

**ANALYSIS AND MODELING OF INELASTICITY IN TENDON:
VISCOELASTICITY, DAMAGE, AND PLASTIC DEFORMATION**

by

Babak Naghizadeh Safa

A dissertation submitted to the Faculty of the University of Delaware in partial fulfillment of the requirements for the degree of Doctor of Philosophy in Mechanical Engineering

Fall 2019

© 2019 Babak Naghizadeh Safa
All Rights Reserved

**ANALYSIS AND MODELING OF INELASTICITY IN TENDON:
VISCOELASTICITY, DAMAGE, AND PLASTIC DEFORMATION**

by

Babak Naghizadeh Safa

Approved: _____
Ajay K. Prasad, Ph.D.
Chair of the Department of Mechanical Engineering

Approved: _____
Levi T. Thompson, Ph.D.
Dean of the College of Engineering

Approved: _____
Douglas J. Doren, Ph.D.
Interim Vice Provost for Graduate and Professional Education
and Dean of the Graduate College

I certify that I have read this dissertation and that in my opinion it meets the academic and professional standard required by the University as a dissertation for the degree of Doctor of Philosophy.

Signed: _____

Dawn M. Elliott, Ph.D.
Professor in charge of dissertation

I certify that I have read this dissertation and that in my opinion it meets the academic and professional standard required by the University as a dissertation for the degree of Doctor of Philosophy.

Signed: _____

Michael H. Santare, Ph.D.
Member of dissertation committee

I certify that I have read this dissertation and that in my opinion it meets the academic and professional standard required by the University as a dissertation for the degree of Doctor of Philosophy.

Signed: _____

Gerard A. Ateshian, Ph.D.
Member of dissertation committee

I certify that I have read this dissertation and that in my opinion it meets the academic and professional standard required by the University as a dissertation for the degree of Doctor of Philosophy.

Signed: _____

David L. Burris, Ph.D.
Member of dissertation committee

I certify that I have read this dissertation and that in my opinion it meets the academic and professional standard required by the University as a dissertation for the degree of Doctor of Philosophy.

Signed: _____

Xin L. Lu, Ph.D.

Member of dissertation committee

ABSTRACT

Analysis and Modeling of Inelasticity in Tendon: Viscoelasticity, Damage, and Plastic Deformation

Tendons are soft connective tissues that connect the muscular system to the skeleton. Tendons are abundant in human body and their primary function is to enable transmission of mechanical force. These tissues are prone to overuse and disease. To understand the relationships between tendon's function and disease, one needs to clearly understand the mechanical behaviors in a physiological context. Despite decades of studies on tendon, a comprehensive framework for studying tendon mechanics that addresses its inelastic mechanical response in relationship to its structure is missing.

The objective of this dissertation was to analyze and model the inelastic behaviors in tendon, which can be categorized into viscoelasticity, damage, and plastic deformation, and study their underlying mechanisms by using state-of-the-art mechanical testing, constitutive modeling, and micro-structural imaging. I addressed this general objective through four specific aims: (1) developing a comprehensive and unifying structurally-inspired modeling framework, reactive inelasticity (RIE), that describes the major inelastic mechanical behaviors of tendon using kinetics of molecular bonds; (2) evaluating damage and plastic deformation as the potential mechanisms of tendon softening behavior during axial loading by using micro-mechanical experiments on tail tendon and RIE modeling; (3) evaluating the poroelastic parameters of tendon, particularly hydraulic permeability, using lateral osmotic loading and biphasic mixture finite element modeling; (4) visualizing and quantifying the 3D microstructure of tendon using serial block-face SEM, and providing a model for interfibrillar load transfer.

This study is innovative in comprehensively addressing the mechanisms of inelasticity in tendon by separately identifying and modeling inelastic behaviors, providing a unifying theoretical explanation for the underlying mechanisms, elucidating novel structure-mechanics relationships, and calculating the inelastic mechanical properties. The outcomes of this study provide novel understanding of tendon mechanics and its relationships to tendon's multiscale structure. The results and tools developed in this dissertation can be used in further studying structure-mechanics relationships in tendon and other tissues, optimizing treatments for pathologies, and designing engineered tissues and materials.

ACKNOWLEDGEMENTS

This dissertation would not have been possible without the help and support of many people. First and foremost, I want to thank my adviser, Dr. Dawn Elliott. Dawn is perhaps the best adviser that a graduate student can wish for. She is a dedicated mentor, a passionate scholar, and a visionary leader. I will be indebted to Dawn for the rest of my life, and hope to be able to follow along the pathway that she has shown to me as a role model. I also would like to graciously acknowledge my co-adviser, Dr. Michael Santare. Mike is a true classic mechanician; his immense knowledge of mechanics and his dedication has been extremely inspiring and guiding for me. I also acknowledge my dissertation committee members, Dr. Gerard Ateshian, Dr. David Burris, and Dr. Lucas Lu, for their visionary inputs in the process of completion of this dissertation. Further, I acknowledge all of my collaborators for their contributions to the projects presented in this dissertation. I am also grateful to the anonymous reviewers, whom generously provided invaluable insights during peer-review of my works, and I acknowledge the funding source for this study (NIH NIBIB grant R01-EB002425).

I would also like to acknowledge my friends and colleagues: Spencer, Megan, John D., Andrea, Kyle, Brandon, Jessica, Ellen, Harrah, and many others from the University of Delaware's excellent scholar community. I also thank my Iranian friends in the United States, with whom I have shared a unique experience. In particular, I was privileged to be acquainted during the challenging years of my PhD with Reyhane, Sadra, and Yashar. Particularly, when continuing research seemed impossible, their support, love, and friendship enabled me by adding confidence to every step I took towards the completion of this dissertation. I also acknowledge my family in Iran and

the US, in particular, Azam, Illiad, Ashraf, Reza, Elizabeth, Ashley, Shahin, Khadijeh, Habib, and Nima. I thank my beloved sister Selda and my brother-in-law Aydin for their awesomeness, love, and encouragement for pursuing my dreams and goals in life, despite all the obstacles along the way. At last, but to the exact opposite of the least, I wholeheartedly thank my incredible parents Akram and Hossein, whom are the reason for the person I am. My journey would be merely impossible and meaningless without their countless sacrifices and support. I also sanctify the memory of my dear grandfather Hossein Sheibani (Babam). Babam was very excited for me, when I told him that I am going to do a PhD, but unfortunately he passed away before I finish my degree, and I could not be with my family during those moments of grief. I want to let Babam know that “Babam! Elabir dohtur oldum!”¹. I never can forget the years that I could not be with my family and loved ones due to the *travel bans* and *walls*. I hope for the day that love is the only true ruler of this world...

This dissertation is dedicated to my parents

Babak Naghizadeh Safa

Summer of 2019

Newark, Delaware USA

¹ Translation from Azeri: Babam! I made it to become a Doctor!

TABLE OF CONTENTS

ABSTRACT	v
LIST OF TABLES	xv
LIST OF FIGURES	xvi
 Chapter	
1 INTRODUCTION	1
1.1 Tendon Etymology and Historical Significance	1
1.2 Clinical Significance	1
1.3 Engineering Significance	3
1.4 Overview of the Dissertation	4
 2 BACKGROUND ON TENDON STRUCTURE-MECHANICS ANALYSIS AND INELASTICITY MODELING	 6
2.1 Overview	6
2.2 Biochemistry and Hierarchical Structure	6
2.3 Mechanical Behavior	7
2.3.1 Stress stiffening or toe-region response	9
2.3.2 Softening at higher deformation	10
2.3.3 Stress relaxation during sustained deformation	10
2.3.4 Creep and rupture under sustained force	10
2.4 Structurally-inspired Modeling for Tissue	11
2.5 Modeling Frameworks for Inelastic Mechanics Analysis	12
2.5.1 General Continuum Mechanics	13
2.5.2 Continuum Damage Mechanics	14
2.5.3 Mixture Theory and Biphasic Modeling	16

3	RESEARCH QUESTIONS AND OBJECTIVES	19
3.1	Aim 1: Reactive Inelasticity	19
3.2	Aim 2: Is Tendon Softening Due to Damage or Plastic Deformation?	20
3.3	Aim 3: Assessing Tendon’s Poroelastic Parameters and the Potential Role of Fluid Viscoelasticity	20
3.4	Aim 4: 3D Micro-structure of Tendon and Mechanical Model for Interfibrillar Load-transfer	21
3.5	Summary of the aims and impact	21
4	A REACTIVE INELASTICITY THEORETICAL FRAMEWORK FOR MODELING VISCOELASTICITY, DAMAGE, AND PLASTIC DEFORMATION IN FIBROUS SOFT TISSUE	22
4.1	Introduction	22
4.2	Reactive Inelasticity	25
4.2.1	Kinematics and relative deformation	26
4.2.2	Free energy and intrinsic hyperelasticity	26
4.2.3	Reactive bond kinetics	31
4.2.4	Bond types	33
4.2.4.1	Formative bonds	33
4.2.4.2	Permanent bonds	33
4.2.4.3	Sliding bonds	34
4.2.5	Damage of bonds	37
4.2.6	Implications of the second law of thermodynamics	39
4.2.7	Summary of formulation	40
4.3	Illustrative Examples	40
4.3.1	Model parameters used in the illustrative examples	43
4.3.2	Sensitivity of the formative bonds to the kinetics rate (Example I)	44
4.3.3	Cyclic loading and damage (Example II)	44
4.3.4	Incremental stress relaxation with softening and anisotropy (Example III)	45
4.4	Discussion	47

5	EVALUATING PLASTIC DEFORMATION AND DAMAGE AS POTENTIAL MECHANISMS OF INELASTICITY IN TENDON	53
5.1	Introduction	53
5.2	Methods	55
5.2.1	Reactive inelastic modeling	56
5.2.2	Plastic deformation and damage constitutive relations	59
5.2.2.1	Kinetics	59
5.2.2.2	Intrinsic hyperelasticity	60
5.2.2.3	Sliding	60
5.2.2.4	Damage	61
5.2.3	Experimental micro-tensile test data	62
5.2.4	Model implementation and parameter identification	62
5.2.5	Data analysis	63
5.2.6	Quantification of inelastic effects	64
5.2.7	Model validation	64
5.3	Results	65
5.4	Discussion	70
5.4.1	Comparison between the plastic deformation and damage models	70
5.4.2	Interpretation of inelastic effects	70
5.4.3	Remarks about RIE modeling	71
5.4.4	Sources of error	71
5.4.5	Conclusion and future direction	72
6	EVALUATION OF TENDON HYDRAULIC PERMEABILITY USING OSMOTIC LOADING AND BIPHASIC FINITE ELEMENT MODELING	74
6.1	Introduction	74
6.2	Material and Methods	76
6.2.1	Sample preparation and grouping	76
6.2.2	Loading protocol	76
6.2.3	Water content measurements	77
6.2.4	transverse strain and image analysis	78

6.2.5	Statistical analysis of water content and comparison to volumetric strain	78
6.2.6	Biphasic finite element model	79
6.2.7	Model parameter identification	81
6.2.8	Statistical analysis of fitted mechanical parameters	81
6.2.9	Prediction of hydraulic permeability during axial loading	82
6.2.10	Distribution of fluid flow and deformation	82
6.3	Results	83
6.3.1	Effect of osmotic loading on water content and tissue strain	83
6.3.2	Optimization results and fit parameters	83
6.3.3	Tendon permeability during tensile tests	87
6.3.4	Distribution of fluid flow and deformation	87
6.4	Discussion	89
7	HELICAL FIBRILLAR MICROSTRUCTURE OF TENDON USING SERIAL BLOCK-FACE SEM AND A MECHANICAL MODEL FOR INTERFIBRILLAR LOAD TRANSFER	94
7.1	Introduction	94
7.2	Methods	96
7.2.1	Serial block-face SEM imaging	96
7.2.2	Segmentation and data analysis	97
7.2.3	Statistics	99
7.2.4	Finite element analysis of helical fibril structures	99
7.3	Results	102
7.3.1	Microstructure of fibrils and SBF-SEM	102
7.3.2	Finite element simulations of the helical fibrils	104
7.4	Discussion	105
7.4.1	Microstructure of fibrils and SBF-SEM	107
7.4.2	Finite element simulations of the helical fibrils	110
8	CONCLUSIONS AND POTENTIAL FUTURE DIRECTIONS	114
8.1	Conclusions	114

8.2	Future Work	116
8.2.1	Force-controlled mechanical experiments for studying inelasticity	116
8.2.2	Using molecular monitoring with inelasticity modeling for understanding mechanical behaviors of tissue	117
8.2.3	Using inelasticity modeling and analysis in clinical studies	118
8.2.4	Generalized framework for model parameter identification and identifiability of inelastic properties	119
8.2.5	Efficient analysis of 3D micro-structure using SBF-SEM for studying structure-mechanics	121
8.3	Summary	121
BIBLIOGRAPHY		123
Appendices.		143
A STRESS AND RELATIVE DEFORMATION		144
B PROOF OF THE STRUCTURE TENSOR (\tilde{M}^α) EXPRESSION FOR SLIDING BONDS		146
C IMPLICATIONS OF THE SECOND LAW OF THERMODYNAMICS		148
C.1	Second law of thermodynamics	148
C.2	Reactive bond compliance with the conditions of the second law	149
C.2.1	Formative bonds	150
C.2.2	Permanent bonds	151
C.2.3	Sliding bonds	151
C.2.3.1	Exponential fibers	152
C.2.3.2	Neo-Hookean	152
C.2.3.3	Holmes-Mow	153
D NOTE ON THE NUMERICAL IMPLEMENTATION OF RIE		154
D.1	Bond kinetics implementation	154
D.2	Calculating damage, energy, and stress	155
E FIT PARAMETER RESULTS FOR THE PLASTIC AND DAMAGE MODELS		156

F	LATERAL STRAIN OF TENDON IN RESPONSE TO OSMOTIC LOADING	158
G	NORMALIZED FLUID FLUX DURING OSMOTIC LOADING	160
H	THE AUXILIARY SHEATH MESH USED FOR THE HELICAL FIBRIL'S FEM ANALYSIS	162
I	STRESS-STRAIN RESPONSE OF A SINGLE HELICAL FIBRIL	163
J	HISTOGRAM OF THE PERCENT TORTUOSITY OF THE FIBRILS	164
K	PERMISSIONS TO INCLUDE PUBLISHED MANUSCRIPTS .	165
	K.1 Permission for manuscripts of Chapters 4 and 5	165
	K.2 Permission for manuscript of Chapter 7	167

LIST OF TABLES

4.1	Summary of structure of a reactive bond type's constitutive relations.	41
4.2	Parameters used for dynamic response of single bond types (Fig. 4.6)	43
4.3	Parameters used for the incremental stress relaxation response tests (Fig. 4.7).	43
5.1	Summary of the bond types, constitutive relations, and the model parameters used for each of the inelastic models. . .	60
6.1	The overall median poroelastic parameters and the range of the resulted fit parameters	87
7.1	Collagen fibril's mechanical properties	102
E.1	Fit parameter results for the plastic and damage models . .	157

LIST OF FIGURES

1.1	Cultural and historical significance of tendon	2
2.1	Hierarchical structure of tendon	8
2.2	Schematic illustration of the mechanical behaviors of tendon	9
4.1	Reference configuration of generations	27
4.2	Example of bonds with first-order rate equation	32
4.3	Consecutive step deformations and multiple generations . .	35
4.4	Effect of damage on molecular kinetics	39
4.5	Example I: Time response of formative bonds to a Heaviside step deformation in a large range of kinetics rates	45
4.6	Example II: Cyclic loading and damage	46
4.7	Example III: Incremental stress relaxation with softening .	48
5.1	Schematic difference between the plastic deformation and damage models	58
5.2	Micro-tensile mechanical testing profile	63
5.3	Fit results for individual experiments.	66
5.4	The IQR of % <i>err</i> of the model fits	66
5.5	Parallel coordinates plots of the fit parameters	68
5.6	Accumulation of damage and plastic deformation	69
5.7	Validation plots for prediction of plastic and damage models	69

6.1	Methods for osmotic loading experiments and finite element modeling	77
6.2	Representative axial force during three phases of the protocol for each of the SPEG solutions	79
6.3	Change to water content and volumetric strain due to osmotic loading	84
6.4	Experimental transverse strain, and model fits	85
6.5	Parallel coordinate plot of the fit parameters	86
6.6	Correlation matrix for tension and compression osmotic loading	88
6.7	Correlation between modulus (E) and (ν)	89
6.8	Predicted deformation-dependent tendon hydraulic permeability	89
6.9	Spatial distribution of fluid flow and displacement on the boundary	90
7.1	Microstructural sliding during micromechanical tensile testing of tail tendon	96
7.2	Experimental methods for SBF-SEM imaging and analysis	98
7.3	Three dimensional segmentation and structural complexity of fibrillar network	103
7.4	Three interesting but isolated structural features	105
7.5	Helical fibrils in tendon's fibrillar structure	106
7.6	Sensitivity analysis of stress transfer due to friction between helically grouped fibrils	107
7.7	Finite element simulation of two helically wrapped fibrils .	108
F.1	Raw data for the lateral strain analysis during osmotic loading	159

G.1	The spatial and temporal distribution of the normalized fluid flux	161
H.1	The auxiliary sheath mesh used for helical fibrils FEM analysis	162
I.1	Stress-strain (σ - ϵ) response of a single helical fibril	163
J.1	Histogram of the percent tortuosity of the fibrils	164

Chapter 1

INTRODUCTION

1.1 Tendon Etymology and Historical Significance

Tendon as a word can be traced back to medieval Latin *tendōn*, which is a variation of the Greek word *ténōn* meaning sinew, a single cord or thread, power, or mainstay [141]. The spelling with -d- occurs by association with Latin *tendere* that stands for *stretch* [49]. As the verbal meaning indicates, the main function of tendon is to be stretched and stream power, which occurs in a physiological setting through transferring muscular contraction to the limbs.

Tendon has been an important material throughout human history. The pre-industrial cultures have used tendon (sinew) as a strong and reliable material for making bows for hunting, and tailoring durable clothing; even some cultures, such as the Inuit people of Greenland, relied heavily on sinew as fixtures and ropes for making hand-tools, tents, and sleds, which is because of the lack of availability of other sources of fiber material such as vegetation [18, 154]. Tendon is an ancient-time super-material, which is reflected in mythology and religious texts, as an example, the biblical hero, Samson's hands were tied with sinew because of the lack of a stronger material known at the time [103]. Due to the strength and importance of tendons, *tenotomy* or excision of tendon, was used as a form of punishment or degradation [103]. A famous example is the Greek hero Achilles mentioned in Homer's *Illiad*, which was only vulnerable at his calcaneal tendon or commonly referred to as the Achilles tendon.

1.2 Clinical Significance

Every human movement engages at least one tendon. Disease and injury to tendon can significantly limit movement and cause pain. Tendons are prone to infectious

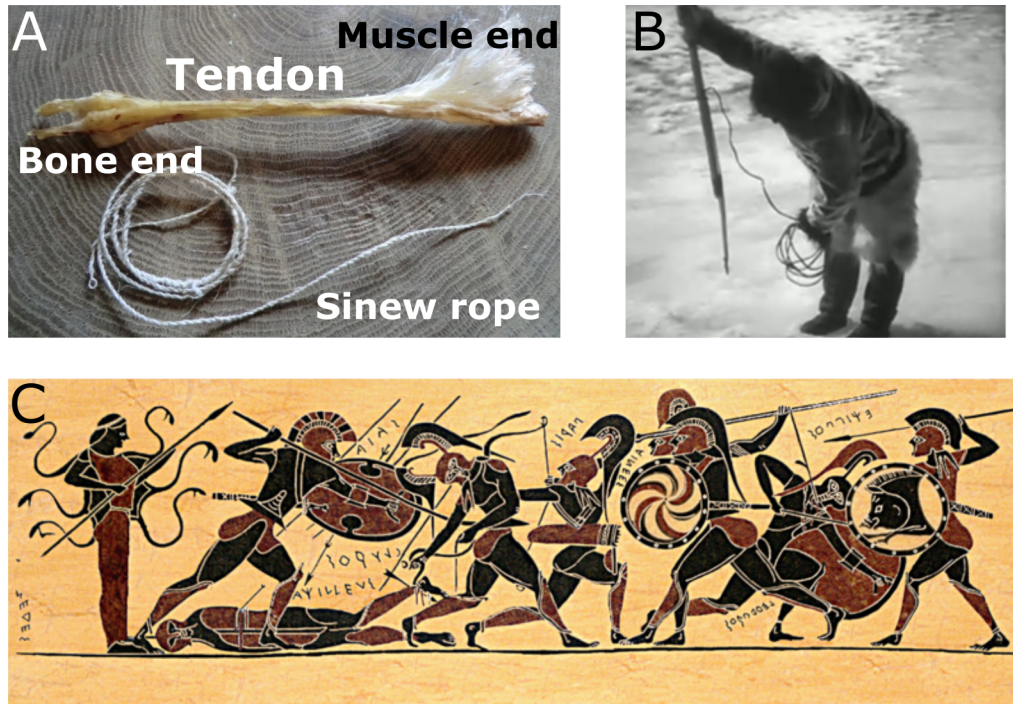


Figure 1.1. Cultural and historical significance of tendon: (A) deer tendon (top) and sinew rope made of it (bottom) [186] (B) an Inuit hunter using a sinew-made harpoon line [63]. (C) An ancient Greek vase painting (540 BCE) depicting the a scene of death of Achilles at the Trojan war, notice the arrow slimming through Achilles' heel [225].

disease, and more commonly, they are subject to mechanical loading-induced injuries. Due to the nature of human activities, tendons undergo complex mechanical loading. These activities are often necessary to maintain a healthy tissue; however, they can lead to acute and chronic disease that result in pain and dysfunction. Hence, the tendons are medically significant. To provide further context about the clinical significance, I review some of the infectious disease and injury-related pathological conditions in tendon.

Tendons are prone to a range of infections caused by micro-organisms, however, they are not common. Bacterial infections occur in tendon, such as purulent tendinitis or tenosynovitis of the surrounding sheath of tendon [148]. This infection may be caused by an animal bite, and the symptoms of infection may present with fever, fatigue, and local tenderness [103]. In rare cases, tendons may also develop soft tissue

sarcoma (clear-cell sarcoma or CCS) that is an aggressive cancerous tumor with “5-year and 10-year survival rates of localized CCS around 60-70% and 40-50%” [39]. In general, the disease in tendon that are not induced by a direct mechanical injury are not common, however, their development might be the sign of a serious medical condition and would need immediate treatment.

The most common tendon disease are the ones related to injury and mechanical loading. Acute rupture of tendon is common, and often occurs in the ankle, shoulders, and the knee. The rupture can be due to an incident of high loading during the course of a simple exercise or an automobile accident. Although these cases may be surgically repaired, rate of success and recovery varies [25,62,229]. Even an incident of overloading which does not result in rupture can result in complications. The acute overloading of tendon can result in inflammation or *tendinitis* that is presented with pain [19]. The other common tendon-disease is chronic *tendinosis* that is the result of repeated injuries to tendon that causes microstructural damage to the tissue. These may be due to a repeated heavy use of tendons in sports or other physically-demanding activities. Common examples are tennis elbow (lateral epicondylitis), and jumper’s knee (patellar tendinosis). Despite this pathological classification, the symptoms and causations of tendinosis and tendinitis can be overlapping and may be confounding each other, and even tendinosis can lead to tendinitis, or vice versa. Hence, the preferred overarching terminology for the mechanical loading induced injury is *tendinopathy*. A tendinopathic tendon may show swelling, microstructural damage, and change of color (to yellow) due to increased vascularisation [59, 119, 203]. All of the aforementioned conditions can be disabling, because the pain and dysfunction can make normal daily tasks unattainable. In order to understand these disease, it is essential to understand the mechanisms of the biomechanical response of tendon.

1.3 Engineering Significance

Tendon’s common diseases and injury are related to mechanical loading. Understanding the mechanism of material’s response to loading and their damage is an

engineering task. This can be explained in a broad sense, with the concept of structural damage. From a general engineering perspective, structural damage is an inelastic (energetically irreversible) behavior that “degrades” the material properties, such as stiffness, and hence causes a deterioration, and eventually loss of mechanical function that can lead to immobility and further complications. However, damage is not the only inelastic behavior in tissue; viscoelasticity, and plastic deformation are separate inelastic behaviors that have overlapping effects and physiological mechanisms with damage. Thus, these mechanisms should be studied by considering their interacting effects and their structural basis across and along the different length scales. Studying the mechanisms of inelastic behaviors by using analytical and engineering techniques is essential in understanding the clinical disorders, designing therapeutic strategies, and engineering artificial tissues.

1.4 Overview of the Dissertation

In this dissertation, theoretical modeling, experimental testing, and structural imaging approaches are used for analyzing and modeling of the inelastic behaviors of tendon. In Chapter 2, the background of the current knowledge about tendon’s structure, and the the experimental and theoretical literature on tendon and tissue inelasticity is reviewed. This is followed with a description of the aims of the dissertation and research objectives in Chapter 3. In Chapter 4, I present a structurally-inspired continuum mechanics theoretical framework, reactive inelasticity (RIE), for modeling fibrous tissue inelasticity based on reactive molecular kinetics. In Chapter 5, the RIE is applied to experimental mechanical behavior of tendon to assess the potential of damage and plastic deformation as mechanisms of inelasticity in tendon. Chapter 6 is focused on the fluid-flow-dependent viscoelasticity of tendon, where we use osmotic loading and biphasic finite element modeling to calculate tendon’s poroelastic mechanical parameters, particularly hydraulic permeability, which are important aspects for understanding the role of fluid-flow in the mechanical response of tendon. In Chapter 7, we study the micro-scale structure of tendon and its implications on mechanical

behaviors by quantifying the 3D micro-scale structure of tendon using serial block-face scanning electron microscopy (SBF-SEM), and providing an interfibrillar load-transfer model based on helical fibrils and finite element analysis. I provide conclusions and recommendations for future studies in Chapter 8.

Chapter 2

BACKGROUND ON TENDON STRUCTURE-MECHANICS ANALYSIS AND INELASTICITY MODELING

2.1 Overview

The focus of this chapter is the background of the structure and mechanics of tendon. I provide an overview of the fibrous structure of tendon and its composition. Since tendon structure is an active subject of research, we only focused on providing a general overview of the literature. The chapter continues by dissecting the major mechanical behaviors of tendon and the structure-mechanics relationships. I provide the experimental accounts for each mechanical behavior, and their analysis. As described earlier, the majority of tendon's mechanical behaviors are inelastic in nature, hence, I reviewed the modeling framework for analysis of inelasticity with a focus on continuum mechanics and structurally-inspired models. I end this chapter by posing the open questions and the research objectives of this dissertation.

2.2 Biochemistry and Hierarchical Structure

Tendons are one of the most abundant orthopedic tissues in human body and are responsible for transmission of mechanical force from muscles to the skeleton. Tendon is a hydrated structure with a hierarchical solid matrix structure (Fig. 2.1A). More than 60% of its mass is water, and the rest is a strong fibrous matrix composed of type-I collagen (65-80%), and various other proteins such as type-III collagen, elastin, proteoglycans [109].

Collagen macromolecules (300 nm length 1.6 nm diameter [30]) are made of three helical polypeptides chains (two $\alpha 1$ and one $\alpha 2$ chains) known as tropocollagen

molecule [57, 126] (Fig. 2.1B). These molecules are cross-linked to one another by several mechanisms including enzymatic and non-enzymatic (e.g., advanced glycation end products AGE) cross-linking (Fig. 2.1 B) [70]. The mechanical properties of collagen structure are sensitive to the density of these cross-linkings, and their stability is a function of temperature and external loading [30, 47, 227]. Other protein components of tendon extracellular matrix such as elastin also are shown to have some potential role in the mechanical response of tendon [33, 85], however, this response is dominated by collagen-I fibrous structure.

The assembly of collagen-I molecules makes *collagen fibrils* (Fig. 2.1A,C). Collagen fibril's diameter ranges from 50 to 500 nm [109]. Collagen-I fibrils have a band pattern (D-period ~ 65 nm), which is the signature of the type-I collagen structure. Some electron microscopy analyses have indicated that collagen fibrils are subject to structural damage such as kinks, when they are subject to high stretch (Fig. 2.1 D). These micro-scale fibrils surround the tendon cells, *tenocytes*, thus their interactions within the fibrillar network and with cells has a potential importance in the biomechanical response of tendon (Fig. 2.1 A).

The next length-scale includes *fascicles* that can be visually seen without equipment (Fig. 2.1 A). Each tendon is made of several fascicles that have a sub-millimeter diameter (Fig. 2.1 A) (e.g., about 500 μm for rat tail tendon fascicles). The fascicles are arranged in a complex interwoven network that in response to mechanical loading show structural sliding, and rotational deformations, indicating an overall heterogeneous structure with underlying helical structures [222].

2.3 Mechanical Behavior

Tendon's main mechanical function is during its axial loading by muscles. This induces a complex mechanical behavior, described below, that is closely tied to its fibrous structure. Tendon's prominent mechanical behaviors include (Fig. 2.2): (1) stress stiffening at low deformation known as a toe-region response, (2) softening at higher deformation, (3) stress relaxation during sustained deformation, (4) creep and

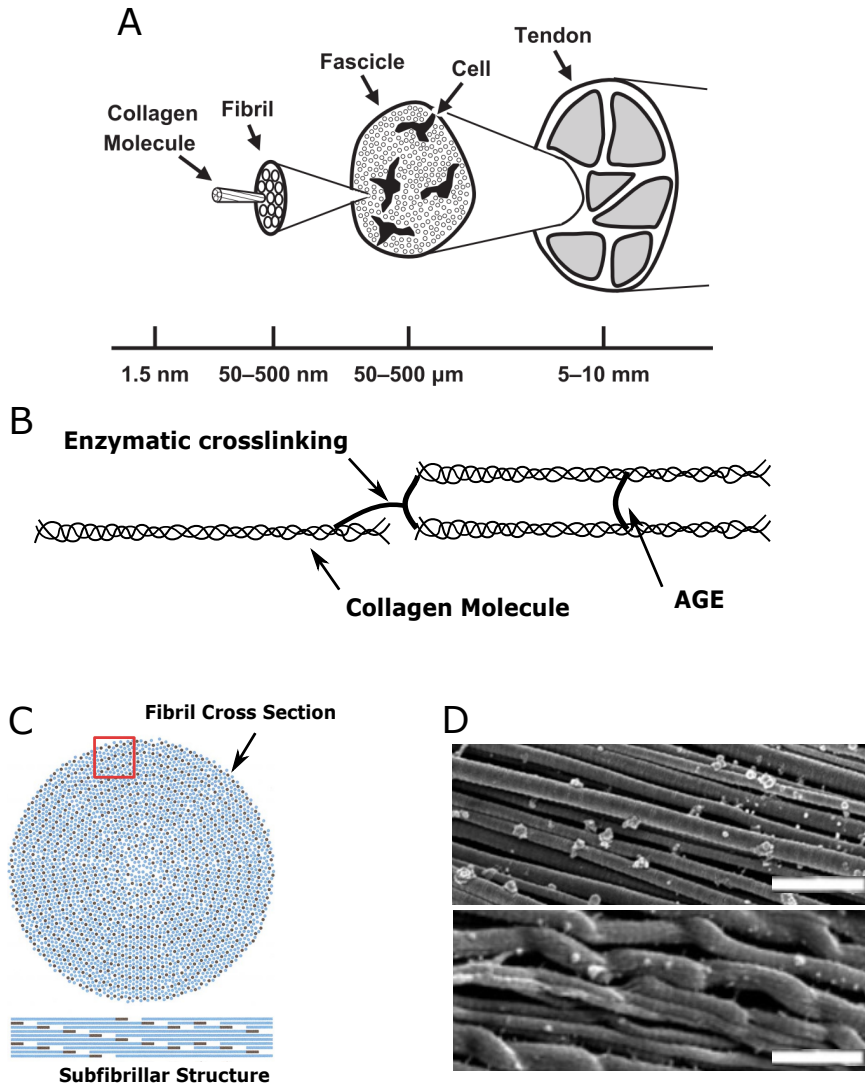


Figure 2.1. (A) Schematic illustration of the hierarchical structure of tendon, adapted from [215] (B) Molecular cross-linking of collagen showing two of the possible types of cross-linking: Enzymatic and advanced glycation end products (AGE) [70]. (C) Longitudinal (top) and transverse (bottom) cuts of fibril structure, showing radial packing and subfibrillar structure due to crosslinking orientation (adapted from [95]) (D) SEM images of non-damaged (top) and damaged (bottom) collagen-I fibrils (adapted from [228]) scale bar is 500 nm.

rupture under sustained force. These nonlinear inelastic mechanical behaviors are the key to understanding the structure-mechanics relationships in tendon. In this dissertation, I will refer to these behaviors at many occasions, thus, in the following, I review some of the key literature on each behavior.

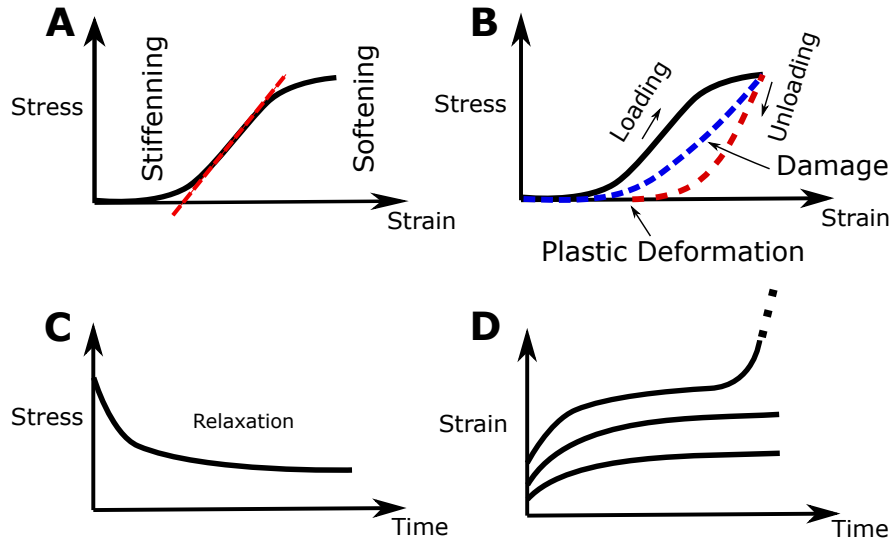


Figure 2.2. Schematic illustration of the mechanical behaviors of tendon(A) Stress stiffening and softening during ramp loading, (B) Unloading with damage (blue dashed) or plastic deformation (red dashed), (C) Stress relaxation during sustained deformation (D) Creep during sustained force

2.3.1 Stress stiffening or toe-region response

This response is a typical behavior of fibrous soft tissue (Fig. 2.2A). It results in a *J-shaped* stress-strain response that is typically observed in axial mechanical tests. Several theories have been proposed to explain this non-linear mechanical behavior. The common interpretation is *fiber-recruitment*, which suggests that the stiffening is due to uncrimping of collagen fibrils, and over the course of mechanical loading the fibrils gradually straighten and eventually fully stretch marking a transition from the toe-region to the linear region of the stress response [80]. Alternative theories suggest that the micro-mechanical realignment and bending of tortuous fibrils cause such behavior [224]. The toe-region is considered the low-load region of mechanical behavior and its transition to linear regime followed with softening is potentially correlated with structural damage, thus this transition and the toe-region response provide important insights into the role of fibrillar structure in tendon’s mechanical response [120].

2.3.2 Softening at higher deformation

Softening at higher deformation occurs upon loading beyond the toe-region and linear-region, and is evident as a progressive decrease in the tangent modulus of tissue (Fig. 2.2A). This behavior can be explained based on an inherent decrease of material stiffness, also known as *damage*, or a shift to the unloaded reference configuration of material, *plastic deformation*(Fig. 2.2B). However, this behavior is dependent on the loading history, and is highly nonlinear, thus, identification of the extent of each of these mechanisms is difficult [1, 164, 210]. This question will be addressed at length in Chapters 4 and 5.

2.3.3 Stress relaxation during sustained deformation

During sustained boundary deformation tendons experience an asymptotic decay of stress to equilibrium Fig. 2.2C) [240]. This phenomena is commonly known as *stress relaxation*, and it is typically observed in soft tissue. Stress relaxation is a viscoelastic behavior. The time-to-equilibrium in tendon is dependent on deformation, and can vary from the order of minutes at small strains, up to to hours at higher deformations [188, 193, 216]. Stress relaxation is seen both under a constant sustained deformation level and under cyclic loading between two levels of deformation which also presents as a hysteresis stress-strain behavior (Fig. 2.2B) [210].

The viscoelastic behaviors cause dissipation of energy, hence they can be categorized as inelastic behaviors. Two structural mechanisms are likely to mediate the dissipation of energy: fluid exudation through the fibrous structure, and intrinsic viscoelasticity of the solid matrix [35, 170, 245]. However, the extent of each of these is not yet known. A framework for modeling solid matrix viscoelasticity will be provided in Chapter 4, and the poroelastic behavior will be addressed in Chapter 6.

2.3.4 Creep and rupture under sustained force

Creep is another inelastic mechanical behavior in tendon that occurs during sustained force loading (or engineering stress) Fig. 2.2D) [117, 219]. Similar to the

viscoelastic stress relaxation, creep behavior may result in an *equilibrium strain* state under both constant and cyclic levels of force, however, unlike relaxation, at high levels of sustained force the equilibrium state may not be achieved, and the tissue can become unstable and deform until rupture (Fig. 2.2D). As an example, it has been shown in Wallaby tail tendon, that 10 MPa of sustained stress can cause creep rupture in a matter of hours, where the yield stress is a much larger number of 144 MPa [233].

The mechanisms of the viscoelastic part of this mechanical behavior, similar to stress relaxation, can be attributed to the exudation of fluid, and intrinsic viscoelasticity of solid matrix [171]. Further, several structural analyses have also shown that creep loading can cause localized deformation in the collagenous structure, known as *discrete plasticity*, which may explain the creep rupture [86]. However, the mechanisms of viscoelastic creep and creep rupture are not yet well understood. While, creep will not be directly addresses here, the modeling framework provides techniques to study creep in future work (Chapter 8)

2.4 Structurally-inspired Modeling for Tissue

The best mechanical models are the ones that relate the structure and physiology to the mechanical behavior of the tissue. Although the phenomenological models are effective in describing the mechanical behaviors in a wide range of observed behaviors, often a physical interpretation is hard or even impossible to achieve. Hence, much efforts have been taken to develop models with physiological and structural bases.

One of the common methods for incorporating the fibrillar structure of tissue for modeling multiscale mechanical behavior is by using a *representative volume element* modeling (RVE). As an example, the *discrete fiber network* model uses volumes of fiber networks generated according to stochastically determined parameters [76], and the overall finite element problem is solved by the means of volume-averaged stress from each RVE [196]. The heterogeneity and the spatial distribution of the parameters can be incorporated into these models, based on image-analysis of fiber alignment [246]. The structural parameters of the RVE may also be controlled by mathematical

parametrization [26, 175]. However, incorporating structural details comes with the cost of the complexity of the system and more expensive computation.

An alternative method is *structurally-inspired* modeling that uses both the benefits of phenomenological models and has a sound structural explanation. Structurally-inspired models have been used by many investigators to address both elastic and inelastic mechanics of tissue. As an example, the *shear-lag* model is used to explain microstructural sliding, stiffening, and softening behaviors of tendon [2, 216]. Another example of structurally-inspired modeling is the use of kinetics of reactive molecular bonds to model mechanical behavior of tissue. The applications of this modeling framework include reactive viscoelasticity [10], reactive damage [151], and growth/remodeling [8]. These models use the structural features of tissue and *observable state variables*, and also allow for a continuum mechanics framework formulation. In this dissertation, I continued the work on reactive mechanics and generalized it to a comprehensive framework for modeling tissue inelasticity, *reactive inelasticity*, with theoretical detail included Chapter 4, and applied it to the experiments on tendon in Chapter 5.

2.5 Modeling Frameworks for Inelastic Mechanics Analysis

Tendon's mechanical behaviors, as described earlier, are majorly inelastic; hence, I review the common inelasticity modeling frameworks for analysis of tendon mechanics and their essential formulation.¹ We first need to establish the groundwork of general continuum mechanics, which will also provide clarity about our notation. We first review the formulation of the classic continuum damage mechanics (CDM). The section continues with a brief overview of the mixture theory by focusing on the biphasic mixture modeling, and the chapter finishes with examples of structural and structurally-inspired models for studying tissue inelasticity.

¹ At this point, a reader with good knowledge of continuum mechanics may choose to skip to Chapter 3 without missing the continuity of the dissertation.

2.5.1 General Continuum Mechanics

If $\chi(\mathbf{X})$ describes the positions of the material points in spatial coordinate as a function of its reference position (\mathbf{X}), the deformation gradient is defined as

$$\mathbf{F} = \frac{\partial \chi}{\partial \mathbf{X}} \quad (2.1)$$

For a general deformation, \mathbf{F} is a second order tensor without any requirement for symmetry; however, for an admissible deformation the determinant will be positive-definite $\det \mathbf{F} > 0$. Subsequently, the right Cauchy strain strain tensor is derived as

$$\mathbf{C} = \mathbf{F}^T \mathbf{F} \quad (2.2)$$

Where, unlike \mathbf{F} , \mathbf{C} is a symmetric tensor. It should be noted that, in this dissertation we will use the *tensor notation* unless otherwise mentioned; and a ‘bold-face symbol’ indicates a tensor variable. It goes without saying that this definition also includes the vectors, as rank-one tensor variables.

Now, consider the Helmholtz free energy density (Ψ) for a material during an isothermal process. A useful consideration is when the material is *hyperelastic*, which indicates that there is a one-to-one relationship between state of deformation and energy. This idealized concept has the practical importance of being useful for simplifying the description of nonlinear elastic behavior and providing a basis for more complex continuum models. Due to the principal of objectivity, the free energy should not be a function of coordinate system, thus the free energy for a hyperelastic material can be written as a function of the strain tensor invariants [205]

$$\Psi(\mathbf{C}) = \Psi(I_1, I_2, I_3). \quad (2.3)$$

Where are $I_{1,2,3}$ are the invariants of \mathbf{C} :

$$I_1 = tr(\mathbf{C}), I_2 = \frac{1}{2} [tr(\mathbf{C}^2) - tr(\mathbf{C})^2], \text{ and } I_3 = \det(\mathbf{C}). \quad (2.4)$$

It is common to include other *pseudo invariants* to this set of invariants to account for *anisotropic material* behavior, which can be related to the stretch of fibrillar component and invariants of higher order structure tensors. [205]

The second Piola-Kirchhoff stress for a hyperelastic material, under isothermal deformation can be written as [211]

$$\mathbf{S} = 2 \frac{\partial \Psi}{\partial \mathbf{C}} = \left(\sum_i 2 \frac{\partial \psi}{\partial I_i} \frac{\partial I_i}{\partial \mathbf{C}} \right) \quad (2.5)$$

Also, it can be shown that the Cauchy stress tensor is [89]

$$\mathbf{T} = J^{-1} \mathbf{F} \mathbf{S} \mathbf{F}^T \quad (2.6)$$

2.5.2 Continuum Damage Mechanics

In classical continuum damage mechanics (CDM), typically a damage term ($0 < D < 1$) is introduced as an internal variable to modify material behavior. The idea of damage term was first introduced and used for solving the creep damage problem of metals [105]. Continuum damage mechanics later evolved for different applications in engineering including fracture mechanics, and fatigue of composite material [113, 231, 232]. Recently there have been some studies applying the idea of CDM to tissue mechanics including mechanics of cardiovascular [16], tendon [149, 230, 233], ligament [191, 220], intervertebral disk [92], and articular cartilage [118] tissues. CDM models usually consist of a hyperelastic reference material state which is altered to the damaged state by damage term (D). More elaborate models also have been developed such as viscoelastic [161, 202], and plastic and viscoplastic damage models [202].

Using an appropriate scalar function for D , it is possible to account for non-linear softening. Further, it should be noted that for a hyperelastic material there is a unique one-to-one relationship between a given deformation and the state of energy and consequently stress, however, when damage is accumulated, this relation should

be modified. It is assumed that during a damage-inducing loading the material progressively loses its ability to absorb strain energy in a non-recoverable way. As a result, the one-by-one relation does not hold anymore. However, this process will still obey the laws of thermodynamics, and thus the dissipation of energy should maintain the conditions of the second law for a non-reversible process. Using the damage term as an *internal variable* [34], one can modify the Helmholtz free energy as the following:

$$\Psi(\mathbf{C}, D) = (1 - D)\Psi_0(\mathbf{C}) \quad (2.7)$$

As a result, using the Clasius-Duhem equation as one form of the second law of thermodynamics [34, 89] the dissipation of energy due to damage is

$$\mathcal{D} = \frac{1}{2}\mathbf{S} : \dot{\mathbf{C}} - \dot{\Psi} \geq 0 \quad (2.8)$$

Where \mathcal{D} is the energy dissipation per unit volume. For any physically admissible process the following relations will hold [[34]

$$\frac{1}{2}\mathbf{S} : \dot{\mathbf{C}} - (1 - D)\frac{\partial\Psi_0}{\partial\mathbf{C}} : \dot{\mathbf{C}} + \Psi_0\dot{D} \geq 0 \quad (2.9)$$

This inequality should stand for any physically admissible process. As a result:

$$\mathbf{S} = 2(1 - D)\frac{\partial\Psi_0}{\partial\mathbf{C}} = (1 - D)\mathbf{S}_0, \quad \text{and} \quad \dot{D} \geq 0 \quad (2.10)$$

Two main points can be taken from these relationships. First, the stress can be derived from a scalar energy equation, which is similar to the hyperelastic case, however, it is multiplied by the damage term $(1 - D)$ that is always less than one. Second, since the energy density has a positive value, the rate of damage (\dot{D}) has to be greater than or equal to zero to meet the conditions of the second law of thermodynamics, meaning damage increases if the system does not heal. This method provides a framework for using the common formulation for hyperelastic constitutive relations in combination

with damage that can account for irreversible softening of the system. It should also be added, that the scalar D applies to isotropic damage case, however, for a generalized anisotropic case a tensor definition might be necessary, which, more or less, would follow a similar theoretical setting [104].

2.5.3 Mixture Theory and Biphasic Modeling

As described earlier, tendons and other soft tissue, are complex hydrated biopolymeric structures. To address the mechanics of these complex systems, *mixture theory* is a powerful framework that has been successfully applied to modeling poroelasticity [143], with inert and charged solutes [97,115], multi-generation material [12], growth and remodeling [8,11], reactive solids [10,150], and complex combinations of soft tissue. The underlying assumption in mixture theory is to treat the material as a continuum with multiple phases of material co-occupying the space. That is, for an infinitesimal volume $dvol$

$$dm = \sum_i dm^i = \sum_i \rho^i dvol, \quad (2.11)$$

where, dm is the total mass, dm^i is the mass of each phase (with superscript i), and ρ^i is the apparent density of phase ‘ i ’, which is defined as:

$$\rho^i = \frac{dvol^i}{dvol} \rho_0^i \quad (2.12)$$

where ρ_0^i is the intrinsic density of the phase, and $\frac{dvol^i}{dvol}$ is the *volume fraction* of the phase ϕ^i :

$$\phi^i = \frac{dvol^i}{dvol} \quad (2.13)$$

Hence, by assuming that there is no void space in the continua, one can easily show that

$$\sum_i \phi_i = 1. \quad (2.14)$$

A mixture can be generalized into having multiple phases, and based on the number and types of phases one can formulate biphasic [143], triphasic [115], and in general

multiphasic mixtures, which have a significantly more challenging mathematical setup for increasing number of phases. For tendon, due to dominance of collagen-I and small GAG content, it is reasonable to assume that there are only two phases, thus tendon can be considered to be a *biphasic mixture*, with a solid phase ($i = s$) and fluid phase ($i = f$). In tendon, fresh-frozen ϕ^s is approximately 50% [183]. Moving forward we will only focus on a simplified form of biphasic formulation.

To continue the continuum formulation we should account for continuity, and conservation of linear momentum. The continuity equation can be written as

$$\nabla \cdot (\phi^s \mathbf{v}^s + \phi^f \mathbf{v}^f) = 0, \quad (2.15)$$

Where, \mathbf{v}^s and \mathbf{v}^f are the velocity of solid and fluid phase respectively, and can be derived from the deformation of each phase, $\mathbf{u}^i = \mathbf{x}^i - \mathbf{X}$, as:

$$\mathbf{v}^i = \frac{\partial \mathbf{u}^i}{\partial t} + \mathbf{u}^i \cdot \nabla (\mathbf{u}^i) \quad (2.16)$$

By using Eq. (2.14) the above relation can be simplified to

$$\nabla (\mathbf{v}^s + \mathbf{w}) = 0 \quad (2.17)$$

Where $\mathbf{w} = \phi^f (\mathbf{v}^f - \mathbf{v}^s)$ is a measure for the *flux* of the fluid relative to the solid phase. As a simple model, *Darcy's law* can be used to relate \mathbf{w} to the gradient of the pressure (∇p) in the medium

$$\mathbf{w} = -\mathbf{k} \cdot \nabla p \quad (2.18)$$

This relation indicates that fluid would move in the opposite direction to increasing pressure. The velocity of the fluid depends on the tensorial variable \mathbf{k} which is often called the *hydraulic permeability*. For an isotropic case, hydraulic permeability is a scalar and for tissue it is common to use either units of $\text{mm}^4(\text{N s})^{-1}$ or $\text{m}^4(\text{N s})^{-1}$. For the anisotropic case, a second order tensorial format would be appropriate [14].

The conservation of linear momentum for a continuum in equilibrium reads as

$$\nabla \cdot \mathbf{T} + \rho \mathbf{b} = 0 \quad (2.19)$$

Where, \mathbf{T} is the Cauchy stress and \mathbf{b} is the body force. In tissue mechanics application, body forces such as gravity and other forms often are small compared to the actual tractions on the system, and they maybe neglected; therefore

$$\nabla \cdot \mathbf{T} = \mathbf{0} \quad (2.20)$$

In the biphasic mixture theory, the Cauchy stress can be explicitly written as

$$\mathbf{T} = -p\mathbf{I} + \mathbf{T}^s \quad (2.21)$$

where, \mathbf{T}^s is the stress-share of the solid phase. Therefore, the linear momentum equation can be rewritten as

$$-\nabla p + \nabla \cdot \mathbf{T}^s = \mathbf{0} \quad (2.22)$$

In summary, the set of differential equations (Eqs. (2.17) and (2.22)), with appropriate constitutive relations for solid matrix stress (\mathbf{T}^s) (that can be derived from a scalar energy relation and Eq. (2.6)), and hydraulic permeability (such as Darcy's law Eq. (2.18)) result in four equations with the four unknowns of pressure (p), solid stress (\mathbf{T}^s), the relative flux of fluid phase (\mathbf{w}), and solid matrix deformation (\mathbf{v}^s). This set of partial differential equations can be solved with a given set of boundary conditions, such a prescribed pressure, deformation, or traction. The mixture theory, and particularly the biphasic model, have been extensively studied in the literature for the cases of stress and creep, and hence in the interest of the length of this dissertation we skip the details of considerations for thermodynamic equilibrium, details of the boundary conditions, and finite element implementation (for further details see [115, 132])

Chapter 3

RESEARCH QUESTIONS AND OBJECTIVES

Despite decades of studies on tendon mechanics, several essential questions are unanswered about the mechanisms of inelastic mechanical behavior of this tissue. These include, but are not limited to, the share of damage and plastic deformation in softening and failure of tissue, the relative roles of fluid flow and intrinsic viscoelasticity in the mechanical response of tendon, and the relationship between the fibrous structure of tendon and its inelastic behaviors.

Particularly, a comprehensive framework for analysis and modeling of the inelastic mechanisms in tendon is not available. Hence, the objective of this dissertation was to analyze and model the inelastic behaviors in tendon, which can be categorized into viscoelasticity, damage, and plastic deformation, and study their underlying mechanisms by using state-of-the-art mechanical testing, constitutive modeling, and micro-structural imaging. I pursued this overall objective through four aims. Each aim was part of collaborative research, hence, in each aim, where the author is referred to, the plural first-person ‘*we*’ is used instead of the single pronoun ‘*I*’.

3.1 Aim 1: Reactive Inelasticity

To distinguish the mechanical behaviors of tissue, we developed a theoretical framework that comprehensively addresses tissue inelasticity. Inspired by the molecular structure of soft tissue, we developed a comprehensive continuum mechanics modeling framework, reactive inelasticity (RIE), that is based on the energy of reactive molecular bonds. This framework is capable of distinctively addressing hyperelasticity, viscoelasticity, damage, and plastic deformation within the same constitutive setting by using the concept of bond breaking and reformation (reactivity) in response

to external mechanical stimulation. We show that by combination of different bond types, a wide range of elastic and inelastic mechanical behaviors can be modeled. This aim is discussed in Chapter 4.

3.2 Aim 2: Is Tendon Softening Due to Damage or Plastic Deformation?

We used experimental mechanical data to explain whether damage or plastic deformation are responsible for the softening behavior seen in tendon stress-strain curves prior to failure, which is the focus of Chapter 5. This is important, because damage reduces material stiffness, where in plastic deformation the reference configuration is shifted, without necessarily a change to the material properties. Because of the non-linearity in stress-strain response (toe-region), and the viscoelastic behavior of tendon, it is difficult to measure these behaviors solely by mechanical tests. Hence, we developed two models, each for damage or plastic deformation by using the RIE modeling framework and applied these models by multi-start optimization to macro-scale experimental data on tail tendon. We validated the models by predicting an independent experimental dataset on similar tissue.

3.3 Aim 3: Assessing Tendon’s Poroelastic Parameters and the Potential Role of Fluid Viscoelasticity

Tendon’s viscoelastic behavior in general can be attributed to two mechanisms: fluid-flow-dependent viscoelasticity (poroelastic effect), and inherent solid matrix viscoelasticity. However, the relative extent of these are not known. In this aim, we quantified the poroelastic parameters of tendon, especially the hydraulic permeability, by isolating the mechanics of fluid flow and solid matrix viscoelasticity using lateral osmotic swelling experiments and biphasic mixture finite element (FE) modeling. This aim is addressed in Chapter 6. We osmotically loaded tail tendon fascicles in the lateral direction, quantified the induced lateral strain over time, and fitted the temporal lateral strain to the FE model and evaluated the permeability and the other poroelastic

properties of tendon. This study provides the required information for understanding the potential role of fluid flow in the mechanical behavior of tendon.

3.4 Aim 4: 3D Micro-structure of Tendon and Mechanical Model for Interfibrillar Load-transfer

The scope of this aim was to visualize the three-dimensional fibril organization of rat tail tendon and to study the potential of interfibrillar friction within helically wrapped groups of fibrils to serve as a mechanism for load transfer Chapter 7. First, we visualized the microstructure of tendon in three dimensions using SBF-SEM. We found a complex network, with many helically wrapped fibrils. These observations informed the second part of this study, in which we used finite element (FE) analysis to test the hypothesis that frictional contact between helically wrapped fibrils can transfer stress (load) between fibrils without a need for a mediating matrix.

3.5 Summary of the aims and impact

This study is significant in that it advances knowledge in three fronts of tendon and tissue mechanics, that include: theoretical modeling (Chapters 4 and 5), analysis of the experimental mechanical behaviors (Chapters 5 and 6), and structure-mechanics relations at different length-scales (Chapter 7). Particularly, the reactive inelasticity framework, multi-start model parameter identification technique, lateral osmotic loading, and analysis of microstructure with SBF-SEM are novel methods and tools that could be adopted to understand the inelastic mechanical behaviors of other tissue systems as well. In summary, the aims of this dissertation are designed to answer the central questions about the inelastic mechanical behaviors of tendon, yet the findings have important implications for tissue mechanics analysis and modeling that are discussed in this dissertation (Chapter 8).

Chapter 4

A REACTIVE INELASTICITY THEORETICAL FRAMEWORK FOR MODELING VISCOELASTICITY, DAMAGE, AND PLASTIC DEFORMATION IN FIBROUS SOFT TISSUE

These findings are published in *Babak N. Safa, Michael H. Santare, Dawn M. Elliott. ‘A Reactive Inelasticity Theoretical Framework for modeling Viscoelasticity, Plastic Deformation, and Damage in Soft Tissue,’ Journal of Biomechanical Engineering (2018)* (<https://doi.org/10.1115/1.4041575>)

4.1 Introduction

Fibrous soft tissues such as tendon, meniscus, intervertebral disc, etc., are biopolymeric material that have non-linear, anisotropic, and inelastic mechanical behaviors. An inelastic behavior, contrary to an elastic behavior, is one that dissipates energy during mechanical loading. Three major inelastic behaviors that are experimentally observed in fibrous soft tissues are: viscoelastic behavior [36, 93, 241], plastic deformation [1, 27, 134, 178], and damage [149, 230]. Understanding the underlying mechanisms of these behaviors is essential for elucidating the relationships among the mechanical loading, pathological conditions (e.g., tendinopathy, meniscus rupture, and disc herniation), and tissue’s structure.

Fibrous soft tissues have a hierarchical structure that is predominantly composed of extracellular proteins such as different types of collagen and proteoglycans, and have a high water content, where the underlying microstructural organization is responsible for the variations in tissue’s mechanical properties. Inelastic mechanical responses can occur with loading, resulting in altered microstructure and mechanical properties, and even loss of function and rupture. While tissue’s elastic and viscoelastic behaviors have been studied for decades, there is no comprehensive framework

for studying inelastic behaviors of tissue in a structural context; perhaps due to the complex nature of experimental measurement of the inelastic behaviors that occur simultaneously and can have overlapping effects (e.g., plastic deformation and damage). Thus, a theoretical framework is necessary to study these behaviors that uniquely identifies characteristics of different inelastic behaviors and their underlying mechanisms based on tissue structure.

From a theoretical point of view, an inelastic behavior is a path-dependent and irreversible thermodynamic process that may be modeled using the theory of internal state variables (ISV) [34,91]. Various phenomenological ISV expressions have been used to model tissue’s mechanical behavior. For instance, decomposition of strain [174] and stress [90] tensors into elastic and inelastic components is a common practice to model viscoelasticity, where the inelastic components are hidden internal variables that correspond to the non-equilibrium part of the mechanical response. For plastic deformation (permanent set) in tissue [247] used a structural approach to model this inelastic behavior in cyclic loading by proposing a shift in reference configuration of exogenously crosslinked matrix of tissue. In another study, to model softening based on permanent set and damage, two weight factors were used based on alterations to the fibrous structure of tissue due to mechanical loading [159,160]. A similar inelastic variable set was used to model permanent deformation and damage that evolve according to the history of maximum energy of fiber families [60] that is based on the theory of *pseudo-elasticity* [51,235]. Damage, perhaps the most common variable for modeling tissue inelasticity [125], is often used to model stress-softening or Mullin’s effect [48,145]. In tissue, damage is usually modeled according to the number of “broken” fibers [4,149,189]. This formulation is similar to the definition of the damage parameter in classic continuum damage mechanics that is based on occurrence of micro-voids in engineering material such as metals and concrete [105,123]. Despite nearly four decades of successful use of phenomenological approaches to study tissue’s inelastic behaviors, their applicability is limited by the focus of individual models on a subset of inelastic behaviors, and in particular for ISV approaches, there is often not a clear

physical interpretation of parameters.

In this study, we used the combination of theory of ISVs and the kinetics of molecular bonds to develop a structurally-inspired continuum mechanics framework that addresses the inelastic behaviors of tissue's solid matrix. In a few words, we define reactive bonds as those which break and reform in response to mechanical loading; this process results in dissipative changes to the stored energy of the material and inelastic mechanical behaviors. We selected the number fraction of molecular bonds (w^α), their reference deformation gradient ($\mathbf{\Pi}^\alpha$), and damage parameter (D) as state variables to address inelastic behaviors. This framework allows for modeling of all three of the aforementioned inelastic behaviors, viscoelastic behavior, plastic deformation, and damage, using the same set of constitutive relations at different ranges of kinetic rate of bond breakage and reformation.

Kinetics of molecular bonds has been previously introduced by Tobolsky and co-workers to model stress-relaxation of polymers based on the energy of a network of molecules with transient cross-links, that is commonly referred to as the *two-network model* [73, 223]. In a similar way, permanent set has been modeled using the idea of kinetics of breaking and reforming bonds [6, 168], where often the concept of material with multiple natural configurations is employed in a thermomechanical framework [144, 169]. This framework is widely used for studying mechanical behaviors of engineering polymers [46, 136, 139, 192, 239] with various physical interpretations based on the molecular structure of polymers [48]. For tissue mechanics application, a similar idea was recently adapted to model damage of cartilaginous constructs that addresses damage as the fraction of failed bonds, which is an observable variable and can be experimentally measured [151]. Reactive viscoelasticity was introduced by Ateshian to model viscoelasticity of a constrained solid mixture [10, 150]. In that model, two separate bond types were introduced: weak and strong, to model the transient and equilibrium mechanical response, respectively. In the current work, we generalize that concept and show that these bonds are not separate, and strong bonds are a special

case of weak bonds. Additionally, by employing this generalization and taking inspiration from prior work in polymer mechanics, the sliding bond type was introduced that can instantaneously break and reform into a stressed-configuration, which results in plastic deformation. Given the structural basis of this framework and its consistency in addressing several inelastic behaviors, reactive inelasticity is well suited for studying the underlying mechanisms of inelasticity in tissue. Thus, the objective of this study was to comprehensively address tissue inelasticity by developing a structurally-inspired continuum mechanics framework, reactive inelasticity (RIE), based on the energy of reactive molecular bonds.

This chapter is organized as follows: in Section 4.2 we formulate the theory of reactive inelasticity by defining the free energy of a reactive body with generic molecular bond types, where the concepts of intrinsic hyperelasticity and generalized bond kinetics are formulated. Further, we introduce special bond types suited for different mechanical behaviors: formative bonds for a viscoelastic behavior, permanent bonds for hyperelastic behavior, and sliding bonds for plastic deformation. Damage is added to the formulation by allowing for the reduction of the number fraction of load bearing bonds. To demonstrate the key features of this framework, in Section 4.3 we provide several numerical examples of the mechanical behavior of single bond types and their combinations. Finally, in Section 4.4, comparisons to the other existing inelasticity models for tissue, and physical interpretation of bonds are discussed.

4.2 Reactive Inelasticity

In the following, we will describe the mechanics of a reactive material. In brief, a reactive material is made of a combination of different bond types each with different characteristics. Each bond type is associated with a certain mechanical behavior (e.g., formative bonds with viscoelastic behavior). Bonds break and reform (i.e., react) when subjected to an external loading and this process initiates new generations. Generations are molecular bonds of certain bond type that were initiated at the same time and, thus, have a mutual reference configuration. Damage is introduced to all of the bond types

by reducing the fraction of active bonds in the material, and finally the consequences of the second law of thermodynamics are discussed.

4.2.1 Kinematics and relative deformation

Consider a solid body made of a set of material points that are energetically constrained with different types of molecular bonds (indicated by a subscript γ). These bonds deform in a smooth path $\mathbf{x} := \boldsymbol{\chi}(\mathbf{X}, t)$, where \mathbf{x} stands for the current configuration of bonds and \mathbf{X} is their master reference configuration. Hence, the deformation gradient tensor is defined as $\mathbf{F} := \frac{\partial \boldsymbol{\chi}(\mathbf{X}, t)}{\partial \mathbf{X}}$ and the right Cauchy-Green deformation tensor as $\mathbf{C} := \mathbf{F}^T \mathbf{F}$. Each bond type may have different generations (indicated by superscript α), and despite their mutual path of deformation and master reference configuration, every generation has a different reference configuration (\mathbf{X}_γ^α), which is a function of the conditions at the time of formation of the bonds (Fig. 4.1). By using the chain rule of differentiation, the relative deformation gradient tensor for each generation (\mathbf{F}_γ^α) is

$$\mathbf{F}_\gamma^\alpha := \mathbf{F}(\boldsymbol{\Pi}_\gamma^\alpha)^{-1}, \quad (4.1)$$

where $\boldsymbol{\Pi}_\gamma^\alpha := \frac{\partial \mathbf{X}_\gamma^\alpha}{\partial \mathbf{X}}$ is the reference deformation gradient tensor of generation α of bond type γ . This procedure results in *multiplicative decomposition* of deformation [121, 129, 200]. As a result, the relative right Cauchy-Green deformation tensor \mathbf{C}_γ^α is

$$\mathbf{C}_\gamma^\alpha := (\boldsymbol{\Pi}_\gamma^\alpha)^{-T} \mathbf{C} (\boldsymbol{\Pi}_\gamma^\alpha)^{-1}; \quad (4.2)$$

note that $\mathbf{A}^{-T} := (\mathbf{A}^{-1})^T$.

4.2.2 Free energy and intrinsic hyperelasticity

The free energy density of the system is the combination of the energy density of all the bond types

$$\Psi = \sum_{\gamma} \Psi_{\gamma}, \quad (4.3)$$

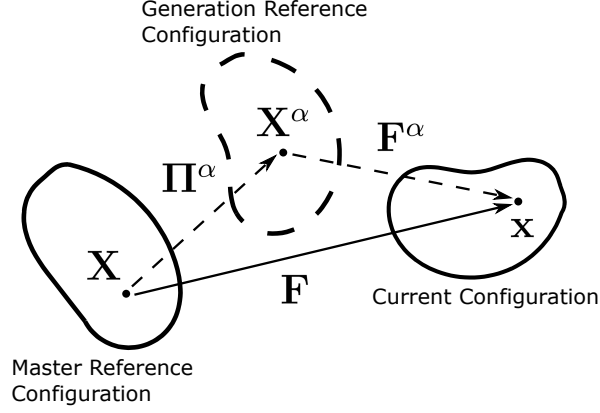


Figure 4.1. Reference configuration of generations. In a body with the master reference configuration \mathbf{X} for generation α the relative deformation gradient tensor (\mathbf{F}^α) is defined using the reference configuration (\mathbf{X}^α).

where Ψ is the Helmholtz free energy density (per volume). The energy density of each bond type is the sum of the energy from each of its generations

$$\Psi_\gamma = \sum_\alpha n_\gamma^\alpha \bar{\psi}_\gamma^\alpha, \quad (4.4)$$

where n_γ^α is the number density, and $\bar{\psi}_\gamma^\alpha$ is the average energy of bonds from generation α of bond type γ . Alternatively, by defining the number fraction of each generation as

$$w_\gamma^\alpha = \frac{n_\gamma^\alpha}{\sum_\alpha n_\gamma^\alpha} = \frac{n_\gamma^\alpha}{n_{\gamma,total}}, \quad (4.5)$$

where $n_{\gamma,total}$ is the number density of a bond type in the natural state of the material, Eq. (4.4) can be re-written as

$$\Psi_\gamma = \sum_\alpha w_\gamma^\alpha \psi_\gamma^\alpha, \quad (4.6)$$

where

$$\psi_\gamma^\alpha = n_{\gamma,total} \bar{\psi}_\gamma^\alpha. \quad (4.7)$$

Here, ψ_γ^α denotes the overall energy density of a generation, which, in general, can be a function of deformation, temperature and other state variables. However, in this

formulation we consider a unique deformation dependence that implies that generations are *intrinsically hyperelastic*. That is,

$$\psi_\gamma^\alpha = \psi_\gamma(\mathbf{C}^\alpha). \quad (4.8)$$

The above equation also denotes that the intrinsic hyperelasticity relation is the same for all of the generations of one bond type, and thus is a characteristic of that type of bonds. Therefore, Eq. (4.6) reads as

$$\Psi_\gamma = \sum_\alpha w_\gamma^\alpha \psi_\gamma(\mathbf{C}_\gamma^\alpha). \quad (4.9)$$

Note that for a bond type with no damage

$$\sum_\alpha w_\gamma^\alpha = 1, \quad (4.10)$$

which indicates that the energy density of each bond type (Eq. (4.9)) is a weighted sum of the energy density of all its generations. Thus, the overall free energy density of the material can be written in the following form

$$\Psi(\mathbf{F}, w_\gamma^\alpha, \mathbf{\Pi}_\gamma^\alpha) = \sum_\gamma \sum_\alpha w_\gamma^\alpha \psi_\gamma(\mathbf{C}_\gamma^\alpha). \quad (4.11)$$

Here, deformation (represented by \mathbf{F}), the number fraction of generations of bond types (w_γ^α) as well as their reference deformation gradient ($\mathbf{\Pi}_\gamma^\alpha$) are the state variables. To simplify the notation without losing generality, we will continue the discussion for one type of bond, where the total response for a mixture of multiple bond types should be taken as a summation over all existing bond types (such as in Eq. (4.11)).

The second Piola-Kirchhoff stress tensor is written as [34]

$$\mathbf{S}(\mathbf{F}, w_\gamma^\alpha, \mathbf{\Pi}_\gamma^\alpha) = 2 \frac{\partial \Psi(\mathbf{F}, w_\gamma^\alpha, \mathbf{\Pi}_\gamma^\alpha)}{\partial \mathbf{C}}. \quad (4.12)$$

Also, by using Eq. (4.9) for a reactive material, Eq. (4.12) can be re-written as (see the Appendix A)

$$\mathbf{S}(\mathbf{F}, w^\alpha, \mathbf{\Pi}^\alpha) = \sum_{\alpha} w^\alpha (\mathbf{\Pi}^\alpha)^{-1} \mathbf{S}^\alpha(\mathbf{C}^\alpha) (\mathbf{\Pi}^\alpha)^{-T}, \quad (4.13)$$

where we also adopted the following definition for stress associated with each generation:

$$\mathbf{S}^\alpha(\mathbf{C}^\alpha) := 2 \frac{\partial \psi(\mathbf{C}^\alpha)}{\partial \mathbf{C}^\alpha}. \quad (4.14)$$

For coordinate-invariance, the state of stress equivalently is determined using the invariants of \mathbf{C}^α :

$$I_1^\alpha = \text{tr}(\mathbf{C}^\alpha), \quad I_2^\alpha = \frac{1}{2} [\text{tr}(\mathbf{C}^\alpha)^2 - \text{tr}((\mathbf{C}^\alpha)^2)], \quad \text{and} \quad I_3^\alpha = \det(\mathbf{C}^\alpha), \quad (4.15)$$

where $\text{tr}(\cdot)$ and $\det(\cdot)$ stand for trace and determinant of a second order tensor, respectively. Often, the given set of invariants suffices to define the state of deformation; however, it is customary to add additional *pseudoinvariants* for anisotropic material (e.g., tendon, and ligament). A common pseudoinvariant for transversely isotropic material is defined as [40, 205]

$$I_4^\alpha := \mathbf{M}^\alpha : \mathbf{C}^\alpha, \quad (4.16)$$

In this equation, \mathbf{M}^α is a second-order structure tensor defined as

$$\mathbf{M}^\alpha := \mathbf{e}_\gamma^\alpha \otimes \mathbf{e}_\gamma^\alpha, \quad \text{where} \quad \mathbf{e}_\gamma^\alpha := \frac{\mathbf{\Pi}^\alpha \mathbf{e}_\gamma^0}{\|\mathbf{\Pi}^\alpha \mathbf{e}_\gamma^0\|}. \quad (4.17)$$

Here, \mathbf{e}_γ^α is a unit vector on the dominant fiber direction in the generation α reference configuration. Therefore, the second Piola-Kirchhoff stress (\mathbf{S}) in terms of deformation

invariants reads as

$$\mathbf{S}(\mathbf{F}, w^\alpha, \mathbf{\Pi}^\alpha) = \sum_{\alpha} w^\alpha (\mathbf{\Pi}^\alpha)^{-1} \left(\sum_{i=1}^4 2 \frac{\partial \psi}{\partial I_i^\alpha} \frac{\partial I_i^\alpha}{\partial \mathbf{C}^\alpha} \right) (\mathbf{\Pi}^\alpha)^{-T}, \quad (4.18)$$

where the derivatives of the deformation invariants are

$$\frac{\partial I_1^\alpha}{\partial \mathbf{C}^\alpha} = \mathbf{I}, \quad \frac{\partial I_2^\alpha}{\partial \mathbf{C}^\alpha} = I_1^\alpha \mathbf{I} - \mathbf{C}^\alpha, \quad \frac{\partial I_3^\alpha}{\partial \mathbf{C}^\alpha} = I_3^\alpha (\mathbf{C}^\alpha)^{-1}, \text{ and } \frac{\partial I_4^\alpha}{\partial \mathbf{C}^\alpha} = \mathbf{M}^\alpha. \quad (4.19)$$

The Cauchy stress (\mathbf{T}) is then obtained from the second Piola-Kirchhoff stress (Eq. (4.18)) as $\mathbf{T} = J^{-1} \mathbf{F} \mathbf{S} \mathbf{F}^T$ (Eq. (2.6)), where $J = \det(\mathbf{F})$. By using the relative deformation gradient tensor, defined earlier in Eq. (4.1), the Cauchy stress tensor for each bond type is

$$\mathbf{T}(\mathbf{F}, w^\alpha, \mathbf{\Pi}^\alpha) = \frac{1}{J} \sum_{\alpha} w^\alpha \mathbf{F}^\alpha \left(\sum_{i=1}^4 2 \frac{\partial \psi}{\partial I_i^\alpha} \frac{\partial I_i^\alpha}{\partial \mathbf{C}^\alpha} \right) (\mathbf{F}^\alpha)^T, \quad (4.20)$$

and by defining the contribution of each generation (\mathbf{T}^α) as [136]

$$\mathbf{T}^\alpha(\mathbf{F}^\alpha) := \mathbf{F}^\alpha \left(\sum_{i=1}^4 2 \frac{\partial \psi}{\partial I_i^\alpha} \frac{\partial I_i^\alpha}{\partial \mathbf{C}^\alpha} \right) (\mathbf{F}^\alpha)^T, \quad (4.21)$$

the Cauchy stress tensor for a specific bond type reads as

$$\mathbf{T}(\mathbf{F}, w^\alpha, \mathbf{\Pi}^\alpha) = \frac{1}{J} \sum_{\alpha} w^\alpha \mathbf{T}^\alpha(\mathbf{F}^\alpha). \quad (4.22)$$

Similar to energy, the above equation indicates that the Cauchy stress of a bond type is the weighted sum of the contributions from all the generations of that bond type.

So far, we have described the fundamental formulation for states of energy and stress in terms of state variables ($\mathbf{F}, w^\alpha, \mathbf{\Pi}^\alpha$). In the following sections, we will describe the energy relations and kinetics of bonds to describe the states of energy and stress in a reactive material.

4.2.3 Reactive bond kinetics

In general, the reactive bonds break and reform (react) when subjected to loading. This process produces the evolution of the states of energy and stress (Eqs. (4.11) and (4.22)). As an example, for a system with one type of bonds, after a unit step deformation the bonds start breaking and their number fraction (w^0) starts to decrease (Fig. 4.2). Simultaneously, the broken bonds reform to a new state, initiating a new generation, where the number fraction of this new generation (w^1) increases over time. In the absence of damage, according to Eq. (4.10) the sum of the number fraction of the breaking and reforming bonds is one (i.e., $w^0(t) + w^1(t) = 1$). As a result, the free energy for a step deformation is

$$\Psi(\mathbf{F}, w^0, w^1, \mathbf{\Pi}^0, \mathbf{\Pi}^1) = w^0(t)\psi(\mathbf{C}^0) + w^1(t)\psi(\mathbf{C}^1). \quad (4.23)$$

If the bonds reform in a stress-free fashion ($\mathbf{C}^1 = \mathbf{I}$), without further loading all of the energy would be dissipated. That is,

$$\dot{\Psi} = \dot{w}^0(t)\psi(\mathbf{C}^0) < 0, \text{ and } \lim_{t \rightarrow \infty} \Psi = 0, \quad (4.24)$$

where the ‘dot’ notation stands for time derivative. To determine the rate of breakage of bonds, a kinetics rate equation is used. The general form of the kinetics rate equation may be written as

$$\dot{w}^\alpha = \Upsilon(w^\alpha, \mathbf{\Gamma}_i). \quad (4.25)$$

In this equation, $\Upsilon(\cdot)$ is a negative-valued function of the available reactants (breaking bonds of w^α) and other state variables such as relative deformation ($\mathbf{\Gamma} = \mathbf{F}^\alpha$) [10], temperature ($\Gamma = \theta$) [239], or for polymeric macro molecules, geometrical characteristics of bonds such as the end-to-end distance and directional angles [139,218]. Despite features that can be added to the rate equation, there are general conditions that need to be satisfied. First, any rate equation should not result in a negative number fraction for any bond generation. Secondly, it should induce a breaking bond number fraction

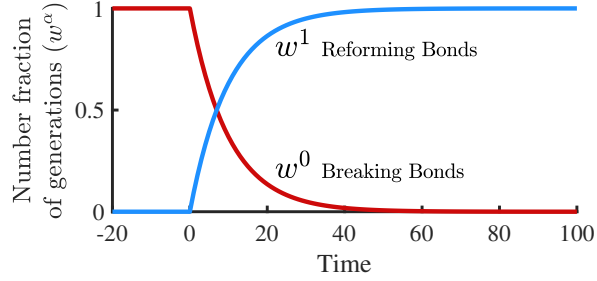


Figure 4.2. Example of bonds with first-order rate equation. After a step deformation at $t = 0$, the bonds start to break (w^0), and simultaneously reform to a new state (w^1). With no further loading, all the bonds eventually break and reform to the new configuration as $t \rightarrow \infty$ (in this example $\tau = 10$).

that asymptotically decays to zero in the limit of infinite time. In this paper, we used the first-order relation, which is the simplest form of a kinetics rate equation satisfying the above conditions:

$$\dot{w}^\alpha = -\frac{1}{\tau}w^\alpha. \quad (4.26)$$

In the above equation τ is the time constant of reaction that controls the rate of breakage and reformation. When multiple consecutive steps of deformation occur at $t^\alpha \in \{t^0, t^1, t^2, \dots, t^n\}$, the number fraction resulting from each deformation for this first-order system is (Fig. 4.3A) [10]

$$w^\alpha(t) = \begin{cases} f^\alpha(t) & t^\alpha < t \leq t^{\alpha+1} \\ f^\alpha(t^{\alpha+1}) \exp(-(t - t^\alpha)/\tau) & t^{\alpha+1} < t \end{cases}. \quad (4.27)$$

In the above relation $f^\alpha(t) = 1 - \sum_{(\alpha; t^\alpha < t)} w^\alpha(t)$ according to Eq. (4.10) that describes the reformation of bonds. The dependence of the rate of breakage on the number fraction of breaking bonds results in an asymptotic exponential decay of bonds. Note that Eq. (4.27) can only be used for first-order kinetics with non-varying time-constant, and for a general rate equation, the number fraction of bonds is numerically calculated from Eqs. (4.10) and (4.25).

4.2.4 Bond types

The state of energy (Eq. (4.11)) for a given bond type depends on the number fraction (w^α) of bonds and their reference deformation gradient ($\mathbf{\Pi}^\alpha$). To characterize the evolution of these variables we define three types of bonds: (1) formative, (2) permanent, and (3) sliding to address viscoelasticity, hyperelasticity, and plastic deformation, respectively.

4.2.4.1 Formative bonds

These bonds have a time constant that is on the order of the characteristic time (t_c) of the experimental observation. That is, $\tau_f/t_c \approx 1$, where $\gamma = f$ stands for formative bond type (Fig. 4.3A). The reference deformation gradient of the new generations of bonds is defined at the current configuration at the time the bonds were initiated (Fig. 4.3D)

$$\mathbf{\Pi}_f^\alpha = \mathbf{F}(t^\alpha). \quad (4.28)$$

Equivalently, for two consecutive generations

$$\mathbf{\Pi}_f^\alpha = \mathbf{\Pi}_f^{\alpha-1} + u(t - t^\alpha)(\mathbf{F}(t^\alpha) - \mathbf{F}(t^{\alpha-1})), \quad (4.29)$$

where $u(\cdot)$ is the unit step function. In this case, during a sustained deformation the energy and stress of the system asymptotically decays as the bonds break, resulting in a fluid-like behavior; a transient viscoelastic mechanical response with zero equilibrium stress.

4.2.4.2 Permanent bonds

Permanent bonds represent a special case of kinetics rate, where the rate of breakage of bonds is extremely slow ($\tau_p/t_c \rightarrow \infty$, $\gamma = p$) (Fig. 4.3B). As a result, only one generation of bonds exists ($w_p^0 = 1$) and the reference deformation gradient of that generation is (Fig. 4.3E)

$$\mathbf{\Pi}_p^\alpha = \mathbf{I}. \quad (4.30)$$

Since the bonds are intrinsically hyperelastic (Eqs. (4.8) and (4.14)), the overall behavior of permanent bonds is hyperelastic, where the states of energy and stress are independent of the history of deformation.

4.2.4.3 Sliding bonds

Sliding bonds represent another special case, where the rate of breakage and reformation of bonds is extremely fast compared to the characteristic time ($\tau_s/t_c \rightarrow 0$, $\gamma = s$) (Fig. 4.3E). In this case, if the bonds could reform to the current configuration, all the energy would immediately be dissipated. If the newly formed bonds have a different reference deformation gradient $\mathbf{\Pi}_s^\alpha$ than the current configuration, they slide (Fig. 4.3F). This implies that the bonds are reforming in a loaded state, and only part of the energy is used for the sliding process and the rest is stored. Since $\mathbf{\Pi}_s^\alpha$ is a state variable, by selecting appropriate constitutive relations the sliding process can be made to produce plastic deformation.

The evolution of $\mathbf{\Pi}_s^\alpha$ is governed by a set of constitutive relations. Following from the classical theory of plasticity [112, 201] we formulated the evolution of the sliding reference deformation gradient using a sliding condition and sliding rule in a rate-independent formulation. Similar to Eq. (4.29) the sliding process is incremental from one generation to the next, i.e.,

$$\mathbf{\Pi}_s^\alpha(t) = \mathbf{\Pi}_s^{\alpha-1}(t^\alpha) + u(t - t^\alpha)\Delta\mathbf{\Pi}_s^\alpha, \quad (4.31)$$

where $\Delta\mathbf{\Pi}_s^\alpha$ is an incremental infinitesimal change to the reference deformation gradient due to sliding. Note that the zeroth generation's reference deformation gradient is the identity tensor ($\mathbf{I} = \mathbf{e}_i \otimes \mathbf{e}_i$). Although the change is infinitesimal, it does not imply that $\mathbf{\Pi}_s^\alpha$ is infinitesimal, nor that the incremental nature of the sliding process goes away, no matter how small the sliding would be.

The sliding only occurs when the sliding condition is met. Otherwise, bonds do not break and due to intrinsic hyperelasticity assumption they behave similarly to

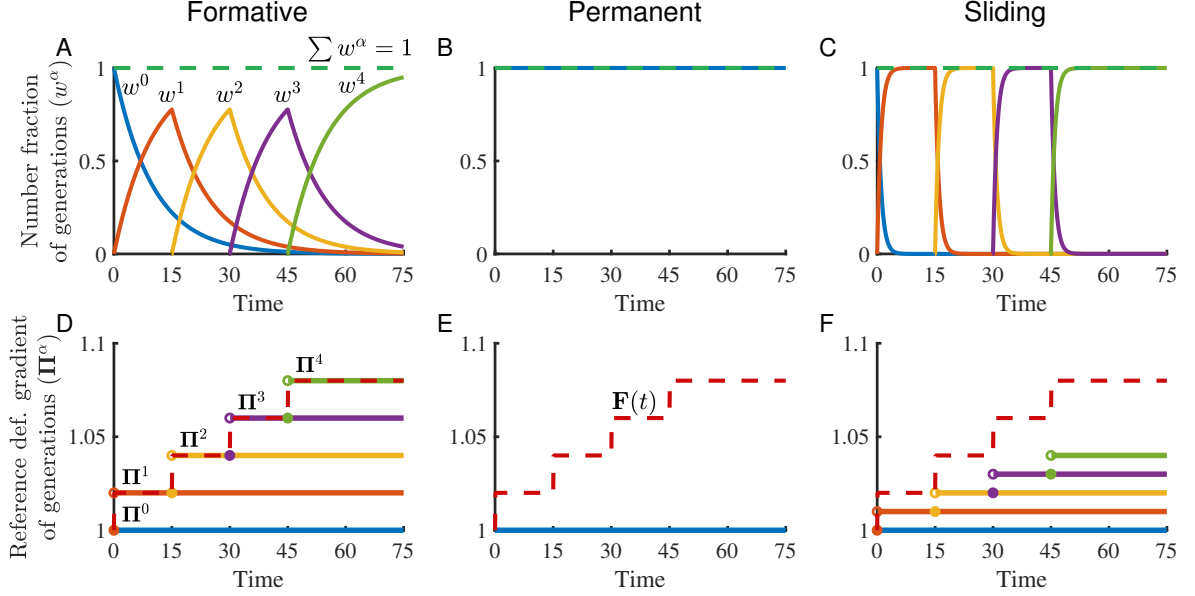


Figure 4.3. Consecutive step deformations and multiple generations (A-C) Number fraction of multiple generations initiated at four consecutive step deformations at $t = 0, 15, 30, 45$ with a first-order rate equation, and (D-F) their corresponding reference deformation gradients. (A,D) Formative bonds (B,E) Permanent bonds (C,F) Sliding bonds. (A-C) For the number fraction graphs, the sum of all of the generations is shown with a horizontal green dashed line. (D-F) The deformation stretch is shown with a red dashed line on reference configuration graphs. Note that $\mathbf{\Pi}^\alpha$ in general is a second-order tensor, and we used a one-dimensional representative for more convenient illustration.

permanent bonds. The sliding condition (analogous to yield condition) is defined as

$$\varphi_s(\Xi_s, r_s) := \Xi_s - r_s \leq 0, \quad (4.32)$$

where Ξ_s is the sliding variable and r_s is the sliding threshold, where all are scalar. The sliding variable is a function of deformation, or equivalently the invariants of deformation:

$$\Xi_s = \hat{\Xi}_s(\mathbf{C}) \equiv \hat{\Xi}_s(I_1, I_2, I_3, I_4). \quad (4.33)$$

The sliding threshold r_s is defined as the maximum value of Ξ_s obtained in the history of deformation [199]

$$r_s := \max \left\{ (r_0)_s, \max_{\tilde{t} \in (-\infty, t]} \Xi_s(\tilde{t}) \right\}. \quad (4.34)$$

The initial value of r_s before any loading is the initial sliding threshold denoted by

$(r_s)_0$, which is a material property. Equations (4.32) and (4.34) indicate $\varphi_s(\Xi_s, r_s) \leq 0$, which corresponds to the physically admissible deformations [201]. Sliding can only be initiated when $\varphi_s = 0$ (necessary condition). To determine the sufficient condition, we need to include the loading direction by defining the second order tensorial normal to the sliding surface ($\varphi_s = 0$)

$$\mathbf{N}_s := \frac{\partial \varphi_s}{\partial \mathbf{C}} \Big|_{\varphi_s=0}. \quad (4.35)$$

While the necessary condition for sliding is in place, two scenarios of loading can occur [147]

$$\begin{cases} \mathbf{N}_s : \dot{\mathbf{C}} \leq 0 & \text{(no sliding)} \\ \mathbf{N}_s : \dot{\mathbf{C}} > 0 & \text{(sliding)} \end{cases}, \quad (4.36)$$

where only the second scenario can initiate a sliding behavior. Here, $\dot{\mathbf{C}}$ is the material time derivative of the right Cauchy-Green deformation tensor $\dot{\mathbf{C}} := \mathbf{F}^T \left(\dot{\mathbf{F}} \mathbf{F}^{-1} + \mathbf{F}^{-T} \dot{\mathbf{F}}^T \right) \mathbf{F}$. When the necessary and sufficient conditions of sliding ($\varphi_s = 0$ and $\mathbf{N}_s : \dot{\mathbf{C}} > 0$) are in place, the incremental sliding can be calculated using the sliding rule:

$$\Delta \Pi_s^\alpha = \mathbf{R}(\mathbf{F}, \Pi_s^{\alpha-1}), \quad (4.37)$$

where \mathbf{R} is a second-order tensor function. An example of sliding rule for a medium with a dominant fiber direction would be

$$\Delta \Pi_s^\alpha = \frac{\partial f_s(\Xi_s)}{\partial \Xi_s} \Delta \Xi_s \tilde{\mathbf{M}}^\alpha, \quad (4.38)$$

where f_s is the sliding function, $\Delta \Xi_s$ is the difference between sliding variables of two consecutive generations involved in the sliding process (Eq. (4.31)), and $\tilde{\mathbf{M}}^\alpha$ is a second-order structure tensor. To define $\tilde{\mathbf{M}}^\alpha$ it was assumed that the initial dominant fiber orientation is preserved in the sliding configurations, i.e. $\mathbf{e}^\alpha = \lambda_s^\alpha \mathbf{e}^0$. Therefore, one can show (see the Appendix B)

$$\tilde{\mathbf{M}}^\alpha = \mathbf{e}^0 \otimes \mathbf{e}^0 \quad (4.39)$$

This particular constitutive relation indicates that the configuration of increments of sliding depends on the extent of deformation and the orientation of bonds in the master reference configuration. As another example, for three-dimensional cases where an analytical expression is available for \mathbf{F} , one can choose $\mathbf{\Pi}_s^\alpha = \mathbf{F}(\lambda_s^\alpha)$ [168]. In general, however, for finite strain plastic deformation an analytic expression is not available, and one should use the well established theory of finite-strain plasticity to formulate the intermediate configuration [7, 44, 121].

For completeness, because the reference configuration is time invariant after formation of bonds and the sliding process is incremental (Eq. (4.31)), the rate of sliding for each reforming bond generation is determined using

$$\dot{\mathbf{\Pi}}_s^\alpha = \delta(t - t^\alpha) \Delta \mathbf{\Pi}_s^\alpha(t^\alpha), \quad (4.40)$$

where $\delta(\cdot)$ is the Dirac delta function that denotes the incremental nature of sliding process. This relation will be helpful later in the analysis of the second law of thermodynamics (Section 4.2.6).

4.2.5 Damage of bonds

Damage is an irreversible process that is due to a loss of chemical bonds [113]. This is often observed as a softening behavior that is also referred to as Mullin's effect [145]. The idea of relating damage to molecular bonds in tissue can be traced back as early as [31] for modeling the hysteresis effect. In the current framework, damage of the various bonds (D) was considered as another state variable, where with a damaging load, the broken bonds may not be reformed, which in turn decreases the number of active bonds. That is,

$$\left(\sum_{\alpha} w^\alpha \right)_{\text{Damaged}} = (1 - D) \sum_{\alpha} w^\alpha, \quad (4.41)$$

where D is the damage parameter of a certain bond type and it takes a value between zero and one ($D \in [0, 1]$) [151]. Damage can be applied to each of the bond types (Fig. 4.4). By doing so, the total energy of the bonds decreases as the number fraction of damaged bonds increases. Hence, the free energy is

$$\Psi(\mathbf{F}, w^\alpha, \mathbf{\Pi}^\alpha, D) = (1 - D) \sum_{\alpha} w^\alpha \psi(\mathbf{C}^\alpha). \quad (4.42)$$

which always has a value less than the non-damaged case.

To determine the evolution of damage, similar to the sliding case, the damage condition is defined as

$$\varphi_D(\Xi_D, r_D) := \Xi_D - r_D \leq 0, \quad (4.43)$$

Here, Ξ_D is the damage variable that is a function of deformation invariants

$$\Xi_D = \hat{\Xi}_D(\mathbf{C}) \equiv \hat{\Xi}_D(I_1, I_2, I_3, I_4), \quad (4.44)$$

and r_D is the damage threshold defined as the maximum value of Ξ_D in the past history of deformation [199]. The damage threshold r_D is defined separately for each bond type as

$$r_D := \max \left\{ (r_0)_D, \max_{\tilde{t} \in (-\infty, t]} \Xi_D(\tilde{t}) \right\}. \quad (4.45)$$

The value of r_D before any loading is the initial damage threshold $((r_D)_0)$, which is a material property. Damage occurs when $\varphi_D = 0$ (necessary condition). The loading direction determines the sufficient conditions. By defining the second order tensorial normal to the damage surface ($\varphi_D = 0$) as

$$\mathbf{N}_D := \frac{\partial \varphi_D}{\partial \mathbf{C}} \Big|_{\varphi_D=0}, \quad (4.46)$$

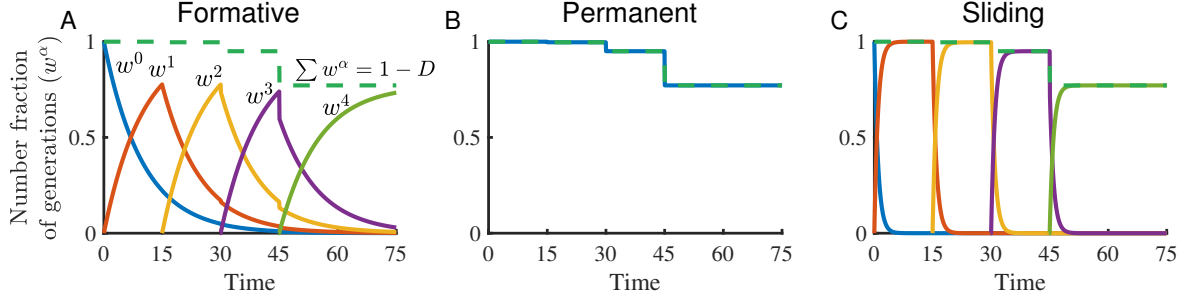


Figure 4.4. Effect of damage on molecular kinetics. Multiple generations initiated at four consecutive step deformations at $t = 0, 15, 30, 45$ with a first-order rate equation with damage shown for (A) formative bonds (B) permanent bonds and (C) sliding bonds, the sum of bonds declines after each step of loading until the final value of 0.75 ($D = 0.25$).

and by using the following normality conditions [199]

$$\begin{cases} \mathbf{N}_D : \dot{\mathbf{C}} \leq 0 & \text{(no damage)} \\ \mathbf{N}_D : \dot{\mathbf{C}} > 0 & \text{(damage)} \end{cases}; \quad (4.47)$$

damage only occurs when ($\varphi_D = 0$ and $\mathbf{N}_D : \dot{\mathbf{C}} > 0$). Thus, during a damaging load, the damage parameter increases according to the damage rule

$$\dot{D} = \frac{\partial f_D(\Xi_D)}{\partial \Xi_D} \dot{\Xi}_D, \quad (4.48)$$

where $f_D(\Xi_D)$ is the damage function. Note that the damage variable (Ξ_D) is different from damage parameter (D), where D is the number fraction of permanently broken bonds.

4.2.6 Implications of the second law of thermodynamics

As a consequence of the second law (as shown in detail in the Appendix C), the bonds are ‘second-law compatible’ if appropriate constitutive relations are used. Formative and permanent bonds are second-law compatible when appropriate kinetics relation is used, and for sliding bonds, the change in reference configuration (Eq. (4.38)) needs to be defined so as to satisfy positive dissipation of energy (Appendix C). For damage, f_D (Eq. (4.48)) needs to be selected to guarantee $\dot{D} \geq 0$ (e.g., cumulative

distribution function of a continuous statistical distribution). Examples of appropriate constitutive relations will be provided in Section 4.3.

4.2.7 Summary of formulation

In summary, a reactive inelasticity model was formulated that defines different types of bonds corresponding to different mechanical behaviors. The combination of bond types should be selected according to the desired mechanical behaviors (as described in Section 4.2.4). In selecting the constitutive relations it is perhaps more convenient to take the discrete steps that are outlined in Table 4.1. In the following section, several illustrative examples are provided that both help in understanding the model and also to exemplify some practical applications to mechanics of soft tissue, where reactive inelasticity can be useful.

4.3 Illustrative Examples

To demonstrate key features of the reactive inelasticity (RIE) framework we provide three numerical examples. First, the sensitivity of formative bonds to the kinetics rate is demonstrated using a Heaviside step loading that shows transitions between different bond types (Example I). Second, we simulate the stress response of an increasing cyclic loading by using a fiber-exponential constitutive relation that is commonly used in tissue mechanics, and we compare the stress response between non-damaged and damaged cases (Example II). Finally, incremental stress relaxation with softening is presented for an anisotropic case, which has importance to understand mechanisms of plastic deformation and damage in tissue. This is done by using a combination of formative bonds and either sliding bonds or permanent bonds with damage (Example III). The model is implemented as a Matlab function using a custom written code intended for uniaxial deformations. The source code and details of implementation are provided at Appendix D and are accessible online¹.

¹ <https://github.com/BabakNSafa/ReactiveBond>

Table 4.1. Summary of structure of a reactive bond type’s constitutive relations.

Step 1	Select the bond types (i.e., formative, permanent, sliding)
Step 2	Select the kinetics relation (e.g., Eq. (4.26))
Step 3	Select the intrinsic hyperelasticity relation $\psi_\gamma(\mathbf{C}^\alpha)$ (e.g., neo-Hookean)
Step 4	If sliding bonds, select appropriate constitutive relations: Sliding variable (Ξ_s) (Eq. (4.33)) Sliding rule and function (f_s) (Eq. (4.38))
Step 5	If damage is included, select appropriate constitutive relations: Damage variable (Ξ_D) (Eq. (4.44)) Damage rule and function (f_D) (Eq. (4.48))

For all of the examples, the axial component of the Cauchy’s stress tensor (i.e., $T = T_{33}$) was used to represent the state of stress during a uni-axial isochoric deformation

$$\mathbf{F} = \hat{\mathbf{F}}(\lambda(t)) := e_i \otimes e_i \frac{1}{\sqrt{\lambda}} + e_3 \otimes e_3 \left(\lambda - \frac{1}{\sqrt{\lambda}} \right) \quad i = 1, 2, 3. \quad (4.49)$$

The following constitutive relations were implemented in the steps outlined in Table 4.1:

- **Step 1- Bond type selection:** The bond type was selected depending on the expected mechanical behavior. Formative bonds were used for a viscoelastic behavior with zero equilibrium stress, permanent bonds for a hyperelastic behavior, and sliding bonds were used for plastic deformation. Note that for Example III, which includes a combination of bonds, the response was calculated independently for each bond type and added according to Eq. (4.11).
- **Step 2- Kinetics relation:** For all of the examples, a first-order kinetics relation was used (Eq. (4.26)).
- **Step 3- Intrinsic hyperelasticity:** Three types of non-linear constitutive relations were used. First, we used the neo-Hookean relation in Example I. This is the simplest non-linear constitutive relation and was used to demonstrate the general behaviors of the model, where the potential energy is

$$\psi_{NH}(I_1) = C_1(I_1 - 3). \quad (4.50)$$

Here, C_1 is the independent model parameter with dimensions of stress.

Second, for relevance to tissue applications, in Examples II and III we used a one-dimensional exponential constitutive relation with a non-zero stiffness only in the e_3 direction (fiber direction) in tension [100, 189]

$$\psi_{EF}(I_4) = C_2 \left(\exp [C_3(I_4 - 1)^2] - 1 \right) u(I_4 - 1), \quad (4.51)$$

where C_2 and C_3 are positive-valued model parameters.

Third, for showing a three-dimensional tissue mechanics application, we used a Holmes-Mow material (Example III)

$$\psi_{HM}(I_1, I_2, I_3) = \alpha_0 \left(I_3^{-\beta} \exp [\alpha_1(I_1 - 3) + \alpha_2(I_2 - 3)] - 1 \right). \quad (4.52)$$

In this relation, α_0 is a positive number with the dimension of stress and $[\beta, \alpha_1, \alpha_2]$ are positive non-dimensional numbers. To comply with the energy- and stress-free reference configuration, $\beta = \alpha_1 + 2\alpha_2$ must be satisfied [88]. Note that the Holmes-Mow model parameters are related to the more familiar infinitesimal linear-elastic parameters as:

$$\alpha_1 = \frac{E/\alpha_0}{4(1+\nu)} - \alpha_2, \text{ and } \alpha_2 = \frac{(E/\alpha_0)\nu}{4(1+\nu)(1-2\nu)}, \quad (4.53)$$

where E is the Young's modulus, and ν is the Poisson's ratio. Hence, $[E, \nu]$ were preferred instead of the original Holmes-Mow parameters.

- **Step 4- Sliding:** The overall stretch was selected as the sliding variable

$$\Xi_s = \lambda = \sqrt{I_4}. \quad (4.54)$$

To describe the sliding rule for the one-dimensional fiber intrinsic hyperelasticity relation (Example II) (Eq. (4.51)) the form represented in Eq. (4.38) was employed with the sliding function as

$$f_s(\Xi_s) = c(\Xi_s - (r_s)_0)^b, \quad (4.55)$$

where the constant parameters $[c, b]$ are dimensionless positive numbers, and $(r_0)_s$ is the initial sliding threshold. Also, e_3 was taken as the sliding direction and was used to define structural direction tensor as $\tilde{\mathbf{M}} := e_3 \otimes e_3$ (Eq. (4.38)). In this case, as long as $\lambda_s^{N-1} < \lambda_s^N < \lambda$ the condition of second law is satisfied, and it can be easily verified that $(-\partial\psi_{EF}(\lambda/\lambda_s^N)/\partial\lambda_s^N)(\lambda_s^N - \lambda_s^{N-1}) > 0$, which proves the compatibility of these constitutive relations with the second law (for details see the Supplementary document). For the three-dimensional constitutive relation cases it was assumed that $\mathbf{\Pi}_s^N$ takes the form of $\hat{\mathbf{F}}(\lambda_s^N)$ during sliding, where by using the Taylor series expansion, it can be shown that all of the constitutive

equations are compatible with the second law of thermodynamics (Supplementary document).

- **Step 5- Damage:** For the case with damage of bonds, similar to sliding, the overall stretch was used as the damage variable

$$\Xi_D = \sqrt{I_4}, \quad (4.56)$$

and a Weibull's cumulative distribution function was used as the damage function [151]

$$f_D(\Xi_D) = 1 - \exp\left\{\left[-\left(\frac{\Xi_D - (r_D)_0}{l-1}\right)^k\right]\right\}, \quad (4.57)$$

where k is the shape parameter, l is the scale parameter, and $(r_0)_D$ is the initial damage threshold.

4.3.1 Model parameters used in the illustrative examples

The illustrative examples were designed using the noted constitutive relations to demonstrate the important features of the framework with no particular focus on certain tissues; however, in practice, specific constitutive relations should be employed to use the framework for successfully modeling of the inelastic behaviors of tissue. The models generated with this framework may have different number of model parameters. Thus, in general, no specific number of parameters could be associated with the framework. Below we have listed the model parameters used for different examples.

Table 4.2. Parameters used for dynamic response of single bond types (Fig. 4.6).

	τ	C_2	C_3	c	b	$(r_0)_s$	k	l	$(r_0)_D$
Formative	10	0.1	40	-	-	-	-	-	-
Permanent	10^{10}	0.1	40	-	-	-	2	1.04	1.03
Sliding	0.01	0.1	40	9	2	1.01	-	-	-

Table 4.3. Parameters used for the incremental stress relaxation response tests (Fig. 4.7).

	τ	C_2	C_3	E	v	α_0	c	b	$(r_0)_s$	k	l	$(r_0)_D$
Formative	10	0.1	40	-	-	-	-	-	-	-	-	-
Permanent	10^{10}	-	-	50	0.3	0.1	-	-	-	2	1.05	1.02
Sliding	0.01	-	-	50	0.3	0.1	8	2	1.02	-	-	-

4.3.2 Sensitivity of the formative bonds to the kinetics rate (Example I)

As discussed in Section 4.2, the kinetics rate is the predominant difference between various bond types. To show this, we simulated the response of formative bonds to a Heaviside step deformation at a wide range of reaction kinetics rate, where the only variable was the time constant (τ_f) (Fig. 4.5). For a large τ_f (slow kinetics rate) the response approaches the hyperelastic behavior (permanent bonds), and as τ_f gets smaller (high kinetics rate) the response approaches a singular stress behavior (sliding bonds). For all of the kinetics rates, the response at $t = 0$ is the same and equal to the hyperelastic stress for that deformation. This response at $t = 0$ also corresponds to the peak stress response of the initial generation in Eqs. (4.23) and (4.24).

This simple example lies at the heart of reactive inelasticity and demonstrates the consistency of inelastic behaviors that are all based on the kinetics of breaking and reforming bonds. In what follows, more complex loading scenarios are investigated that are all based on a summation of incremental step deformations.

4.3.3 Cyclic loading and damage (Example II)

Example II demonstrates the response of single bond types with the model parameters listed in Table 4.2 to a cyclic loading (Fig. 4.6A). In response, formative bonds dissipate energy in a cyclic hysteresis (Fig. 4.6B), while the permanent bonds have a hyperelastic response that is independent of history of deformation (Fig. 4.6C). The sliding bonds undergo plastic deformation that is evident by the shift in the point of zero stress after each cycle, while there is no change in stiffness during the consecutive loading parts (Fig. 4.6D). Note that the sliding bonds account for strain softening that results in a decrease in stress after reaching the peak stress (points 3 and 4 in Fig. 4.6D), and it is different from strain hardening that is associated with plasticity in metals and some engineering polymers. Further, by adding damage (decreasing the total number of bonds) the Mullin's effect was captured for all three types of bonds. In addition to decreasing stiffness and the corresponding stress values, the damage increases the

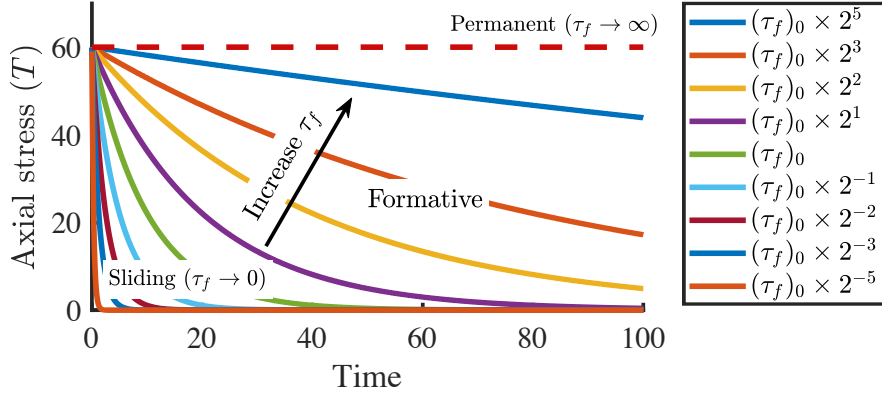


Figure 4.5. Example I: Time response of formative bonds to a Heaviside-step deformation in a large range of kinetics rates. The kinetics rate is controlled by time constant of reaction where $(\tau_f)_0 = 10$ and the range of time constants is covered by multiplying $(\tau_f)_0$ with powers of two. Formative bonds show an asymptotic decay in Cauchy stress during a sustained loading, whereas for large values of τ_f (slow kinetics rate) the response approaches a hyperelastic behavior (permanent bonds) marked with dashed red line, and at small τ_f (high kinetics rate), the stress response approaches a singular behavior that is immediately decays to zero (sliding bonds). The step deformation is $\lambda(t) = 1.1u(t)$ and the neo-Hookean intrinsic hyperelasticity parameter is $C_1 = 100$.

difference between the loading and unloading parts of the stress response. This results in increased hysteresis and further dissipation of energy (Fig. 4.6E, F, and G).

The expansion of sliding and damage thresholds are shown in Fig. 4.6A by the dashed lines. It is evident from the simulations that the behavior of bonds, especially permanent bonds with damage and sliding bonds are similar. However, certain characteristics are unique to each bond type. For example, contrary to sliding bonds, there is no shift in reference configuration for permanent bonds with damage.

4.3.4 Incremental stress relaxation with softening and anisotropy (Example III)

In Example III a typical combination that may be used to model anisotropic response of tissue in a stress relaxation test is demonstrated that also includes softening. Softening in tissues often occurs at high deformations [131,216]. It is not possible to distinguish between damage and plastic deformation solely by loading the tissue in tension and analyzing the stress response. This is demonstrated in the example by

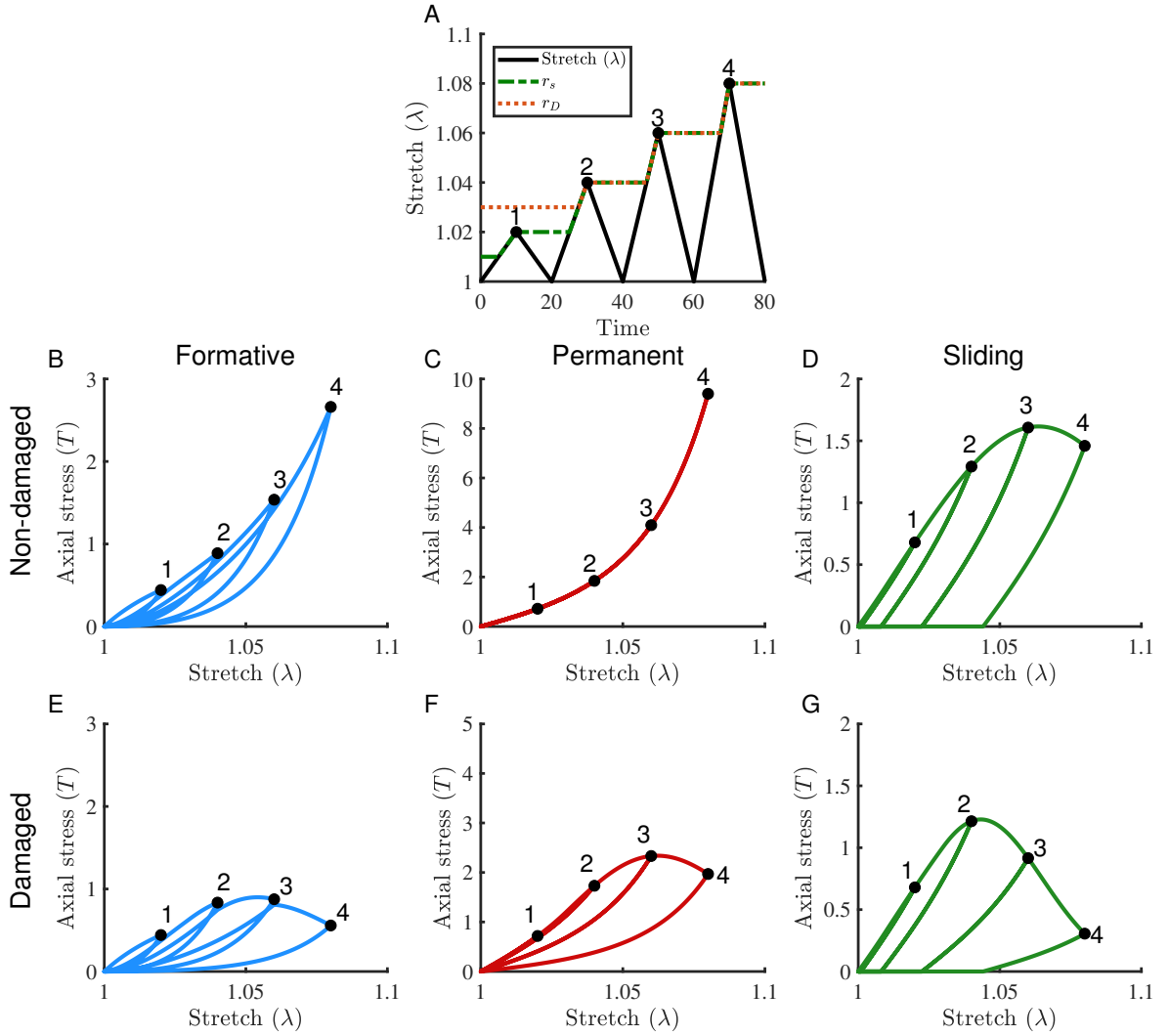


Figure 4.6. Example II: Cyclic loading and damage (A) an increasing cyclic loading protocol applied for non-damaged (B) formative, (C) permanent, (D) sliding bonds. When damage is added to the response for (E) formative, (F) permanent, and (G) sliding bonds, all the bond types show a softening behavior. The evolution of sliding and damage thresholds is also shown in (A) in response to loading and unloading phases, where sliding starts after $\lambda = (r_s)_0 = 1.01$, and damage after $\lambda = (r_D)_0 = 1.03$.

using a combination of formative bonds and either sliding bonds, or permanent bonds with damage (Fig. 4.7). In these examples, formative bonds account for the transient stress response in axial direction, and sliding (or permanent bonds) produce the equilibrium part of the stress response (model parameters in Table 4.3). Identical behaviors are observed during ramp and relaxation loading phases (Fig. 4.7). However, during

unloading it is evident that the reference configuration is shifted when implementing the sliding bonds, where for permanent bonds with damage there is no shift in the zero-stress configuration.

Experimental evaluation of this shift in the reference configuration in soft tissue is often challenging due to non-linearity in stress-strain behavior, when the initial stiffness is low that gradually increases by further deformation (toe-region effect). However, by having a theoretical framework for both of the candidate mechanical behaviors (i.e., plastic deformation and damage) it is possible to fit the models to the loading phase and make predictions about either the unloading phase, or other experimental results (e.g., cyclic loading in Example II) to assess the success of the model in predicting the experimental data, and thus evaluating the contribution of each of the aforementioned inelastic behaviors in tissue [182].

4.4 Discussion

This study provides a structurally-inspired framework for modeling inelasticity in tissue. It uses a thermodynamic scheme, where internal state variables and kinetics of molecular bonds are employed to capture the major inelastic behaviors of tissue. This framework consistently addresses a range of inelastic behaviors. The formative, permanent, and sliding bonds correspond to viscoelastic behavior with zero equilibrium stress, hyperelastic response, and plastic deformation, respectively. Additionally, the formulation of bond kinetics allows for the inclusion of damage by reducing the number of bonds, which introduces damage as an inelastic behavior to all of the bond types. Any combination of the bond types can be employed to model various kinds of inelastic behaviors, such as a combination of formative bonds and permanent bonds with damage to model a viscoelastic behavior with softening.

The reactive inelasticity framework uses ISV formulation, where it is usually assumed that the variables are “hidden”; however, despite the similar mathematical formulation, the variables used herein can be physically measured, and as suggested by Ateshian and co-workers are “observable state variables” [10, 151]. Connective tissues

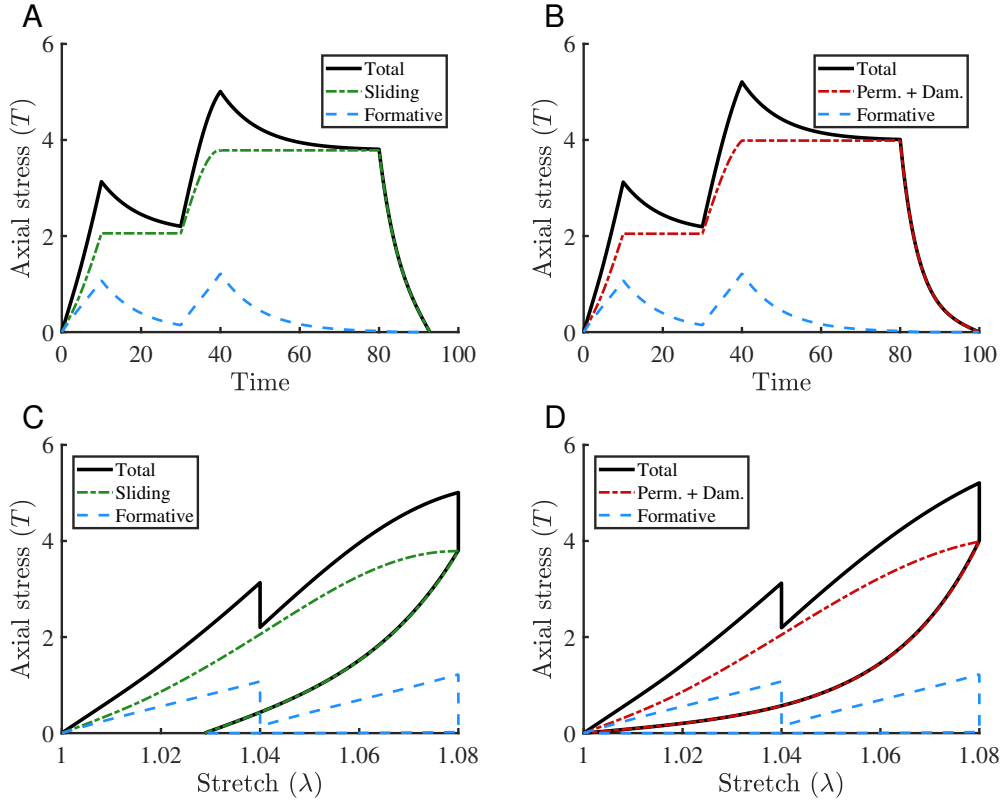


Figure 4.7. Example III: Incremental stress relaxation with softening for (A,C) formative and sliding bonds, and (B,D) formative bonds with permanent bonds and damage. The effect of selection of either sliding bonds or permanent bonds is only observed during unloading. When the sliding bonds are used there is a shift in the reference configuration (C) which is not true for permanent bonds with damage (D).

matrix is mostly made of various types of collagen that are cross-linked. These cross-links are formed via several mechanisms including enzymatic lysyl oxidase-mediated and non-enzymatic glycation-induced cross-links to produce larger collagenous structures [57, 177]. The mechanical properties of collagenous material are sensitive to the density, structure and properties of these cross-links [47]. Several studies support a correlation between mechanical loading and the state of molecular bonding as described below. Fourier transform-Raman spectroscopy during tendon's incremental stress relaxation tests [137], and thoracic aortic wall's ramp-to-failure [81] show that the protein

conformation is highly dependent on mechanical loading. Additionally, when overloaded, collagen fibrils show local deformities (kinks) that contain denatured-collagen-rich regions [86,227]. In fact, the denatured collagen density is closely correlated with reactive damage parameter [151]. Recent advancements in using collagen hybridizing peptides (CHP) provided new opportunities to visualize the spatial distribution and level of disruption in these regions after mechanical overloading [126,212,249]. Furthermore, using in-silico molecular dynamics experiments, two potential mechanisms of molecular disruption, shear and tension dominant, were suggested and these closely resemble the sliding and damage processes modeled here with RIE [249]. However, despite these advances demonstrating a role for molecular bonds as observable state variables, more experimental work needs to be done to elucidate structural mechanisms of inelasticity in terms of molecular bonding.

The reactive inelasticity framework is a generalization of the reactive viscoelasticity model [10], where an inclusive and consistent treatment of inelastic processes is provided. The reactive viscoelasticity model of Ateshian provided the essential concepts of weak and strong bonds that correspond to formative and permanent bonds, respectively. We chose the terminology of formative and permanent bonds because of their analogy to kinetics rate of bonds and their behavior. Additionally, in contrast to [10] we based our formulation on the number fraction of bonds rather than mass fraction, which emphasizes that in general, bonds are levels of energy and individual bonds do not correspond to a physical mass. Although at the first sight these parameters appear to be equivalent, due to their non-dimensional nature, this non-inertial bond assumption is particularly important when considering the singular accelerations arising in the case of sliding bonds. Massless bonds keep the model in the realm of admissibility in the general sense. Further, by making these generalizations we showed that the bonds are interchangeable at the extremes of kinetics rate, where the behavior of formative bonds is hyperelastic (permanent bonds) in the limit of slow kinetics rate (Fig. 4.5), and at high rates of bond kinetics formative bonds turn into sliding bonds that correspond to a plastic deformation (Fig. 4.6).

Plastic deformation has been experimentally observed in tissue at the macro- [134], micro- [120, 216], and nano-scale [198]. Several phenomenological ISV modeling approaches have been taken to address these phenomena that often are focused to address specific inelastic behaviors and usually omit the relationships between different inelastic behaviors and their mechanisms [60, 66, 134, 160, 247]. In the current framework, we particularly focused on providing a consistent formulation between different inelastic behaviors and their structural relevance. It should be noted that the concept of sliding bonds is a fundamentally different concept compared to classic plasticity, and it rather should be compared to the theory of permanent set in polymer mechanics (rubber-like material) [48]. In a similar framework, for cross-linked polymers a molecular bond approach has been used to model stress relaxation and plastic necking instability [139, 140]; however, in that theory, only plastic necking rather than general plastic deformation was addressed, and therefore, their formulation does not explicitly provide for the shift in unloaded configuration that is observed in tissue, such as non-recoverable interfibrillar sliding [120]. In our model, the generation reference deformation gradient ($\mathbf{\Pi}^\alpha$) is a state variable that is directly related to the plastic deformation and thus is an observable variable accounting for the shift in unloaded configuration of the material.

Damage was applied to each of the bond types regardless of their kinetics rate. This allowed for modeling the effect of damage on different components of structure that produce the mechanical behavior of material, such as degradation in the viscous components of a viscoelastic behavior without affecting its elastic part. Previously, a similar concept was used to study damage in cartilage that was only applied to the permanent bonds. This resulted in the damage effect being limited to the equilibrium behavior [151]. The reduction in number fraction of active bonds results in a decrease in the ability of material to absorb energy, which provides a generalized definition of damage as a behavior. By adding this ability, it is possible to model mechanical behavior up to rupture, where, if the formative bonds could not be damaged, no rupture could occur. Another benefit of this definition is in that it forms a clear theoretical

basis for distinction between plastic deformation and damage. As shown in Fig. 4.6, plastic deformation alone does not result in a decrease in stiffness; however, adding damage would cause a reduction in stiffness, which is a common mechanical property used to assess the extent of damage in a material. By using the current theoretical framework for addressing damage and other forms of inelastic response that was provided in this study, it is possible to elucidate the mechanisms and role of each inelastic behavior in the mechanical response of tissue from the experimental stress response of the material. One future direction, for example, is using a specific loading profile with repeated scenarios (e.g., loading, unloading and reloading) to curve fit different versions of reactive inelasticity and using the fit parameters to predict an independent experimental mechanical behavior. From the quality of the predictions, one can assess the relevance of the involved inelastic behaviors and their contribution; this is studied in the following chapter.

In this framework, one of the limitations may be that we made a continuum body assumption to relate the molecular energy to the macro-scale mechanical behavior, where hierarchical structural effects, as well as statistical considerations for molecular bonding were not included; however, the simplicity of the model and its ability to reproduce a spectrum of macro-scale behaviors were chosen here over complexity of formulation. Additionally, damage was modeled as a scalar variable that may overly constrain a generalized three-dimensional case [104]. These issues can be addressed by utilizing multiple bond types with different directional preferences to achieve a desired level of anisotropy [151]. The current formulation does not study the geometry effects, spatial variation of material properties, and or other heterogeneities, which can be incorporated when RIE is solved on a certain geometry. Finally, since tissues have a significant fluid content, the fluid pressurization and poroelastic effects can play an important role in the mechanical response. Those effects were not included in this model, which is a limiting factor for applying this framework to experimental data. However, including poroelasticity with other material models has been studied in depth by others, thus we did not focus on that; where, a multiphasic mixture model

can be used with inelastic solid phase to address fluid flow effects [9, 93, 132].

In conclusion, we have provided a structurally-inspired framework for modeling inelastic behaviors of tissue based on the kinetics of reactive molecular bonds that break and reform in response to mechanical loading. The model addresses viscoelasticity, plastic deformation, and damage of a fibrous structure in an inclusive framework. We introduced three types of molecular bonds: formative, permanent, and sliding that result in viscoelastic, hyperelastic, and plastic deformation behaviors. Damage was applied to each of the bond types by reducing the number fraction of bonds, which consequently decreases the ability of material to absorb energy. All of the aforementioned inelastic behaviors are modeled within the same framework and by using similar sets of constitutive equations. This allows for investigating the mechanisms of inelasticity by providing a comprehensive theoretical basis for analyzing the mechanical response of tissue that can be used to understand mechanical loading induced pathological conditions, to develop more effective treatment protocols, and to engineer replacement tissues.

Chapter 5

EVALUATING PLASTIC DEFORMATION AND DAMAGE AS POTENTIAL MECHANISMS OF INELASTICITY IN TENDON

These findings are published in *Babak N. Safa, Andrea H. Lee, Michael H. Santare, Dawn M. Elliott. 'Evaluating Plastic Deformation and Damage as Potential Mechanisms for Tendon Inelasticity Using a Reactive Modeling Framework,' Journal of Biomechanical Engineering (2019) (<https://doi.org/10.1115/1.4043520>)*

5.1 Introduction

Inelastic mechanical behaviors, as described in Chapter 4, occur during tendon's overload and in loading-induced pathological conditions such as degeneration and tendinopathy [37, 133]. Inelastic behaviors in tissue include viscoelasticity, plastic deformation, and damage. In particular, plastic deformation and damage are associated with stress softening, commonly referred to as Mullin's effect in polymer mechanics [48, 135]. In tissue, softening is observed as a progressive decrease in tensile modulus prior to failure [122, 158, 165, 183] and can be described based on the concepts of plastic deformation and damage. In plastic deformation, there is a shift in the unloaded reference state, and in damage the material loses its ability to absorb energy without a change to the unloaded reference state [3, 48, 125]. These inelastic behaviors can contribute to the development of clinical disorders, such as tendinopathy and rupture by changing the macro-scale mechanical behavior [64] and can also affect tissue degeneration and regeneration, by changing the cell loading [38].

Tendon's mechanical and structural studies support both of the potential mechanisms of plastic deformation [1, 178, 210] and damage [54, 149] for softening. However,

plastic deformation and damage are hard to differentiate experimentally. Plastic deformation and damage cannot be differentiated during the commonly used ramp-to-failure tests due to the similar softening effect of these two mechanisms during loading, and a repeated loading protocol, such as loading and unloading, is essential to quantify plastic deformation and damage. However, even when unloading is added, the low stiffness in the toe-region and viscoelastic behaviors can still limit differentiation between plastic deformation and damage [210]. Structural studies also do not resolve the question: non-recoverable micro-scale sliding [120] supports plastic deformation, collagen denaturation due to mechanical loading [228, 249] supports damage, and the inelastic tensile response of individual collagen fibrils [128, 198] may support both. Despite numerous mechanical and structural studies, tendon’s inelastic behaviors are not well described.

In Chapter 4, we reviewed the reactive inelasticity (RIE) theoretical framework to address the inelastic behaviors of soft tissue by using the kinetics of molecular bonds. This structurally-inspired continuum mechanics framework is an extension of the reactive viscoelasticity model by Ateshian [10] and prior work in polymer mechanics [6, 48, 96, 239], which addresses all three of the aforementioned inelastic behaviors of tissue (i.e., viscoelasticity, plastic deformation, and damage) by using the same constitutive settings at different kinetic rates of bond breakage and reformation. This characteristic makes RIE distinct from other models for tissue’s inelastic behaviors, which address viscoelasticity without softening [52, 171, 245], or include softening by focusing on either plastic deformation [210, 247], damage [53, 75, 125, 149, 151, 224], or their combination [60, 134, 160, 161]. In the RIE framework there are three bond types; formative bonds are used to model a transient viscoelastic behavior, permanent bonds are used for modeling the hyperelastic behavior, and sliding bonds are used for plastic deformation. Damage is added to each bond type by reducing the number fraction of the available bonds Chapter 4. By combining different bond types, a wide variety of mechanical behaviors can be modeled. Hence, the RIE framework provides a comprehensive tool for investigating the inelastic behaviors of tissue by using a unified structurally-inspired theory to model inelasticity.

Our long-term goal is to study tissue inelasticity, bridging the gap between experiments and modeling. The objectives of this chapter are to apply the RIE modeling framework to tendon’s tensile behavior, to evaluate the model performance in fitting the macro-scale experimental data for plastic deformation and damage mechanisms, and to validate the models by predicting an independent experimental dataset. Our previous study on rat tail tendons demonstrated that uniaxial mechanical loading can change both macro-scale mechanical properties and micro-scale structure [120]. However, this experimental study was not designed to distinguish between plastic deformation and damage, and it did not provide numerical measures for inelastic effects. We will show that we can describe the inelastic behaviors in tendon by using RIE-based models specific to plastic deformation (combination of formative bonds and sliding bonds) or damage (combination of formative bonds and permanent bonds). Importantly, for validation we then apply the resulting model parameters to predict results from a separate, independent experiment. This study is significant in that it pursues a systematic approach to elucidate the mechanisms of tissue degeneration and failure, and it provides a path forward for understanding the connection between structural hallmarks of tendon pathology and mechanical behavior.

5.2 Methods

We formulated two material models using the reactive inelasticity (RIE) framework that address either plastic deformation or damage. These models account for physics of tendon by simultaneously addressing: stress stiffening (toe-region), stress-relaxation (viscoelasticity), unloading, and softening. The models were independently fit to the experimental data from Lee and co-workers [120]. We first evaluated the performance of these two models in fitting the experimental data. To validate the model prediction, we applied the resulting model parameters to a separate, independent experiment that measured the stress response of tendon fascicles in constant-rate tensile tests (Szczesny and co-workers [214]).

5.2.1 Reactive inelastic modeling

In the following, we briefly describe the theoretical formulation of RIE and its specific application to this study; for further details the reader is referred to Chapter 4. The RIE framework employs the kinetics of molecular bonds to simulate the inelastic behaviors. There are two levels for categorizations of bonds: “bond types” and “generations”. A bond type, specifies its mechanical behavior (e.g., hyperelastic or plastic deformation). Bonds break when subjected to external loading, and reform to a new configuration. The reformed bonds initiate a new generation. The generations are bonds that were formed at the same time and have the same reference deformation gradient. Different generations can have different stress and relative deformations, but the sum of the number fraction of the generations is conserved at unity [10]. That is,

$$\sum_{\alpha} w_{\gamma}^{\alpha} = 1. \quad (5.1)$$

Where, w_{γ}^{α} is the number fraction of the generation (α) from a bond type (γ), which is a positive scalar less than one. In this formulation, the number of generations is calculated based on the discretization of deformation into a finite number of time steps, which results in adequate numerical convergence.

By adding the response of generations, the overall response of a bond type is calculated, and by combining different bond types, an RIE material model is formulated. This constitutive setting allows for consistent modeling of the inelastic behaviors using the same set of equations Chapter 4. We used a simplified one-dimensional version of RIE to model the rat tail tendon’s axial tensile tests. We assumed that the stress in the material is the sum of all the bonds types ($T = \sum_{\gamma} T_{\gamma}$), and that the stress of a bond type is a weighted sum of the stresses from generations that depends on the overall stretch λ and the reference stretch of each generation $\lambda_{\gamma}^{\alpha}$, such that

$$T(\lambda, w_{\gamma}^{\alpha}, \lambda_{\gamma}^{\alpha}) = \sum_{\gamma} \sum_{\alpha} w_{\gamma}^{\alpha} \mathcal{T}_{\gamma}(\lambda/\lambda_{\gamma}^{\alpha}). \quad (5.2)$$

In this equation, \mathcal{T}_γ is the intrinsic hyperelasticity stress function that provides a unique stress for each deformation for each generation of a bond type. As a result, the state variables that control stress are λ , w_γ^α , and λ_γ^α Chapter 4.

We modeled the kinetics of molecular bonds to formulate the evolution of w_γ^α , and λ_γ^α for the different bond types Chapter 4. Three types of bonds are defined based on their kinetic rate: formative ($\gamma = f$), permanent ($\gamma = p$), and sliding ($\gamma = s$), which account for viscoelastic, hyperelastic, and plastic deformation behaviors, respectively Chapter 4. The formative bonds have a finite rate of breakage and reformation and the reference stretch is determined by the deformation at which the generation was initiated. That is, $\lambda_f^\alpha = \lambda(t^\alpha)$, and t^α is the time at which the generation was generated. This results in a viscoelastic behavior with a stress-free equilibrium condition (Fig. 5.1A,D) [10, 239]. Permanent bonds do not break ($w_p^0 = 1$ and $\lambda_p^0 = 1$), which results in a hyperelastic behavior with no deformation history dependence. The permanent bonds are a special case of formative bonds at the limit of slow kinetics. Sliding bonds are the other limit case; this time the kinetics rate is fast and the bonds almost instantaneously break and reform. In this case, the plastic deformation behavior can be formulated using constitutive relations for λ_s^α , where, for the 1D uniaxial tensile loading, $\lambda_s^\alpha \leq \lambda$ is the sufficient condition Chapter 4.

In this formulation, damage can be applied to all of the bond types by reducing the number fraction of the bonds able to carry load Chapter 4. As a result,

$$T(\lambda, w_\gamma^\alpha, \lambda_\gamma^\alpha, D_\gamma) = \sum_\gamma (1 - D_\gamma) \sum_\alpha w_\gamma^\alpha \mathcal{T}_\gamma(\lambda/\lambda_\gamma^\alpha). \quad (5.3)$$

In the above relation, D_γ is the damage parameter for each bond type that is a scalar in the range [0,1] and it is defined as

$$D_\gamma = 1 - \frac{\sum_\alpha \bar{w}_\gamma^\alpha}{\sum_\alpha w_\gamma^\alpha}. \quad (5.4)$$

Here, \bar{w}_γ^α is the number fraction of bonds with damage. According to Eq. (5.1) it reads

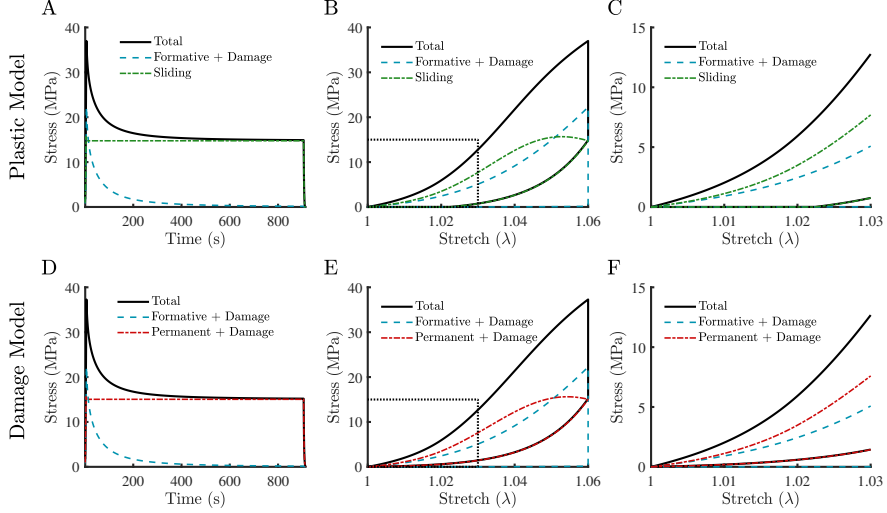


Figure 5.1. Schematic difference between the plastic deformation and damage models. In the plastic model (A-C) a combination of formative bonds with damage and sliding bonds is used. For the damage model (D-F) a combination of formative bonds with damage, and permanent bonds with damage is used. Both of the models have similar behaviors during loading, and relaxation ((A,D) and (B,E)); however, when looking closer at the boxed region in (B) and (E) during unloading (C and F) the plastic model shows a shift in reference unloaded configuration, where there is none for the damage model.

as

$$D_\gamma = 1 - \sum_{\alpha} \bar{w}_\gamma^\alpha. \quad (5.5)$$

Hence, if no bonds are damaged $D_\gamma = 0$, and if all of the bonds are damaged $D_\gamma = 1$ [151]. Both damage and the change of reference configuration in sliding bonds have a similar behavior during loading (Fig. 5.1B,E); however, during unloading the difference between these two processes becomes evident. Unlike plastic deformation, damage causes the softening effect without a shift in the reference unloaded configuration (Fig. 5.1C,F) Chapter 4. Note that for an example case with only permanent bonds ($\gamma = p$), because there is just one generation with non-zero number fraction (i.e., $w_p^\alpha = w_p^0 = 1$), Eq. (5.3) reduces to

$$T = (1 - D_p)\mathcal{T}_p(\lambda), \quad (5.6)$$

which is the common formulation used in classic continuum damage mechanics for

isotropic damage [28, 105, 123, 151].

5.2.2 Plastic deformation and damage constitutive relations

In this study, two separate models were created using the RIE framework: (1) plastic deformation model and (2) damage model. For the plastic deformation model we used a combination of formative bonds ($\gamma = fP$) and sliding bonds ($\gamma = sP$), where

$$T_{plastic} = T_{fP} + T_{sP}. \quad (5.7)$$

For the damage model, a combination of formative bonds ($\gamma = fD$) and permanent bonds ($\gamma = pD$) was used, where

$$T_{damage} = T_{fD} + T_{pD}. \quad (5.8)$$

The details of the constitutive relations and parameters are explained in the following and are summarized in Table 5.1.

5.2.2.1 Kinetics

For formative bonds, an nth-order kinetics rate equation was used:

$$\frac{dw_f^\alpha}{dt} = -K_f(w_f^\alpha)^{N_f}. \quad (5.9)$$

In this relation, the model parameters are (K_f, N_f) , where K_f is a positive number that scales the rate of the reaction and N_f is the order of the breakage reaction ($N_f \geq 1$). For the special case of $N_f = 1$, this relation reduces to a first-order kinetics equation, where its time constant is $\tau_f = 1/K_f$ [23]. For the sliding bonds, a step kinetics relation is used, where for breaking generations $w_s^\alpha = 0$, and for reforming generation $w_s^{\alpha+1} = 1$ Chapter 4. For the permanent bonds, since there is no bond breakage, $\tau_p = 1/K_p \rightarrow \infty$.

Table 5.1. Summary of the bond types, constitutive relations, and the model parameters used for each of the inelastic models.

	Bond Type	Kinetics	Int HElast.	Sliding	Damage	# par
Plastic	Formative	Nth-order $[K(s^{-1}), N]_{fP}$	Fiber-exp $[C_1(\text{MPa}), C_2]_{fP}$	-	Weibull $[k, l, r_0]_{fP}$	10
	Sliding	Step -	Fiber-exp. $[C_1(\text{MPa}), C_2]_{sP}$	Mod.Weibull $[b, c, r_0]_{sP}$	-	
Damage	Formative	Nth-order $[K(s^{-1}), N]_{fD}$	Fiber-exp $[C_1(\text{MPa}), C_2]_{fD}$	-	Weibull $[k, l, r_0]_{fD}$	10
	Permanent	- -	Fiber-exp $[C_1(\text{MPa}), C_2]_{pD}$	-	Weibull $[k, l, r_0]_{pD}$	

5.2.2.2 Intrinsic hyperelasticity

To account for nonlinear stiffening of tissue (toe-region), since the rat tail tendon fascicles have a mostly parallel makeup [166], a typical nonlinear fiber-exponential constitutive relation was used as the intrinsic hyperelastic function of the bonds [176, 240]:

$$\mathcal{T}_\gamma(\lambda/\lambda_\gamma^\alpha) = C_1[\exp(C_2(\lambda/\lambda_\gamma^\alpha - 1)) - 1]u(\lambda/\lambda_\gamma^\alpha - 1). \quad (5.10)$$

In this equation, C_1 and C_2 are positive-valued model parameters. In the plastic model, C_1 and C_2 are the same for formative and sliding bonds, and likewise for the damage model C_1 and C_2 are the same for formative and permanent bonds. This is a simplifying assumption that indicates the bonds from each model have the same load bearing capability, but their difference is due to the difference in their kinetics and inelastic parameters. In addition, $u(\cdot)$ is the Heaviside step function, which is included so that the constitutive relation does not provide for stiffness in compression.

5.2.2.3 Sliding

The axial stretch was used as the sliding variable ($\Xi_s = \lambda(t)$), which governs the sliding process in a non-reversible way Chapter 4. That is, sliding stretch increases upon loading, and its value does not change during unloading or lower loading. Hence, the difference between the reference stretch of two consecutive generations of the sliding

bonds ($\alpha - 1$ and α) is calculated as Chapter 4

$$\lambda_s^\alpha - \lambda_s^{\alpha-1} = f_s(\Xi_s(t^\alpha)) - f_s(\Xi_s(t^{\alpha-1})). \quad (5.11)$$

A modified Weibull's relation was used for f_s such that

$$f_s(\Xi_s) = (\Xi_s - 1) \left(1 - \exp \left[- \left(\frac{\Xi_s - (r_0)_s}{c - 1} \right)^b \right] \right). \quad (5.12)$$

The model parameters are b ($b \geq 1$) the shape parameter, c the scale parameter, and $(r_0)_s$ is the initial threshold of sliding ($c \geq 1, (r_0)_s \geq 1$). For a simple ramp loading with $(r_0)_s = 1$, one can show that $\lambda_s^\alpha = f_s(\Xi_s) + 1$. This constitutive relation guarantees that for a tensile loading, the reference configuration of bonds always is a non-compressive configuration (i.e., $1 \leq \lambda_s^\alpha < \lambda$). For convenience, the sliding stretch of the last generation λ_s^α will be simply referred to as the sliding stretch λ_s .

5.2.2.4 Damage

Similar to the sliding formulation, the axial stretch was used as the damage variable ($\Xi_D = \lambda(t)$) and the Weibull's cumulative distribution function (CDF) was used for accumulation of damage [75, 151]

$$f_D(\Xi_D) = 1 - \exp \left[- \left(\frac{\Xi_D - (r_0)_D}{l - 1} \right)^k \right]. \quad (5.13)$$

In this equation (k, l) are the Weibull's shape and scale parameters, respectively, and $(r_0)_D$ is stretch at the initial onset of damage ($k \geq 1, l \geq 1, (r_0)_D \geq 1$) Chapter 4. The accumulation of damage is calculated by considering the history of deformation and $\dot{D}_\gamma = (\partial f_D / \partial \Xi_D) \dot{\Xi}_D$ using a non-recoverable scheme that only allows for increase in damage during loading Chapter 4. Similar to λ_s^α it can be shown that if $(r_0)_D = 1$, for a simple ramp loading $D_\gamma = f_D(\Xi_D)$. Damage is applied to permanent bonds for the damage model. Additionally, the formative bonds in both models are allowed

to accumulate damage, because otherwise post-yield failure would not be possible. This is also consistent with the creep rupture of tendon under force-loading, because a viscoelastic response with no damage would converge to an “equilibrium” under that regime of loading, which further justifies our consideration for damage on formative bonds [5,233].

5.2.3 Experimental micro-tensile test data

Experimental data from Lee and co-workers [120] was used to fit the two models. Briefly, tendon fascicles were dissected from the tail of Sprague-Dawley rats and tested in a PBS bath. The mechanical tensile test consisted of ~ 5 mN preload, 5 cycles of preconditioning to 4% strain, a ramp load at 1%/sec to either 4% , 6%, or 8% grip-to-grip strains (n=7/group)(loading phase), held for 15 minutes (relaxation phase). Following relaxation, the specimen was unloaded at 1%/s (unloading phase), and reloaded to failure (reloading phase) (Fig. 5.2). The initial cross-sectional area and grip-to-grip length were used to calculate stress and strain. We used the maximum optical strain (reported as the tissue strain in [120]) to scale the grip-to-grip strain to account for the gripping effects and to avoid the errors in estimation of the applied strain to the tissue. The stress data was smoothed using the moving average method and re-sampled to one-thousand data points for each loading, relaxation, unloading, and reloading phases, and were then used for curve-fitting to calculate the model parameters.

5.2.4 Model implementation and parameter identification

The models were implemented using a custom written Matlab package for reactive inelasticity (ReactiveBond v1.1 [181]). For each phase of loading, relaxation, unloading, and reloading, one-thousand time-steps were used that results in the same number of generations for loading, unloading, and reloading. Note that no generations are initiated at the relaxation phase. These time steps were adequate for reaching

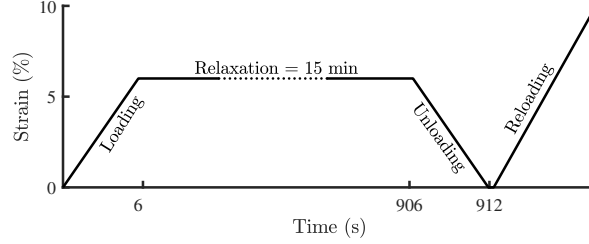


Figure 5.2. Micro-tensile mechanical testing profile. (A) The samples were ramped to a target grip strain (4%, 6%, or 8%) at a 1%/sec rate (loading phase), held for 15 min (relaxation phase), unloaded at 1%/sec (unloading phase), and reloaded to failure (reloading phase). The profile shown corresponds to a 6% target strain test.

numerical convergence. For parameter identification, we used a constrained multivariable nonlinear optimization method (*fmincon*, Matlab). The root-mean square error (RMSE) was used as the optimization cost function. To minimize the chance of convergence to local minima, we ran the optimization for each of the experimental stress curves using 48 randomly generated initial guesses and the solution with the minimum final residual value was selected as the optimal answer (*MultiStart*, Matlab).

5.2.5 Data analysis

The optimized curve-fit results were individually plotted for each phase of the test, and the resulting model parameters were illustrated using parallel coordinate plots (PCP) to visualize the fit parameters in a compact way [102]. In addition to the individual fit parameters, the means, medians, and the interquartile range (IQR) were calculated and displayed in the PCP. The resulting fit parameters' similarity to normal distributions were tested using a Jarque-Bera test (*jbttest*, Matlab) with a significance level set at ($p < 0.05$).

The goodness of the fits was assessed using the percent-error between the fits and the experiments, calculated as $\%err = 100(T_{fit} - T_{exp})/T_{exp,max}$. The IQR of $\%err$ is evaluated for both of the models, and plotted for each phase of the deformation as a function of the normalized time of the phase defined as $t = (t - t_1)/(t_2 - t_1)$, where t_1 and t_2 correspond to the time at the beginning and the end of the phase, respectively.

Normalization of time was performed to visualize the patterns of the errors due to variability in strains reached at each phase.

The constitutive relations used for formative bonds were the same between the models, so we hypothesized that the formative bond parameters are not sensitive to the choice of other bond types. To test this hypothesis, we compared the pairs of formative bond model parameters by using Wilcoxon signed rank test (*signrank* Matlab, $p < 0.05$).

5.2.6 Quantification of inelastic effects

The accumulation of inelastic effects are plotted for each bond type in each model. The inelastic effect of damage is represented by the damage parameter D_γ for formative bonds and permanent bonds. To calculate the inelastic effect of sliding on stress, analogous to the damage parameter, we defined a normalized representation of the sliding effect (when the sliding is occurring) as

$$\pi_{sP} = 1 - T_{sP}/T_{s0}, \quad (5.14)$$

where T_{s0} is the stress response of sliding bonds using the same intrinsic hyperelasticity relation with no sliding (equivalent to a permanent bond response). As a result, π_{sP} takes a value between zero and one, where $\pi_{sP} = 0$ indicates that there is no sliding in the system, and $\pi_{sP} = 1$ has a zero-stress response. To compare the inelastic effect between the models, the median stretches at the 50% inelastic effect ($D_{fP}, \pi_{sP}, D_{fD}, D_{pD} = 50\%$) were compared. Using paired comparison, median stretch of the formative bonds of two models were compared to each other, and the median stretches for sliding bonds were compared to permanent bonds (*signrank*, $p < 0.05$).

5.2.7 Model validation

To validate the models, we compared the response of both models to the constant strain-rate ramp experimental tests by Szczesny and co-workers [214]. This type of mechanical testing is widely used for material characterization, thus it is a suitable

choice for validation [122, 242]. It is important to note that the validation data was not included for the curve-fitting. We used the non-stained constant-rate ramp data from [214] ($n=4$, Figure 6 in [214]). The median values from the fit results of the models (Table 5.1) are used for predicting the mechanical response to a $1\%/sec$ deformation curve, up to the peak stress, and the time step between the initiation of the generations was set as 1.5 ms that results in adequate convergence. The modulus and the peak stress are compared between the experimental data and the model predictions.

5.3 Results

Both the plastic deformation and damage models resulted in excellent fits to the experimental data (Fig. 5.3). In particular, both of the models were capable of fitting the loading phase that showed stress stiffening (toe-region) followed by the linear-region (Fig. 5.3A,E). During the sustained loading of the relaxation phase, stress relaxation was closely fit as a result of using the n th-order kinetics relation for the formative bonds (Fig. 5.3B,F). The unloading phase had a different nonlinear response compared to the loading phase due to the inelastic behaviors (Fig. 5.3C,G). The reloading curves showed significant softening before reaching the peak stress that was captured by both models (Fig. 5.3D,H).

The errors were generally small between the model fits and the experiments, where the median of errors did not exceed 5% (Fig. 5.4). However, the performance of the models were not equal in all of the phases. In particular, both of the models overestimated the loading toe-region in the loading phase (Fig. 5.4A,E). The error during relaxation was maximum at the higher stress values—the start of relaxation—and it declined as the relaxation progressed (Fig. 5.4B,F). Both of the models had minimal overestimation during the unloading phase, where the plastic model had a slightly better performance towards the end of unloading (Fig. 5.4C,G). Upon reloading, the models underestimated the stress in the nonlinear stiffening region, and the error was lesser at the end of the reloading phase (Fig. 5.4D,H).

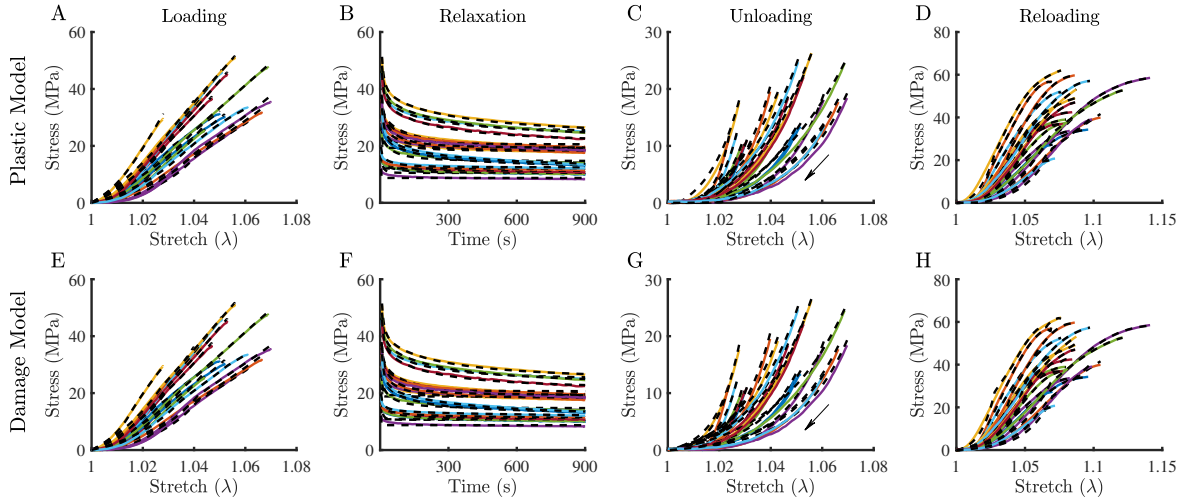


Figure 5.3. Fit results for individual experiments. The fits are overlaid (black dashed line) on top of individual experimental stress responses, for (A,E) loading, (B,F) relaxation, (C,G) unloading, and (D,H) reloading phases of the experiment. (A-D) are fits to the plastic model and (E-F) to the damage model.

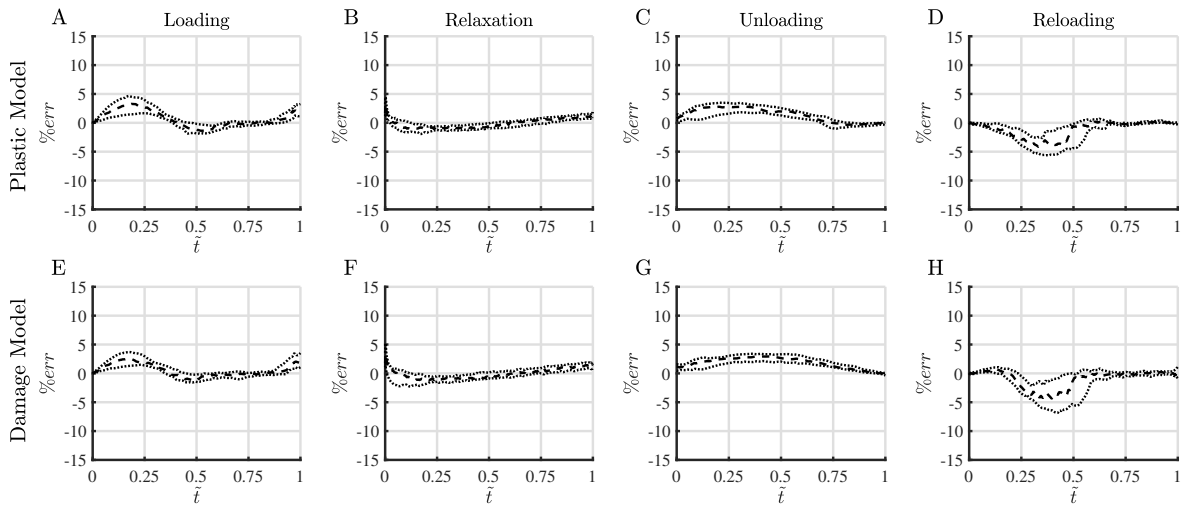


Figure 5.4. The IQR of $\%err$ of the model fits of (A,E) loading, (B,F) relaxation, (C,G) unloading, and (D,H) reloading phases as a function of the normalized time of each phase defined as $\tilde{t} = (t - t_1)/(t_2 - t_1)$, where t_1 is the beginning of the phases and t_2 corresponds to end of the phase. (A-D) are $\%err$ for the plastic model and (E-F) for the damage model (median = dashed line, $Q1, Q3$ = dotted lines).

The fit parameters were visualized using parallel coordinates plots (PCP), where each piece-wise line corresponds to the fit parameters of one sample (Fig. 5.5). Several model parameters had a different median and mean values, which is a sign for non-normality of the distributions; this was also confirmed by the normality tests that

indicates for an overall response the median is more appropriate compared to the mean value (Table E.1). Both of the models showed a similar trend in fit parameters for formative bonds, which were modeled using the same parameter sets, but independently fit using each model (Fig. 5.5). However, the statistical comparisons indicated that formative bonds' parameters had some differences. In particular, for kinetics of bonds K_f parameters were slightly different ($p < 0.05$), where for plastic model $K_f = 0.32s^{-1}$, and for the damage model $K_f = 0.34s^{-1}$, but there was no difference between the order of the kinetics relation ($N_f \sim 1.5$). Additionally, contrary to our hypothesis all of the pairs of intrinsic hyperelasticity (C_{1f}, C_{2f}) and damage ($k_f, l_f, (r_0)_f$) parameters were different, except for only l_f that did not show a difference ($p < 0.05$) (Table E.1). The sliding parameters of sliding bonds and the damage parameters of the permanent bonds were dissimilar, which was expected since they belong to different bond types (Figure 5.5 and Table E.1).

The inelastic effects on the bonds were calculated for each experiment and the stretch at which 50% inelastic effect for a bond type was reached (Fig. 5.6). In the plastic model, the formative bonds' damage reached $D_{fP} = 0.50$ at the stretch value of 1.07[1.04, 1.09] (read as *median*[$Q1, Q3$], Fig. 5.6A). The sliding bonds in the plastic model, π_{sP} reached 50% at the stretch of 1.05[1.04, 1.06] (Fig. 5.6B). For the damage model, the formative bonds reached $D_{fD} = 0.50$ at $\lambda = 1.06[1.05, 1.07]$, which had a slightly different distribution compared to that of formative bonds in the plastic model ($p < 0.05$) (Fig. 5.6C) and the permanent bonds $D_{pD} = 0.5$ was reached at $\lambda = 1.05[1.03, 1.05]$ which was similar to the sliding bonds (Fig. 5.6D). When looking at the individual samples, due to the non-recoverable nature of the inelastic effects during reloading, higher values were reached for all of the inelastic parameters compared to their counterpart in the loading phase (Fig. 5.6). In addition to the inelastic effects, for sliding bonds we plotted the reference stretch λ_s that reached the small value of 1.01[1.0, 1.02] during loading, and it increased to 1.05[1.04, 1.05] at the end of reloading phase (Fig. 5.6B).

To validate the model fits, the median parameter from both of models were used

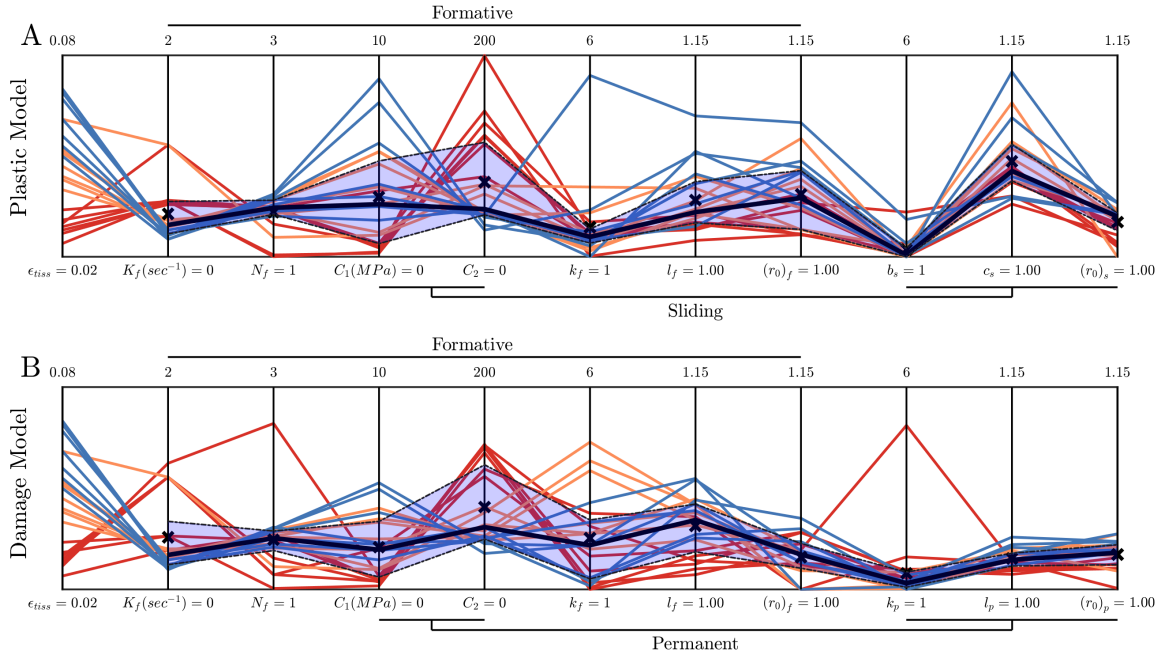


Figure 5.5. Parallel coordinates plots of the fit parameters for (A) plastic deformation model and (B) damage models, color-coded based on the nominal grip strain (red = 4%, orange = 6%, and blue = 8%). The interquartile range (IQR) is shaded, where the median value is plotted using a solid black line. The mean value is marked with “×”.

to predict independent experiments [214], where both models produced similar stress-strain curves that include the initial stiffening (toe-region) and subsequent increase in stress followed with softening (Fig. 5.7). Average experimental modulus and peak stress were 909 ± 27 MPa and 58 ± 4 MPa, respectively [214]. The predicted modulus of the plastic model was 832 MPa and the peak stress was 31 MPa. Respectively, these values were -8% and -46% different from the experiments. For the damage model, the modulus was 1036 MPa, and the peak stress was 64 MPa, which were 14% and 10% different from their experimental counterparts, respectively. In overall, both models produced similar stress-strain curve shapes, and modulus values; however, the damage model resulted in a closer peak stress prediction when compared to the plastic model (Fig. 5.7).

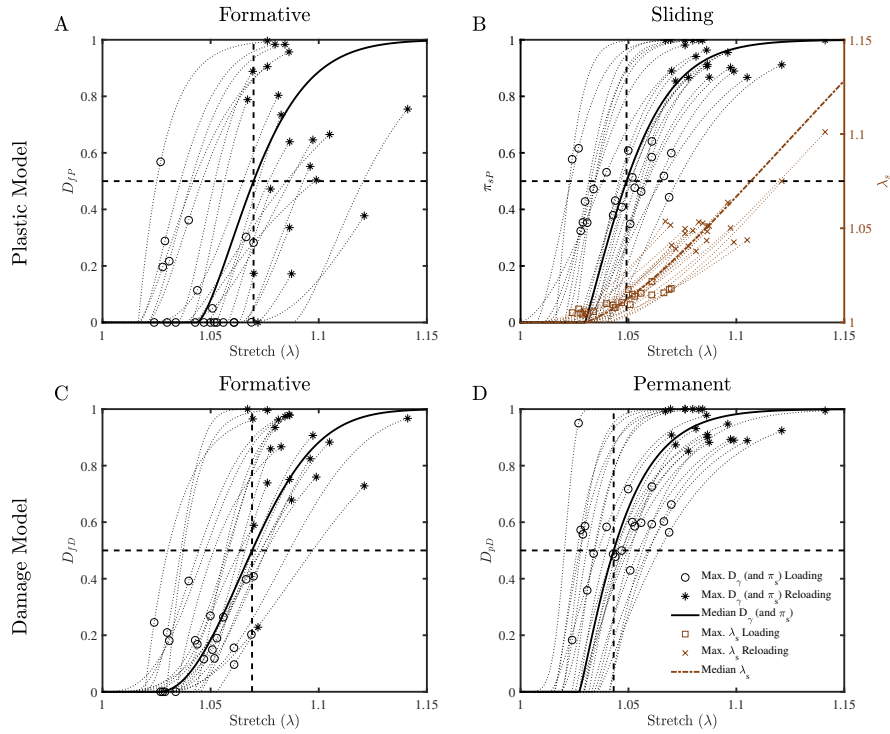


Figure 5.6. Accumulation of damage and plastic deformation. The overall response for accumulation of damage (D_{γ}), and normalized plastic deformation (π_s) are plotted for each bond type using the median of the fit parameters (solid line). The 50% inelastic effect lines are marked using horizontal straight lines and the median stretch of all samples' intersected with this 50% inelastic effect line is marked with a vertical line. Additionally, the maximum damage and normalized plastic deformation reached during individual fits in loading (open circle), and reloading (star) phases for the individual fits. For the sliding bonds, the sliding stretch (λ_s) is also plotted (brown dashed line) and the maximum plastic deformation stretch during loading (open square) and reloading (cross) phases is plotted with respect to the right y-axis (brown).

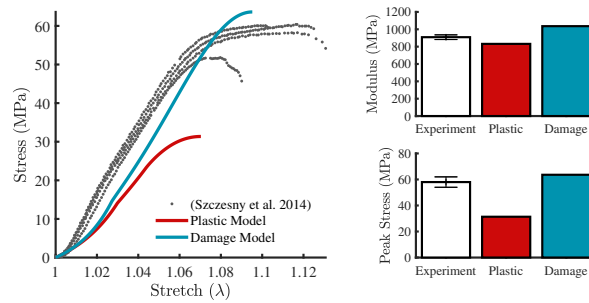


Figure 5.7. Validation plots for prediction of plastic and damage models, showing the comparison of the experimental data from [214] to the predictions of the plastic model (red) and damage model (blue) to a ramp loading.

5.4 Discussion

5.4.1 Comparison between the plastic deformation and damage models

In this study we successfully applied the theoretical framework of reactive inelasticity to tendon experimental data [120]. We implemented two independent models, specific to plastic deformation or damage, and showed excellent fits to the experiments (Fig. 5.3), and visualized the outcome parameters using parallel coordinate plots, which enhances visualization of the complex relationships among them. The fits showed that the plastic model had slightly smaller errors towards the end of the unloading phase, which was due to inclusion of plastic deformation that agrees with previous studies [1,210]. However, when comparing the model predictions using the resultant fit parameters to independent validation experimental data, both of the models predict similar stress-strain curves, with the damage model having more similar behavior (Fig. 5.7). These results do not strongly favor one approach over the other, and both of the inelastic mechanisms may contribute to the mechanical response, thus further investigations and different experimental testing protocols are needed to differentiate between tendon plastic deformation and damage behaviors. Particularly, force-controlled tests that can enable unloading to zero-force rather than zero-deformation can be helpful to distinguish plastic deformation and damage.

5.4.2 Interpretation of inelastic effects

The J-shaped form for the accumulation of inelastic behaviors in our study (Fig. 5.6) are consistent with the findings of a recent study that reported the increase in denatured collagen during tensile loading by using collagen hybridizing peptides (CHP) [249]. This indicates that the accumulation of inelastic effects may be correlated with collagen denaturation due to mechanical loading. However, the CHP study suggested onset of damage at higher strains ($\sim 8\%$ strain) [249] compared to our study ($(r_0)_\gamma < 5\%$) and other studies [1, 120, 210]. This suggests that in addition to collagen denaturation, other molecular mechanisms and proteins in extra-cellular matrix (perhaps elastin or decorin) may play a role in the inelastic mechanical response of

tendon [58, 85, 172]. Further, part of the inelastic response also can arise from multi-scale “sliding” between tendon’s fibrous components [77, 214] that is not intended to be represented by the sliding bonds, which specifically address the macro-scale response in a continuum mechanics scheme. While identification of the relationships between tendon’s inelastic mechanics and molecular disruptions require further investigations, the inelastic effects can be quantified by using mechanical modeling for understanding the mechanical properties of tendon, and assessing its altered mechanical properties in various stages of disease, injury, and healing [5, 68, 203].

5.4.3 Remarks about RIE modeling

We hypothesized that the formative bond parameters would be the same for both models regardless of the choice of sliding or permanent bonds for the equilibrium response. While they were similar, there were some unexpected and statistically significant differences (Table E.1). This may be due to the simplifying assumption we made that the formative bonds had the same intrinsic hyperelasticity parameters as the sliding or permanent bonds (Table 5.1). We made this assumption in order to use the minimum number of variables to model the tendon response. It is unclear if full independence of bond parameters would provide a benefit over the current modeling framework. Nonetheless, it is likely that including interaction terms between bonds or addition of more bonds and parameters, as a spectrum [15, 167], could be beneficial for accurate modeling of tissue’s inelastic behaviors.

5.4.4 Sources of error

The percent-error ($\%err$) of the models were quite small, but both of the models had relatively large errors in the toe-regions and the beginning of the relaxation phase (Fig. 5.4). Here, our continuum modeling scheme is intended to study the macro-scale inelastic behaviors, and it does not account for the microstructure. Smoother fits could be achieved with more elaborate constitutive relations and microstructural considerations, such as fiber-recruitment for intrinsic hyperelasticity [17, 180, 215] or

normalized energy and stress for sliding and damage [151, 202, 231], and by adding derivatives of the stress response to the cost-function. For the relaxation phase, despite some deviations at the beginning, this phase was well fit by using a generalized n -order kinetics for formative bonds (Fig. 5.4B,F). The error in the relaxation phase may be related to fluid flow dependent viscoelasticity [36, 176], which was not included in this study. We expect this to be a small effect for tail tendon; however, it can be added by using a biphasic mixture with RIE as the solid phase [93, 245]. The poroelastic parameters are the subject of the next chapter, where we use osmotic loading, and finite element modeling to evaluate the hydraulic permeability and other poroelastic parameters of tendon. A further limitation is that we assumed the kinetics rate of bond breakage and reformation is not dependent on the level of strain; however, adding strain-dependence to kinetics parameters might be necessary for modeling more complicated loading scenarios such as incremental stress-relaxation [10, 99].

5.4.5 Conclusion and future direction

In conclusion, we applied the theoretical framework of reactive inelasticity (RIE) to model viscoelasticity, plastic deformation, and damage to determine tendon’s inelastic mechanical response. This study is novel in that (1) it investigated tendon inelastic effects without a prior assumption about the softening mechanism and compared the two modeling approaches for inelasticity, (2) it demonstrated numerical values for inelasticity effects on tendon mechanical response, and (3) it provides a path forward to relate the molecular structure of tendon to its mechanical response. We applied the models to the experimental data, and validated the model by comparing the predictions to an independent set of experimental data. Both models were successful in fitting and predicting the experimental data, although the plastic model had slightly better fits during the unloading phase, and the damage model had better predictions of the independent validation data set. However, the results largely indicate that deformation-driven experiments can be equally described with both plastic deformation and damage perspectives. Thus, distinguishing plastic deformation and damage

mechanisms will require further experimental studies using different loading protocols.

Chapter 6

EVALUATION OF TENDON HYDRAULIC PERMEABILITY USING OSMOTIC LOADING AND BIPHASIC FINITE ELEMENT MODELING

6.1 Introduction

Tendon's viscoelastic behaviors and mechanisms are important to mechanical function and mechanobiology [119, 203]. Fluid flow, as an example, is a mechanism of viscoelasticity that is likely to have an important role in maintaining healthy and injured tendons homeostatic balance by transporting nutrition from synovial fluid to tenocytes [59, 72]. In general, tendon viscoelasticity can be attributed to both intrinsic mechanisms in the solid matrix and to fluid-flow-dependent poroelastic mechanisms. Solid matrix viscoelasticity for tensile loading along the tendon longitudinal axis (fiber direction), is typically analyzed using phenomenological models, such as quasi-linear viscoelasticity (QLV) [69, 167, 188, 240] and recently using structurally-inspired reactive mixture models [182, 185]. Fluid-flow-dependent viscoelasticity for tensile loading in the fiber direction has been analyzed using poroelasticity for tendon and other fibrous tissues [93, 124, 211, 245], although success in multiple loading modalities has been limited. The effect of these mechanisms are overlapping and difficult to distinguish, moreover tendon is highly anisotropic and these fiber-aligned studies do not provide tendon transverse viscoelastic properties .

When loaded in longitudinal tension, tendon has a large Poisson's ratio ($\nu > 2$) that exceeds the limit of incompressibility for isotropic material ($\nu = 0.5$) [131, 176], which indicates that tendon is anisotropic and it experiences volume-loss, inducing fluid exudation. Recent high-frequency AFM Nano-indentation of tendon reveals that there

are two distinct peaks in the phase shift of tendon’s response indicating a geometry-independent and a geometry-dependent behavior, which may correspond to solid matrix and poroelastic viscoelasticity, respectively [36,152]. Therefore, transverse poroelasticity is an important contributor to tendon material behavior.

Despite decades of studies on the mechanical response of tendon, transverse mechanical properties are not well understood. Only a few studies on tendon (and ligament) in compression report transverse elastic and poroelastic properties [21, 84, 157,187,236]. In particular, the transverse modulus and hydraulic permeability that are required to evaluate the fluid flow contribution to viscoelasticity are mostly unavailable for tendons. As an example, for transverse hydraulic permeability although some studies report tendon permeability by modeling tendon as a biphasic mixture, the values in these studies vary by several orders of magnitude 10^{-6} to $10^{-1}\text{mm}^4(\text{Ns})^{-1}$ [152,245]. This is likely due to the complexity of the interacting inelastic mechanical behaviors and the need for a careful treatment of the experimental procedure to isolate the poroelastic behavior.

Hence, the objective of this study was to quantify the transverse poroelastic material parameters of tendon through transverse osmotic loading experiments and mixture finite element modeling. We osmotically loaded tail tendons in the transverse direction, both in compression and tension, which isolated the fluid-flow mechanisms. The induced transverse strain over time was measured and was fitted to a finite element model by using a novel multi-start optimization method. This is a robust method to explore the search space to identify the model parameters. We report tendons transverse solid matrix elastic parameters, and transverse permeability in both transverse tension and compression. Further, using these results, we predict hydraulic permeability of tendon during uniaxial loading and the spatial distribution of fluid flow during transverse osmotic loading.

6.2 Material and Methods

6.2.1 Sample preparation and grouping

Tail tendon fascicles were harvested from mature Long-Evans female rats (aged 4 to 8 month). A 60 mm long portion of the proximal tail was dissected by means of a surgical scalpel, and individual fascicles were pulled from the distal end of the cut portion [183,216]. The fascicle was immediately cut transversely to obtain matched pairs with the same length (30 mm). The proximal and distal halves were randomly assigned to *osmotic loading* or fresh-frozen *water content* groups. For osmotic loading we used SPEG (polyethylene glycol PEG 20 kDa and 0.9% tris-buffered saline) at concentrations of $c = 1\%$, 8% (as the reference control), and 15% SPEG ($n = 5$ per group). SPEG is a polymeric based solution that maintains hydration and mechanics of rat tail tendon fascicles close to physiological level at 8% concentration [183].

6.2.2 Loading protocol

For the osmotic loading groups, each sample was first gripped in a custom-made microtensile testing machine (Fig. 6.1A), with approximately 10 mm grip-to-grip clearance [120,214] while bathed in 8% SPEG. The sample, was preloaded to maximum of ~ 0.01 N to remove slack, and immediately preconditioned between 0% and 2% strain for 5 cycles at $1\%.s^{-1}$ rate.

Following preconditioning, the sample was held at the zero-deformation for 16 min (Equilibration phase, Fig. 6.1A). After this phase, the buffer bath was removed by means of an electric pipette and the solution was changed either to 1% , 8% or 15% SPEG, and the sample was held in position for 16 min (Osmotic loading phase, Fig. 6.1A). The transverse image of the fascicle was recorded during the test using a CCD camera (Fig. 6.1B). Additionally, the axial force was monitored throughout the test. Note that the axial force remained at the preload-level during both Equilibration and Osmotic loading phases (Fig. 6.2).

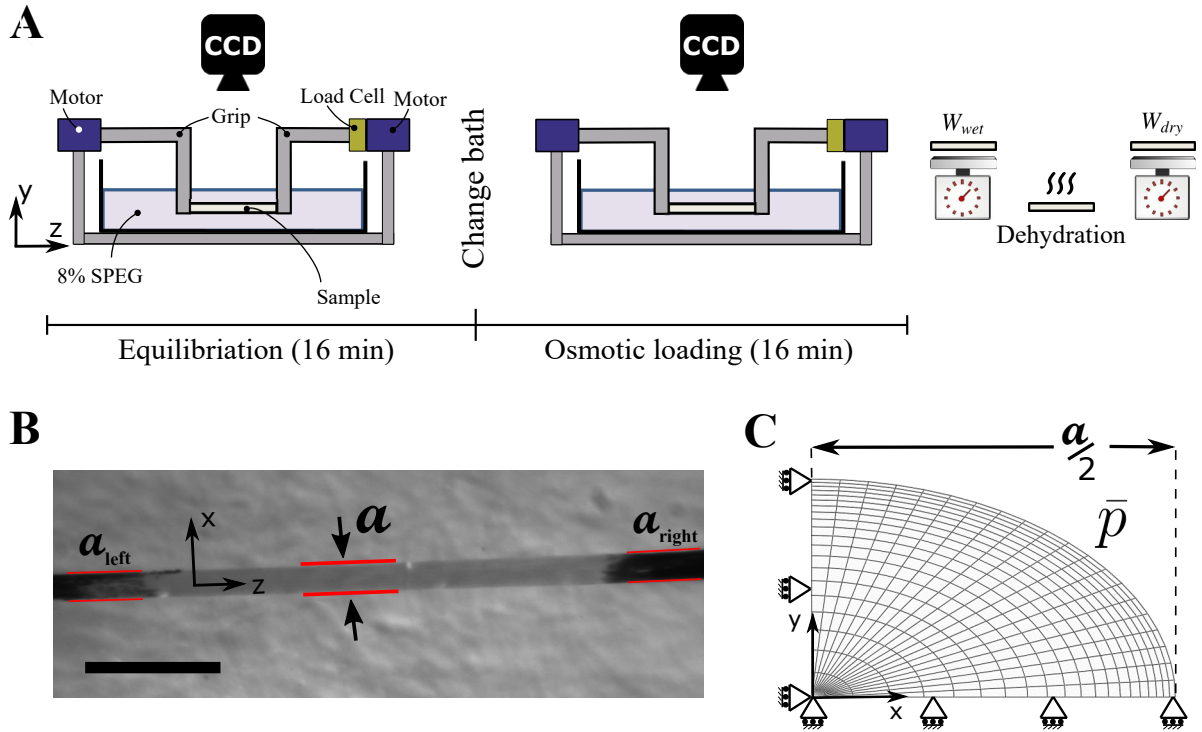


Figure 6.1. Methods for osmotic loading experiments and finite element modeling: (A) The samples were equilibrated in 8% SPEG for 16 minutes, followed by the osmotic loading by exchanging the buffer solution with 1%, 8% (control), or 15% SPEG. After osmotic loading the samples were weighed to get wet mass (W_{wet}), dehydrated and weighed again to get the dry mass (W_{dry}). (B) The transverse width ($a = (a_{left} + a_{right})/2$) was measured over time in solution (scale = 1 mm). (C) Finite element analysis included a quarter ellipse with a pressure boundary condition.

6.2.3 Water content measurements

The water content of osmotically loaded samples and their matched fresh-frozen halves from the same fascicle were measured to determine the effect of osmotic solution on the water content. Each sample was first placed in a capped micro-tube on an electronic scale (0.1 mg precision) to measure the wet weight, transferred to the oven for dehydration (at least for 20 hr in 43°C), and the dry weight was measured (Fig. 6.1A). For the osmotic groups, after the loading phase, while the sample was gripped, a scalpel blade was used to cut the samples at the gripped ends and the remaining sample was used for the water content measurement. The fresh-frozen sample's wet weight was measured immediately after dissection. The water content (φ_w) was calculated as [183]:

$$\varphi_w = \frac{W_{wet} - W_{dry}}{W_{wet}}. \quad (6.1)$$

Where, W_{wet} is the wet weight and W_{dry} is the weight after dehydration (Fig. 6.1A). We calculated the change to φ_w ($\Delta\varphi_w$) by subtracting the water content of osmotic group from their paired fresh-frozen sample.

6.2.4 transverse strain and image analysis

The transverse width of the sample a was calculated by averaging sample's width at two locations, as $a = (a_{left} + a_{right})/2$ (Fig. 6.1B). The marked widths were measured using a custom written segmentation code. One sample from the 15% SPEG group was excluded due to what appeared to be accidental movement of the CCD camera during imaging. The transverse strain along x-axis (ϵ_t) was calculated as

$$\epsilon_t = \frac{a}{a_0} - 1 \quad (6.2)$$

Where, a_0 is the average width of the sample during the Equilibration phase (see supplementary Fig. F.1). Additionally, we calculated the volumetric strain based on the equilibrium transverse strain, calculated by averaging the last five minutes of the transverse strain during the Osmotic loading phase (see Results Fig. 6.4B) and the assumption of transverse isotropy of tendon as

$$\epsilon_{vol} = 2\epsilon_t \quad (6.3)$$

6.2.5 Statistical analysis of water content and comparison to volumetric strain

To check if the samples in the three groups had the same initial condition, we conducted an ANOVA between the fresh-frozen group's water content ($p < 0.05$). To test if the osmotic loading had an effect on the water content we performed a separate ANOVA between the water content of the samples after osmotic loading ($p < 0.05$).

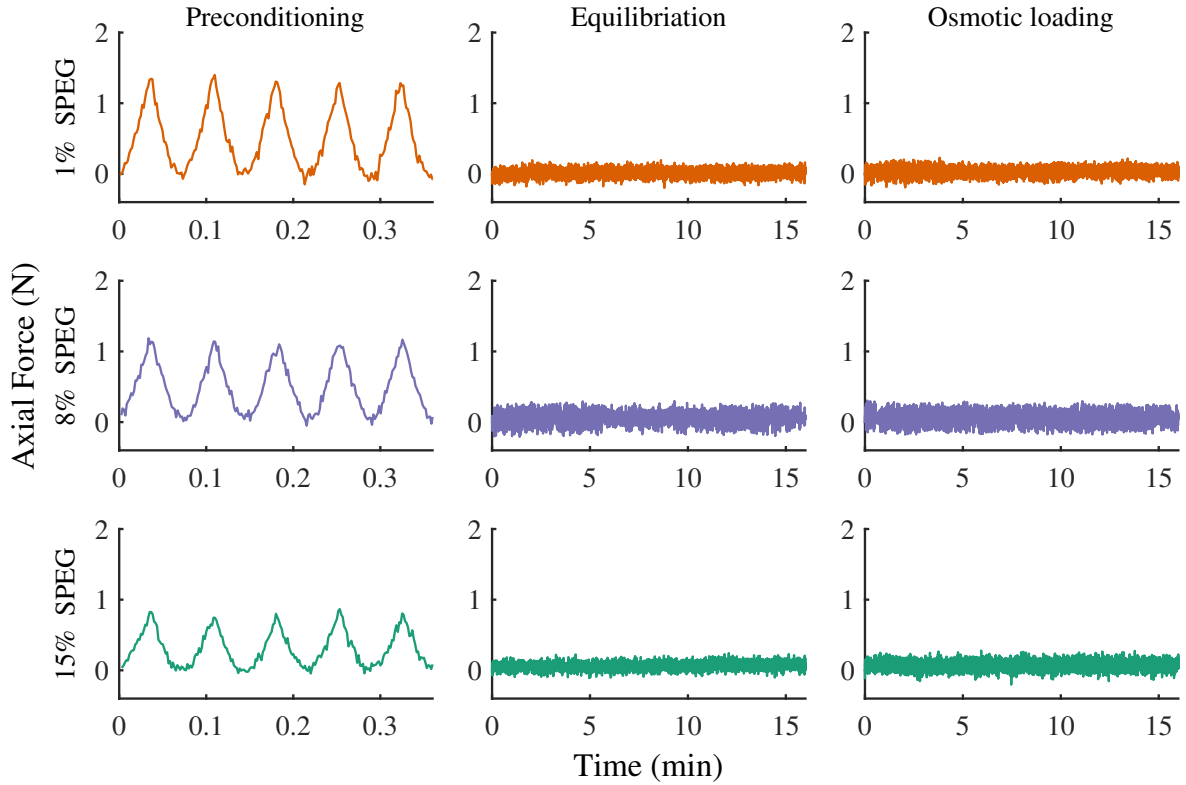


Figure 6.2. Representative axial force during the three phases of the protocol for each of the SPEG solutions. There was no change to axial force during Equilibration or Osmotic loading phases.

As a post-hoc test, we compared the pairs of fresh-frozen and osmotic loading water contents using paired two-tailed t-test ($p < 0.05$). To test if the change to water content and the change to volume are the same, we conducted single-group t-tests on ϵ_{vol} ($p < 0.05$), and performed paired t-tests between ϵ_{vol} and ϵ_{vol} for each group ($p < 0.05$).

6.2.6 Biphasic finite element model

To evaluate the biphasic properties of tendon we developed a finite element (FE) model using FEBio (v2.8 febio.org [132]) and applied it to the Osmotic loading phase. According to the high aspect-ratio of fascicle the plane-strain condition was imposed. A symmetric elliptical quarter-cylinder was meshed using hexahedral elements (Fig. 6.1C), where the ellipse parameters were: semi-major axis $a/2 = 0.14$

mm based on the average of the current study's samples ($a = 0.28 \pm 0.05$ mm), and eccentricity $e = 0.8$ based on previous measurements of rat tail tendon fascicle ($e = 0.79 \pm 0.14$ [183]).

To model osmotic loading, we imposed a pressure boundary condition (Fig. 6.1C). Since during Equilibration phase, the tendon was bathed in 8% SPEG, the effective boundary pressure (\bar{p}) was calculated relative to 8% SPEG using the phenomenological virial expansion of the osmotic pressure [29]

$$\bar{p}_{1,15\%} = b_1(c_{1,15\%} - c_{8\%}) + b_2(c_{1,15\%}^2 - c_{8\%}^2), \quad (6.4)$$

where $b_1 = 1.283 \times 10^{-4}$ MPa and $b_2 = 8.532 \times 10^{-6}$ MPa, which results in -63 kPa for 1% SPEG (tension osmotic loading) and 146 kPa for 15% SPEG (compression osmotic loading).

The solid matrix was modeled using a Holmes-Mow material constitutive relation (modulus E , Poisson's ratio ν , nonlinearity factor β) [88] as

$$\Psi(I_1, I_2, J) = C_0 (\exp[Q(I_1, I_2, J)] - 1), \quad \text{where} \quad (6.5)$$

$$C_0 = \frac{\lambda + 2\mu}{4\beta}, \quad \text{and} \quad Q = \beta \frac{2\mu - \lambda}{\lambda + 2\mu} (I_1 - 3) + \beta \frac{\lambda}{\lambda + 2\mu} (I_2 - 3) + \ln J^2. \quad (6.6)$$

Here, Ψ is the energy density function, I_1, I_2 are the first and second invariants of the right Cauchy strain tensor, J is the Jacobian of the deformation, and λ and μ are the Lamé parameters. Permeability was modeled with deformation dependency as [88]:

$$k(J) = k_0 \left(\frac{J - \varphi_{s0}}{1 - \varphi_{s0}} \right)^\alpha \exp \left[\frac{1}{2} M (J^2 - 1) \right]. \quad (6.7)$$

Where, φ_{s0} is the reference solid volume fraction ($\varphi_{s0} = 1 - \varphi_{w0}$; set to $\varphi_{s0} = 0.6$); k_0 is the reference permeability with the dimensions of $\text{mm}^4(\text{Ns})^{-1}$; α and M are non-dimensional positive parameters controlling the deformation dependence of k . In summary, the fitted model parameters were: $E, \nu, \beta, k_0, \alpha$, and M . We will refer to

E , ν , and β as *solid matrix parameters* and to k_0 , α , and M as *permeability parameters*.

6.2.7 Model parameter identification

To identify the model parameters, we used a constrained multivariable nonlinear optimization method (*fmincon*, Matlab). To minimize the chance of converging to a local minima, we used multiple initial conditions from a wide range search space, where the initial Holmes-Mow model parameters were sampled from $0 \leq E \leq 1$ MPa, $0 \leq \nu < 0.5$, $0 \leq \beta \leq 5$, and the hydraulic permeability parameters were chosen between $10^{-5} \leq k_0 \leq 10^{-2} \text{ mm}^4(\text{Ns})^{-1}$, $0 \leq \alpha \leq 5$ and $0 \leq M \leq 5$. For the initial conditions, the search space was sampled by two-hundred values per variable using a Latin Hypercube method (*lhsdesign*, Matlab), and we ran the optimizations for each of the tension and compression osmotic loading cases, separately. As cost function (*res*), we used the root-mean square error (RMSE) of the transverse strain (along x-axis Fig. 6.1), which was calculated using the transverse strain of the FE model and the mean transverse strain of the experiments. Only fits that met the criterion of RMSE of less than 50% of the standard deviation of experimental transverse strain were accepted.

To visualize the initial parameters used for curve-fitting and the accepted fits we used parallel coordinate plotting, which is a compact way to illustrate a high-dimensional data [102,182]. Further, for identifying an overall response, we used the median of the accepted parameters from the optimizations that met the curve-fitting criterion.

6.2.8 Statistical analysis of fitted mechanical parameters

For inspecting the solution space all the permutations of the pairs of fit parameters were plotted and a linear correlation analysis was performed ($p < 0.05$). Particularly, we observed that E and ν were not independent, hence, we calculated bulk

modulus K for matched pairs of fitted E and ν , separately for tension and compression osmotic loading as

$$K = \frac{E}{3(1 - 2\nu)}. \quad (6.8)$$

We compared K from tensile and compression osmotic loading tests using a unpaired two-tailed t-test ($p < 0.05$). Similarly, to test if the parameters from compression and tension osmotic loading groups were different, for each of the fit parameters the probability distribution was calculated and a two-sided Wilcoxon rank sum test was performed between them ($p < 0.05$).

6.2.9 Prediction of hydraulic permeability during axial loading

It was of further interest to predict the tendon hydraulic permeability during uniaxial tensile loading. Due to tendon's high Poisson's ratio in axial loading (ν_{zx} and ν_{zy}) [131, 176], a negative volumetric strain is expected during axial loading ($J < 1$). To predict the hydraulic permeability of tendon during axial loading, we used the range of deformation of $0.8 \leq J \leq 1$ that represents a deformation with volume loss. By assuming $\nu_{zx} = \nu_{zy} = 2$ this range of J corresponds to approximately $0 \leq \epsilon_z \leq 6.7\%$, which is calculated using the following relation for infinitesimal deformation $\epsilon_z = \epsilon_{vol}/(1 - 2\nu_{zx})$. For rat tail tendon, $\epsilon_z = 6.7\%$ is a mid-to-high range axial deformation [120]. The curves were generated using the median parameters of the fit parameters from tension and compression osmotic loading groups, separately.

6.2.10 Distribution of fluid flow and deformation

We used the median response to calculate fluid flux along the boundary of tendon over the course of osmotic loading. Fluid flux is calculate according to Darcy's law

$$\mathbf{w} = k \cdot \nabla p. \quad (6.9)$$

Where, \mathbf{w} is the fluid flux relative to solid matrix, k is the hydraulic permeability, and ∇p is the interstitial fluid pressure gradient [14]. The fluid flux was visualized for each

element on the curved outer boundary of the finite element mesh.

6.3 Results

6.3.1 Effect of osmotic loading on water content and tissue strain

The 1% SPEG put the tissue under transverse tensile loading and 15% caused a transverse compressive loading. All of our samples had the same initial water content, as shown by analysis of variance on fresh-frozen water content across different groups (Fig. 6.3A). Further, analysis of variance indicated that the osmotic loading affected the water content ($p < 0.05$) (Fig. 6.3A,B). When comparing the fresh-frozen groups to their paired osmotic loading groups, we see that the 8% SPEG control did not alter the water content, where the 1% SPEG (tension osmotic loading) showed a trending increase φ_w by $9.9\% \pm 8.6\%$ ($p = 0.062$) (Fig. 6.3A,B). Surprisingly, for the 15% SPEG (compression osmotic loading) $\Delta\varphi_w$ was not different between the fresh-frozen and its osmotic loading paired group ($\Delta\varphi_w = -4.9\% \pm 6.3\%$, $p = 0.156$) (Fig. 6.3A,B).

To check if osmotic loading alters the water content at a similar amount compared to volumetric strain, we first conducted single-group t-test ε_{vol} , and compared the changes to the water content to the paired volumetric strain. As expected, the volume did not change for 8% SPEG control group ($\varepsilon_{vol} = 2.0\% \pm 3.1\%$, $p = 0.215$) (Fig. 6.3B). For the 1% SPEG and 15% SPEG ε_{vol} was non-zero ($p < 0.05$), where for 1% SPEG $\varepsilon_{vol} = 13.1\% \pm 5.1\%$, and for 15% SPEG $\varepsilon_{vol} = -7.1\% \pm 1.0\%$ (Fig. 6.3B). The change to water content and volumetric strain were not statistically different between the two measurements ($p > 0.05$) (Fig. 6.3B).

6.3.2 Optimization results and fit parameters

The overall response for 1% and 15% SPEG solutions were calculated by using the median of the fitted parameters, where for both of the solutions these model resulted in extremely good fits (Fig. 6.4). The resulting fit parameters were visualized using a parallel coordinate plot (PCP) (Fig. 6.5) and the summary of the fit parameters is provided shown in Table 6.1.

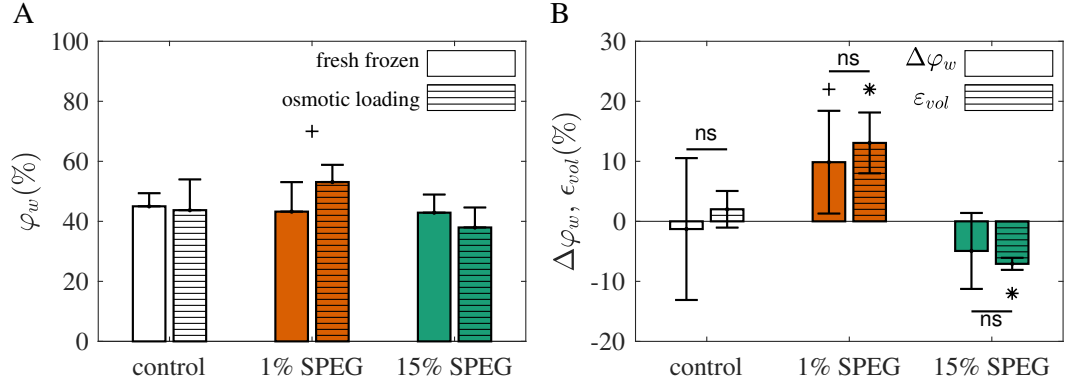


Figure 6.3. Change to water content and volumetric strain due to osmotic loading (A) Water content φ_w of control (8%), 1% and 15% SPEG groups, for fresh-frozen and osmotic loading groups. The control was not different than its fresh-frozen pair, confirming that 8% SPEG maintains tissue’s fresh-frozen hydration. When comparing the osmotic group to the matched fresh-frozen samples, the 1% SPEG group’s water content showed a trending increase ($\Delta\varphi_w = 9.9 \pm 8.6$, $p = 0.062$), and the 15% SPEG did not show a difference (B) The change to water content $\Delta\varphi_w$ and volumetric strain ϵ_{vol} of control (8%), 1% and 15% SPEG groups. For ϵ_{vol} , the control volumetric strain was $2.0\% \pm 3.1\%$ and not different from zero, for both of 1% SPEG and 15% SPEG ϵ_{vol} was non-zero ($p < 0.05$). For 1% SPEG $\epsilon_{vol} = 13.1\% \pm 5.1\%$, and for 15% SPEG $\epsilon_{vol} = -7.1\% \pm 1.0\%$. Comparison between $\Delta\varphi_w$ and ϵ_{vol} did not result in statistical significance for either of the solutions. Error lines are mean \pm standard deviation. + $p = 0.062$, * $p < 0.05$

Out of 200 initial points for the optimization, 163 of tension group fits and 36 of the compression group fits met the optimization criterion (defined in Section 6.2.7) (Fig. 6.5). It is evident that after optimization, the initial residual values (res) are reduced, and “trends” in the solution parameters are evident. Particularly, we observe that the Young’s modulus (E) and Poisson’s (ν) appear to have lower values for the tension osmotic loading, where the other parameters were visually not different between the osmotic loading groups. This indicated a tension-compression nonlinearity, which motivated further investigation to formally compare the fit parameters (described in the following).

To check for tension-compression nonlinearity, we compared the accepted fit parameters from the tension and compression osmotic loading group fits (the diagonal elements of the Fig. 6.6, and summarized in Table 6.1). Notably, for the tensile loading group the modulus had a median of 0.570 MPa, and for the compression group, the

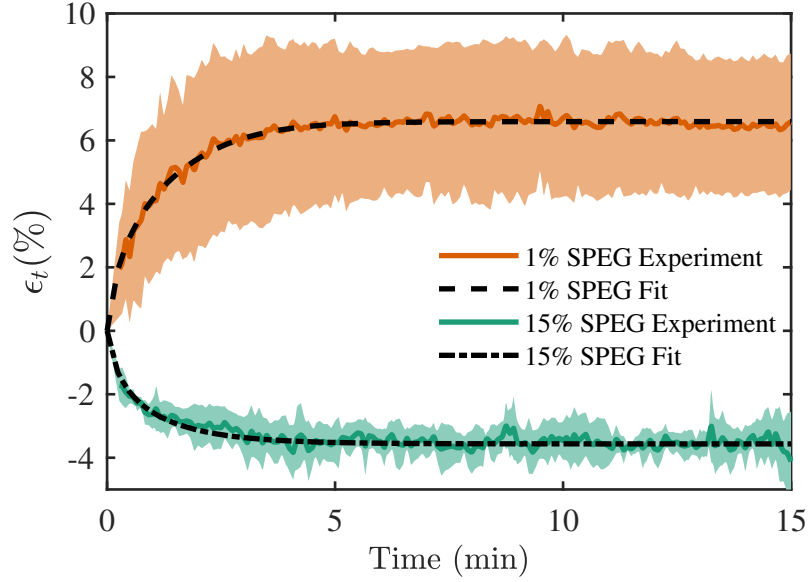


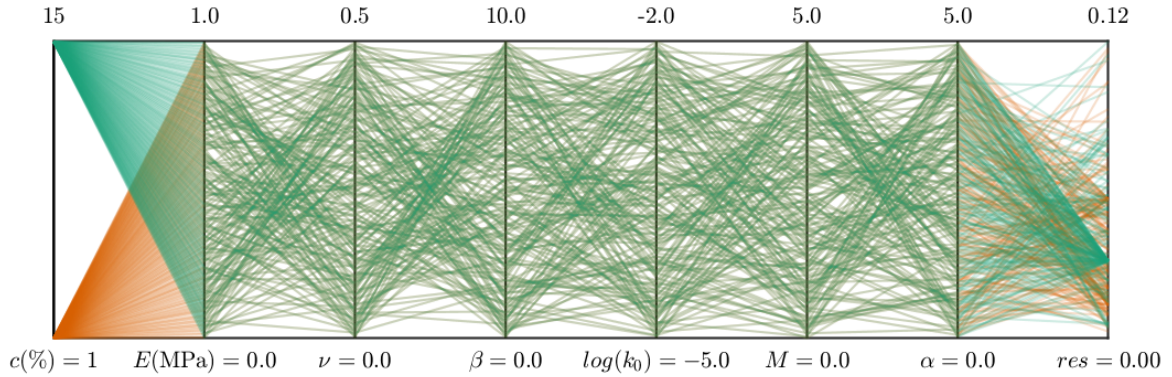
Figure 6.4. Experimental transverse strain and the model fits for 1% SPEG (tension osmotic loading; top orange), and 15% SPEG (compression osmotic loading; bottom green). For each case the resulting overall fit (using median parameters) is overlaid (dashed lines) on top of the mean experimental response. The shaded areas indicate mean \pm standard deviation of the experimental transverse strain.

median was 0.740 MPa, which was larger in compression compared to tension ($p < 0.05$). Similarly, the median Poisson’s ratio for the tensile loading was 0.247, which was lower than that of the compression loading group’s median 0.433 ($p < 0.05$). The reference hydraulic permeability (k_0) for 1% SPEG was $2.057 \times 10^{-5} \text{ mm}^4(\text{N s})^{-1}$, and it was $2.013 \times 10^{-5} \text{ mm}^4(\text{N s})^{-1}$ for 15% SPEG (Table 6.1). These values were not different between the groups. The rest of the parameters were similar, except for small differences in M and α (Fig. 6.6 diagonal and Table 6.1).

A careful inspection of these parameters indicated that correlations exist between some parameters (Fig. 6.6). In particular, there was a correlation between modulus and Poisson’s ratio for both of the osmotic loading groups (Fig. 6.6). Further, for the tension osmotic loading (1% SPEG), M and α were correlated, and for the compression osmotic loading (15% SPEG) E was correlated with β , k_0 , and M ; ν was correlated with β ; k_0 had correlation with parameters M and α (Fig. 6.6).

One important observation was that the Young’s modulus, and Poisson’s ratio

A. Initial Conditions



B. Fit Results

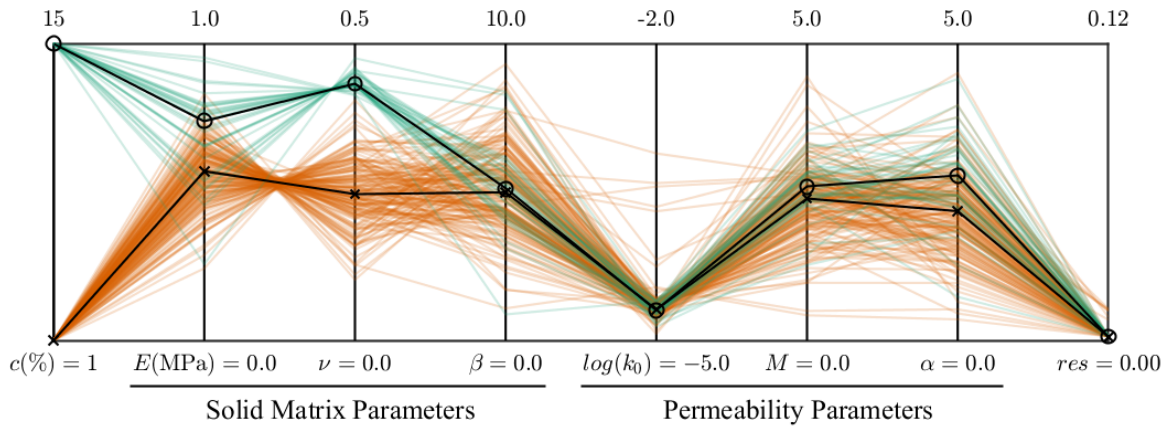


Figure 6.5. Parallel coordinate plot of the fit parameters. (A) The initial conditions as inputs to the optimization procedure and, (B) the resulting fitted parameters for samples meeting the optimization criterion. In each plot, the left most coordinate indicates the concentration of the solution, followed by six model parameters, and the right-most coordinate indicates the corresponding residual value of the cost function. The median of fit parameters are plotted for 1% SPEG (cross sign) and 15% SPEG (open circle). k_0 is in $\text{mm}^4(\text{Ns})^{-1}$. Parameters are defined in Section 6.2.6

were linearly correlated (Fig. 6.6 and Fig. 6.7A). This is an indication of these parameters' effects not being independent of one another. In other words, identifying independent values for E and ν only from the osmotic experiments is not possible. However, based on the correlation of the E and ν we calculated the bulk modulus K (Eq. (6.8)). This resulted in $K = 0.376 \pm 0.022$ MPa and $K = 1.843 \pm 0.031$ MPa for the tension and compression tests, respectively. Interestingly, these values were almost five-folds different ($p < 0.05$), indicating a clear tension-compression nonlinearity in

the transverse direction (Fig. 6.7)

6.3.3 Tendon permeability during tensile tests

We evaluated the transverse hydraulic permeability as a function of J , by using the fitted permeability parameters (Table 6.1 and Equation (6.7), for the range of $0.8 < J < 1$, which approximately corresponds to the range of volumetric strain of $-20\% < \epsilon_{vol} < 0$ (Fig. 6.8). Our results indicated that under tensile loading in tendon ($J < 1$), the transverse permeability decreases with decreasing J . Based on this deformation regime, k decreased almost one order of magnitude from $\sim 10^{-5} \text{ mm}^4(\text{N s})^{-1}$ at $J = 1$ to $\sim 10^{-6} \text{ mm}^4(\text{N s})^{-1}$ at $J = 0.8$ (Fig. 6.8).

6.3.4 Distribution of fluid flow and deformation

The main mode of transportation of nutrition and cellular-waste in tendon is through fluid flow. Evaluation of the transverse poroelastic parameters of tendon enables finite element simulation of this transport phenomena. Therefore, we simulated the spatial and temporal distribution of fluid flow at the boundary during osmotic loading for both tension (1% SPEG) and compression (15% SPEG). The fluid flow was inwards for the tension osmotic loading, which was in the opposite direction to the deformation of tissue (Fig. 6.9 and supplementary Fig. G.1). Conversely, for compression

Table 6.1. The overall median poroelastic parameters and the range of the resulted fit parameters

		Solid Matrix Parameters			Permeability Parameters		
		E (MPa)	ν	β	k_0 ($\text{mm}^4(\text{N s})^{-1}$)	M	α
Tension	(1% SPEG)						
	Median	0.570*	0.247*	4.993	2.057×10^{-5}	2.391*	2.179*
	Min	0.243	0.102	1.086	1.167×10^{-5}	0.425	0.356
	Max	0.831	0.405	9.313	7.779×10^{-4}	4.447	4.508
Compression	(15% SPEG)						
	Median	0.740*	0.433*	5.109	2.013×10^{-5}	2.591*	2.776*
	Min	0.257	0.413	0.882	1.384×10^{-5}	1.272	0.736
	Max	0.953	0.476	8.375	2.549×10^{-5}	3.530	4.405

* the tension and compression medians are different ($p < 0.05$).

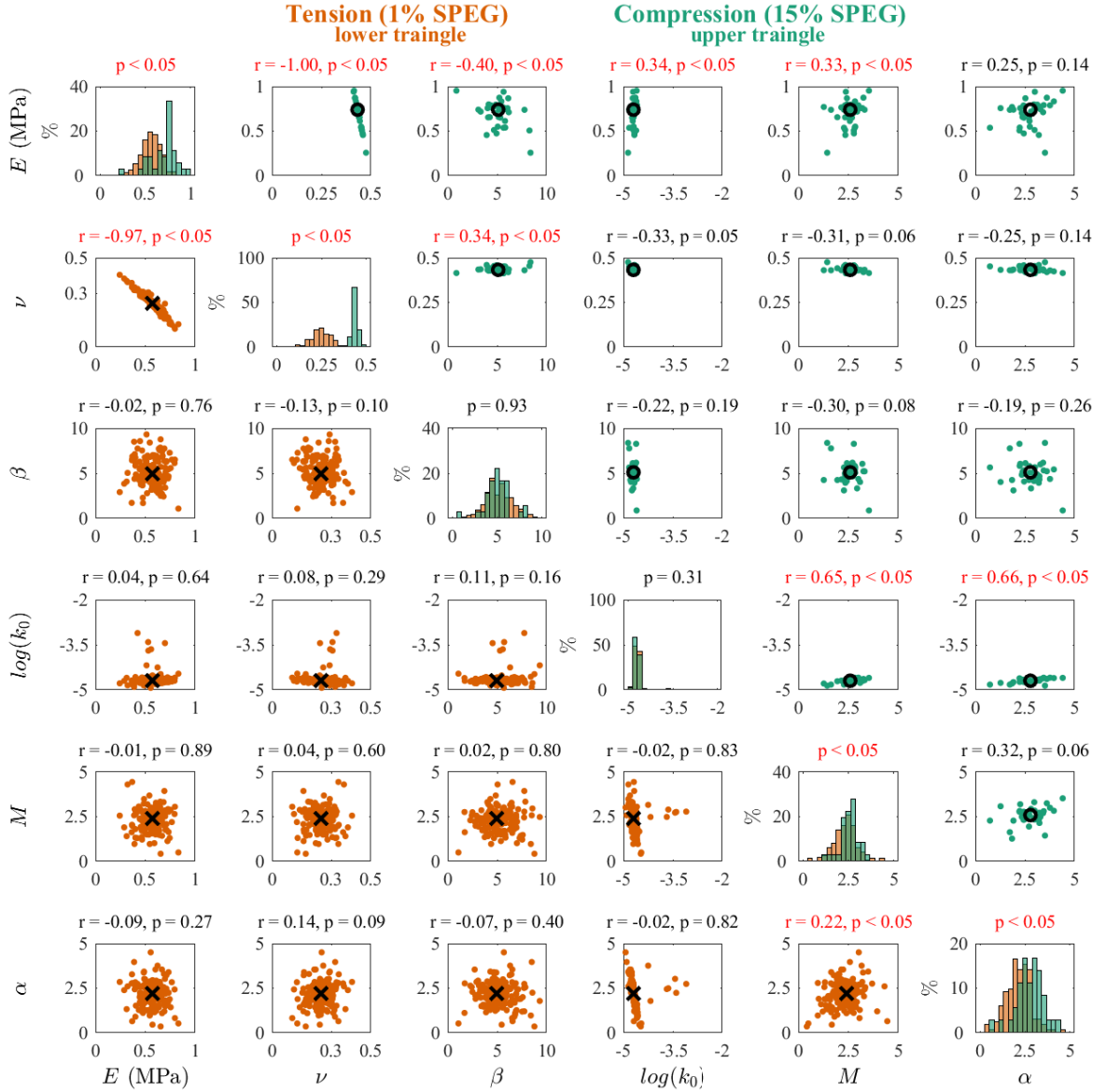


Figure 6.6. Correlation matrix for tension osmotic loading (lower triangular matrix), and compression osmotic loading (upper triangular matrix), and frequency distribution of the fit parameters (main diagonal of the matrix). The median of fit parameters are also marked for tension osmotic loading (cross sign) and compression osmotic loading (open circle)

osmotic loading fluid left the boundary in the opposite direction to displacement of the boundary (Fig. 6.9 and Supplementary Fig. G.1).

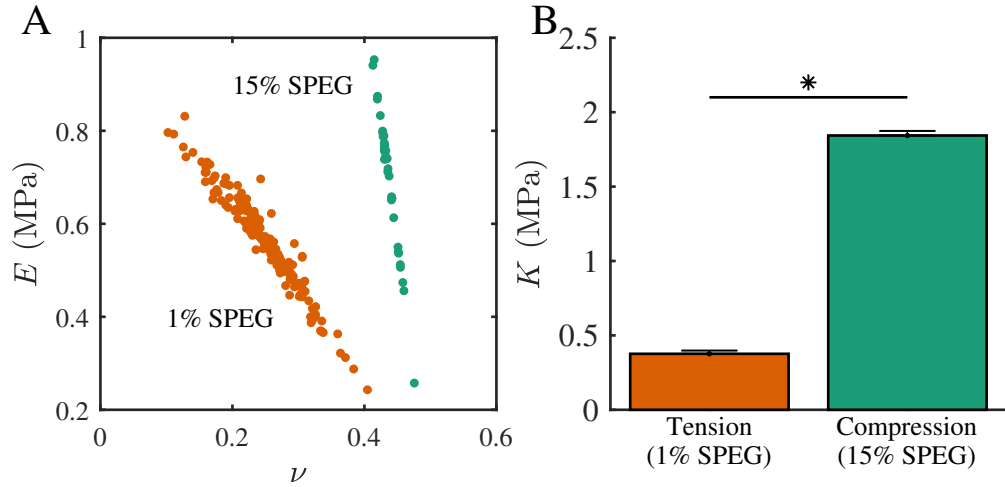


Figure 6.7. Correlation between modulus (E) and (ν) indicates bulk modulus from tension osmotic loading is almost five folds smaller compared to the bulk modulus from the compression osmotic loading case that indicates a tension-compression nonlinearity.* $p < 0.05$

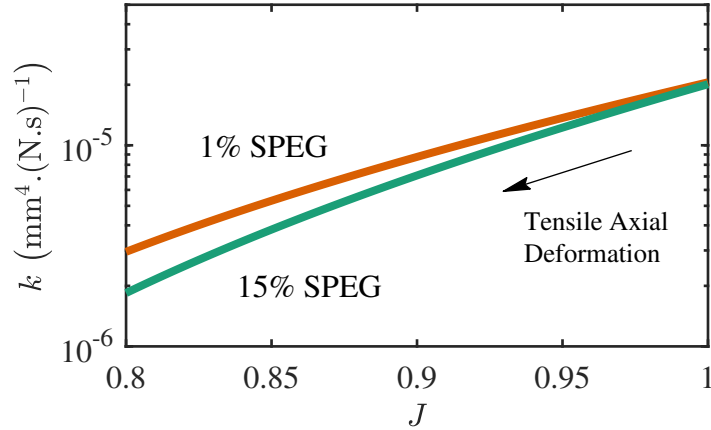


Figure 6.8. Predicted deformation-dependent tendon hydraulic permeability shows that tendon's hydraulic permeability is at $10^{-4} - 10^{-5} \text{ mm}^4(\text{N s})^{-1}$ at the unloaded configuration ($J = 1$) and it decreases by a decrease in volume. Such decrease is expected during axial tensile loading of tendon.

6.4 Discussion

We used a combination of osmotic loading and biphasic FE modeling to evaluate the poroelastic properties of tendon in the transverse direction. Importantly, we calculated the reference permeability (k_0) of tendon that is in the order of 10^{-4} to $10^{-5} \text{ mm}^4(\text{N s})^{-1}$ (10^{-16} to $10^{-17} \text{ m}^4(\text{N s})^{-1}$) (Fig. 6.5 and Table 6.1) and showed that tendon has tension-compression nonlinearity in the transverse direction by approximately

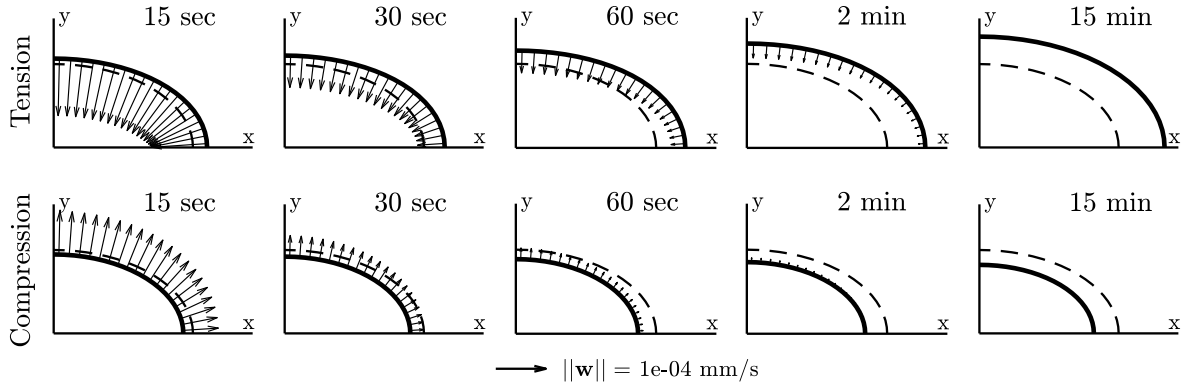


Figure 6.9. Spatial and temporal distribution of fluid flow (black arrows on the curved edge) and displacement on the boundary over time (15 sec until 15 min) for both tension (top) and compression (bottom). For both of the solutions, the deformed (solid) and undeformed (dashed) boundaries are shown. The deformation is scaled five-times for easier visual detection. The simulations show influx of fluid in tension osmotic loading and exudation of water in the compression osmotic loading. The fluid moves in the opposite direction of the deformation. In both of the solutions flow is highest along the minor axis (y-axis).

five-folds higher bulk modulus in compression compared to tension (Fig. 6.7).

One important contribution of this study is reporting of a narrow range for the transverse hydraulic permeability of tendon. When comparing this range to that of the other hydrated fibrous tissues, such as articular cartilage, intervertebral disc, and ligament, which are usually in the range of 10^{-4} to 10^{-2} $\text{mm}^4(\text{Ns})^{-1}$ [13, 41, 84, 98], we see that the hydraulic permeability for tendon is small. This is likely due a denser collagenous network in tendons. In addition, it is possible that the use of phosphate buffered saline (PBS) in the previous experiments may have overestimated actual k_0 at physiological hydration. PBS increases water content and interfibrillar spacing of tissue [78, 194], hence, it is likely to alter tendon's hydraulic permeability as well.

Interestingly, we observed tension-compression nonlinearity in the transverse direction. Tendon's fibrous structure directly impacts its mechanical response. It is well-known that tendons are orders of magnitude stiffer in axial tension compared to axial compression, which is by definition a tension-compression nonlinearity in the axial direction [21, 94]. Our results indicate tendon has tension-compression nonlinearity in the transverse direction as well. This is supported based on two observations. First,

the transverse strain was larger for tension osmotic loading (1% SPEG), despite its smaller relative pressure compared to the pressure in compression osmotic loading (15% SPEG). Second, and more prominently, the modeling parameter identification showed a smaller bulk modulus K from tension tests compared to compression ones (Fig. 6.7). While the structural source is not known, it maybe due to the contribution of the transverse stiffness of fibrils that may push against each other in compression and other more complex micro-scale structures such as helical fibril structures [107, 184].

Axial loading engages the fibrous matrix and thus the relative contributions of fluid flow and solid matrix viscoelasticity can not be distinguished in the axial stress response. In this study we focused on fluid-flow viscoelasticity mechanisms and eliminated the effect of axial fibrils by uniformly loading the tissue in the transverse direction by osmotic pressure. This mode of loading does not engage the axial fibrils. This was verified by the lack of change to the axial force during osmotic loading (Fig. 6.2). Further theoretical argument can be made to support this observation. Since tendons have a large axial-to-transverse Poisson's ratio (i.e., ν_{zx} and $\nu_{xz} > 2$ Fig. 6.1C) [131, 176], one can use an estimation based on transverse isotropic symmetry that the transverse Poisson's ratio can be estimated as $\nu_{xz} = \nu_{zx}E_x/E_z$, where E_z (axial modulus) is extremely large compared to E_x (transverse modulus). Hence, transverse loading will not induce a significant axial response. This may not be the case for tissue with non-axial fibrous component, and for those cases osmotic loading in transverse direction should induce an axial force response [55].

In this study, we used SPEG buffer (polyethylene glycol plus physiological saline) at different concentrations as a means to osmotically load the tendon samples in transverse tension and compression, which changes the water content of tissue and causes volumetric strain. SPEG is the suitable choice of buffer solution for osmotically loading tendon, because unlike buffers based on small solutes such as NaCl and sucrose, it can control water content without infusion of solutes into tissue, and more importantly, it does not alter mechanical behavior over long-term exposure [130, 183, 194, 197, 210, 221]. As a new observation on the effect of SPEG buffer on tissue, we recorded the temporal

response of the transverse and volumetric strain in response to osmotic loading, and made comparisons between change to water content and volumetric strain (Fig. 6.4, and Fig. 6.3B). A change to water content of tissue often affects its fibrous structure and geometry [78,194]. Here, despite the significant volumetric strain in 1 % and 15% SPEG (Fig. 6.3B), surprisingly, the effects of osmotic loading on water content were variable (Fig. 6.3). This was unexpected based on prior observations [183]. However, it should be noted that water content was a secondary measurement and it was performed after the osmotic loading protocol and gripping (Fig. 6.1). The experiment was not specifically designed for measurement of water content, which may have contributed to the unexpected finding of weak and no difference in 1% and 15% SPEG.

Simulation of the temporal fluid flow from the boundary of tendon (Fig. 6.9 and supplementary Fig. G.1) showed that exudation and influx of fluid is not uniform spatially or temporally. The direction along minor axis of the elliptical cross-section had a higher fluid transfer in both tension and compression compared to the direction along the major axis (Fig. 6.9). The non-uniformity of the fluid flow is directly correlated with the geometry, and for a tendon with a higher eccentricity, the effects would be more prominent [187]. Since tendons have a poor vascular structure, infusion of nutrition through fluid transportation plays a crucial role in supplying the cellular component of tendon [72], therefore, the spatial non-uniformity of fluid transport would be an important aspect in understanding adaptation of tissue to injury, and for tissue engineering [79, 119, 203].

It is worthwhile to point out that only by using a multi-start approach for the optimization we could identify that there is a correlation between modulus and Poisson's ratio, where there are many combinations of these parameters that can be used as a solution. We used this observation to calculate and report the bulk modulus as the material property, which was the identifiable solid structure parameter from these experiments. However, this could easily have been overlooked if an optimization with a single judicial or random initial guess, or a global optimization techniques such as genetic and particle swarm algorithms were used. Hence, we recommend a multi-start

approach for model parameter optimization and careful inspection of the fit results for valid and thorough optimization.

This study has some limitations. We evaluated transverse permeability of tendon, but the axial permeability was not studied. During axial loading of tendon, the axial flow should be minimal due to the mostly parallel structure of tendon with a high aspect ratio. Further, we only studied tendon by keeping it at axial unloaded reference configuration. It is likely that imposing an axial tension would alter the results. Lastly, we used rat tail tendon fascicles, which despite their acceptance in the field of tendon mechanics as a useful model system, are not load-bearing and have a relatively simple structure. It is likely that for studying more complex load-bearing tendons, further considerations need to be made such as the role of axial permeability and the possibility of off-axis deformations.

In conclusion, we calculated tendon's poroelastic properties in the transverse direction, including deformation-dependent transverse hydraulic permeability and bulk modulus, by osmotic loading and biphasic mixture modeling. We used transverse osmotic loading that minimizes the effect of axial fibers on the mechanical response. This study is significant in providing a reliable method to calculate hydraulic permeability and providing transverse poroelastic mechanics of tendon in both transverse tension and compression.

Chapter 7

HELICAL FIBRILLAR MICROSTRUCTURE OF TENDON USING SERIAL BLOCK-FACE SEM AND A MECHANICAL MODEL FOR INTERFIBRILLAR LOAD TRANSFER

These findings are accepted for publication in *Babak N. Safa, John M. Peloquin, Jessica R. Natriello, Jeffrey L. Caplan, Dawn M. Elliott. 'Helical Fibrillar Microstructure of Tendon using Serial Block-Face Scanning Electron Microscopy and a Model for Interfibrillar Load Transfer,' Journal of the Royal Society Interface (2019) (<http://dx.doi.org/10.1098/rsif.2019.0547>)*

7.1 Introduction

Tendon's hierarchical structure allows for load transfer between its fibrillar elements across multiple length scales [110, 162, 195], which results in remarkable capabilities to withstand stress and endure repetitive loading [203]. The microscale structure and function are particularly important, because this is the scale where the cells and their surrounding collagen fibrils interface, and these mechanical interactions can have important physiological and pathological contributions. In particular, there is evidence of microscale sliding and shear load transfer that is highly likely to represent sliding between fibrils at small strains (less than 2%); and at larger strains this microscale sliding is nonrecoverable indicating tissue damage [120, 195, 216] (Fig. 7.1). However, the underlying mechanisms of load transfer between tendon fibrils are still unknown. Tendon fibrils are collagenous structures (diameter ~ 100 nm) that are the building blocks of tendon microstructure [109]. The fibrils are responsible for supporting external mechanical loading. Interfibrillar matrix molecules such as glycosaminoglycan chains (GAG) have been postulated to be responsible for load transfer between fibrils [2, 172];

however, removal of a wide range of interfibrillar matrix components, including GAG, does not affect the mechanical response [217], or has minimal consequences [61]. It is not likely that the load transfer in tendon is solely, or majorly, mediated via interfibrillar matrix. Thus, the microscale architecture of the collagen fibrous network itself is likely to have a role in mediating load transfer.

Serial block-face scanning electron microscopy (SBF-SEM) makes it possible to visualize the 3D microscale architecture of tissue in great detail, and to reveal the fibrillar architecture with several mechanical implications [163, 207]. SBF-SEM is an advanced electron microscopy technique that takes sequential SEM images of the cross-section of tissue; these images combine to provide a three-dimensional view of the microstructure [83, 207]. Using SBF-SEM with a short scan depth ($8.7 \mu m$), our group showed that there is a small fibril angular dispersion and that the fusion/branching of small fibrils might be responsible for interfibrillar load transfer [217]. Longer scan depths ($\sim 100 \mu m$) showed that fibril fusion/branching and fibril ends also exist in tendons [209], and that helical fibril patterns form in microscale during tendon development in juvenile tail tendons [107, 206]. The existence of helical fibrils in collagen microscale and nanoscale was shown using two-dimensional light, atomic force, electron, and X-ray scattering microscopy in tendons and other collagenous tissues [23, 45, 65, 67, 108, 127, 153, 173]; however, these visualizations do not provide the details of the 3D fibrillar structure.

Experimental observations and finite element (FE) modeling suggest that helical structures in tendon may have significant mechanical effects. The rotation and high Poisson's ratio observed during tendon's axial loading have been attributed to such structures [24, 175, 222]. Furthermore, some FE models have studied the groups of helical fibrils by combining the fibrils with interfibrillar matrix in a mesh to produce the nonlinear stress response of fascicles [26, 175]. Despite the potential of helical fibril organization to affect tendon's microscale mechanics, little is known about individual groups of helically wrapped fibrils and their mechanical implications. We hypothesized that helical wrapping can induce frictional load transfer between fibrils, allowing for

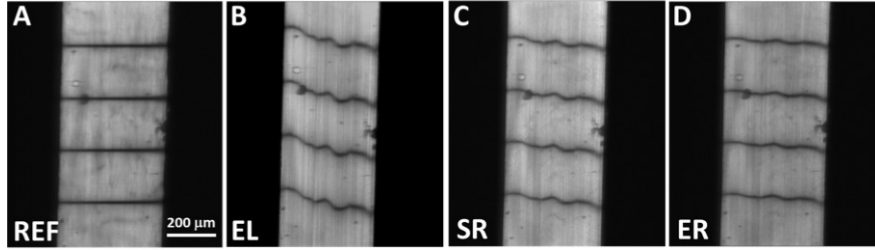


Figure 7.1. Microstructural sliding during micromechanical tensile testing of tail tendon in reference (REF), end of ramp loading (EL), starting of stress relaxation (SR), and end of relaxation (ER) (courtesy of Lee and co-workers [120])

mechanical interfibrillar load transfer without an intermediate matrix. This would imply that friction between helically wrapped fibrils can contribute to load transfer, in addition to interfibrillar matrix shear and fibril fusion/branching.

The scope of this contribution was to visualize the three-dimensional fibril organization of rat tail tendon and to study the potential of interfibrillar friction within helically wrapped groups of fibrils to serve as a mechanism for load transfer. First, we visualized the microstructure of tendon in three dimensions using SBF-SEM. We found a complex network, with many helically wrapped fibrils. These observations informed the second part of this study, in which we used finite element (FE) analysis to test the hypothesis that frictional contact between helically wrapped fibrils can transfer stress (load) between fibrils without a need for a mediating matrix. This study elucidates new aspects of tendon microstructure, providing a detailed image of fibril tortuosity, fusion/branching, and organization into helical groups. Importantly, our results establish interfibrillar friction as a new mechanism for interfibrillar load transfer, among the several proposed load transfer mechanisms, advancing our knowledge about microscale structure-mechanics relationships.

7.2 Methods

7.2.1 Serial block-face SEM imaging

A tail tendon fascicle from a three-month-old male Sprague-Dawley rat was dissected as previously described [183], and used for SBF-SEM imaging. To prepare

for imaging, the fascicle was equilibrated in PBS for 8 hours, consistent with other studies [183, 195], which may have increased interfibrillar spacing and fibril diameter [78], but likely did not alter overall structure such as tortuosity, and then soaked overnight at 4°C in a solution of 2% glutaraldehyde and 2% paraformaldehyde in 0.1 M sodium cacodylate buffer. The sample was subsequently stained and resin-embedded, according to established techniques [207].

The transverse cross-section was scanned in series under 1.78 kV in low-vacuum pressure with three microseconds dwelling time using an Apreo VolumeScope (Thermo Fisher Scientific, Waltham MA). After the end of the scanning of each section, a 200 nm layer of the block's face was removed by means of a mechanical slicer and the scanning was repeated. Alignment was maintained by keeping the block was fixed in place throughout the imaging process. The in-plane resolution of the scans was 10 nm/pixel with 432 slices that covers a total volume of $(20.27\mu\text{m} \times 16.74\mu\text{m} \times 86.20\mu\text{m})$, where the third dimension is measured along the fascicle's axial direction.

7.2.2 Segmentation and data analysis

The SEM images were smoothed using a Gaussian blur filter and a representative subset of fibrils were manually segmented through the entire 3D image stack (Fig. 7.2A). Only fibrils that spanned the entire image stack, as many fibrils did not entirely fit in the scanned volume or some fibrils were otherwise discontinuous, were used for analysis ($n = 42$ fibrils). The segmentation was done using Seg3D (seg3d.org). Since the axial distance between subsequent images was small (200 nm) the fibrils appear as approximately circular spots that move in-plane allowing for the fibrils to be inspected and tracked through the image stack (Fig. 7.2A-C).

To confirm that the manually segmented fibrils were a representative selection of all the fibrils, we segmented all fibrils in each of ten equally spaced 2D sections by thresholding (ImageJ, imagej.nih.gov). The distribution of fibril diameter was calculated and compared to that of the manual 3D fibril segmentations by using Wilcoxon rank sum test (Fig. 7.2D and E). The distributions were similar, and the medians of

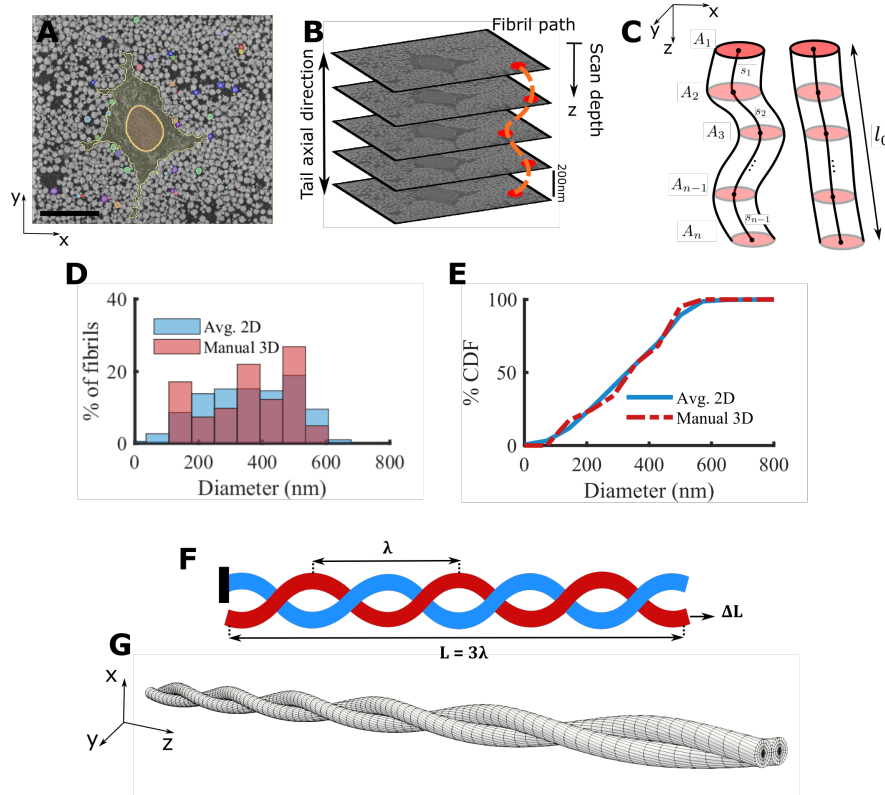


Figure 7.2. Experimental methods for SBF-SEM imaging and analysis (A) Representative SEM image and in-plane segmentation (scale bar = $5 \mu m$), (B) SBF-SEM imaging process showing sequential stacks of images and a schematic fibril label (dotted orange line) along the tendon length, (C) schematics of fibrils with large (left) and low (right) tortuosity that shows the cross-sectional area (A_i) of fibrils throughout the scan depth and the incremental distance (s_i) between the center of the fibrils. By comparing the (D) distribution and (E) cumulative distribution function (CDF) of the diameter using the averaged 2D automatic segmentation of all fibrils (blue) and the 3D manual segmentation of a subset of 42 fibrils (red), it is evident that the manually segmented fibrils are a representative of the full fibril population. (F) For the finite element analysis a model with three full turns is used ($L = 3\lambda$). The boundary condition is that one fibril (blue) is anchored (left), while the other fibril (red) is pulled in the axial direction (arrow, right) to a deformation of $\Delta L = L\varepsilon$. (G) The mesh used for the finite element simulations shows that the fibrils were initially in contact throughout the length.

the fibrils were not different ($p = 0.927$). The manual 3D fibril segmentations were used for all subsequent analysis.

To determine the variation in fibril diameter along the length, we calculated the normalized diameter of each fibril in each section in the image stack. The normalized

diameter for a fibril at section i is defined as

$$\bar{d}(z_i) = \frac{d(z_i)}{\tilde{d}} \quad (7.1)$$

where z_i is the scan depth, $d(z_i) = \sqrt{4A_i/\pi}$ is the diameter of the fibril, A_i is the cross-sectional area of the fibril, and \tilde{d} is the median of $d(z_i)$ across all sections (Fig. 7.2C). To quantify the complexity of the fibrillar network, we calculated the percent tortuosity for each fibril as

$$\tau = \left(\frac{\sum_{i=1}^{N-1} s_i}{l_0} - 1 \right) \times 100. \quad (7.2)$$

Here, l_0 is the end-to-end distance of the fibrils, and s_i is the magnitude of the 3D vector between adjacent fibril slice centroids, and N is the number of sections (Fig. 7.2C). Half of the segmented fibrils ($n = 21$) were in helical groups; for these groups, we calculated the pitch (λ) by dividing the total scan depth (86.20 μm) by the average number of turns. Note that tortuosity is a combination of tortuosity along the helical axis and of the helical turns themselves. For a high aspect ratio helix, as in this study, the contribution from the helical turns is small.

7.2.3 Statistics

The variation in diameter of fibrils along the length was tested by calculating, for each section, the 95% confidence interval of normalized diameter (Eq. (7.1)). To test the correlation between fibril diameter and tortuosity, we conducted a linear regression analysis between \tilde{d} and τ for the fibrils in the helical groups and others, separately, using Pearson's correlation method. Statistical significance was defined as $p < 0.05$.

7.2.4 Finite element analysis of helical fibril structures

Helical wrapping of fibrils around each other was a commonly observed feature, and we hypothesized that this helical wrapping may provide interfibrillar load transfer. To study this, we developed a three-dimensional finite element (FE) model of a pair of helical fibrils in contact (Fig. 7.2F and G) using FEBio software (FEBio2.8 febio.org)

[132]. Based on the SBF-SEM microstructural analysis, the fibril diameter was taken to be 200 nm (within the range, *median* [*min*, *max*], of segmented fibril diameters 378 [128, 565] nm, see Results), and consistent with previous values for fibril diameter using TEM measurements of median diameter of 144 nm for non-incubated and 161 nm for PBS-incubated samples [114]. Additionally, the helix pitch was set at 40 μm (within the range of measured pitch 38 [22, 86] μm , see Results). The entire model included three full fibril revolutions (i.e., $L = 3\lambda$ where L is the total length). The boundary condition was set as that each fibril had one free-end. In one fibril, the opposite end was anchored; in the other fibril, it was set to move to create 8% axial strain (Fig. 7.2F). The value of 8% was selected from experimental data as the maximum tissue strain that fibrils may experience prior to tissue failure [120].

We used an isotropic compressible neo-Hookean constitutive relation for the fibrils [22]:

$$\Psi(I_1, J) = \frac{E}{4(1 + \nu)}(I_1 - 3) - \frac{E}{2(1 + \nu)} \ln J + \frac{E\nu}{2(1 + \nu)(1 - 2\nu)}(\ln J)^2 \quad (7.3)$$

Where, Ψ is the strain energy, I_1 is the first invariant of the right Cauchy-Green strain tensor, J is the Jacobian of deformation, E is the Young's modulus, and ν is the Poisson's ratio.

To solve the frictional contact problem between the fibrils we employed the penalty method regularized with an augmented Lagrangian scheme that has been implemented in FEBio [248]. This method is surface-to-surface method, which is a robust algorithm to solve frictional contact problem that would require specialized smoothing, or higher order shape function by using node-to-surface (NTS) method [248]. In the initial configuration the fibrils were in contact along the entire length. We used a mesh consisting of 20,160 elements (hexahedral trilinear and linear pentahedral wedge) and 23,478 nodes based on a mesh sensitivity analysis (Fig. 7.2G). To improve the stability of the contact algorithm we used an auxiliary frictionless external cylindrical sheath

with a weak modulus (10% of fibril modulus) to prevent separation in the intermediate steps of the iterative FE solver (Fig. H.1). The auxiliary sheath was effective in increasing the stability of the model, and did not alter the final solutions. This was confirmed by using different moduli for the sheath between 0.1% and 1000% of the fibril modulus; the same mechanical response was produced in each case.

The reaction force at the anchored end of the fixed fibril was divided by the cross sectional area and used as the measure for load transfer. To assess the sensitivity of the load transfer, we performed a one-at-a-time parametric sensitivity analysis by varying the model parameters in a range according to the reported values in the literature for fibril properties as summarize in Table 7.1 [32, 71, 128, 142, 216, 237, 238, 243]. and for geometry based on the range in this study. According to the summary of literature parameter, the initial values for model parameter sensitivity analysis for solid material was set as $E = 1$ GPa, $\nu = 0.2$. The friction parameter between fibrils was set as $\mu = 0.5$, and the helix pitch was set as $\lambda = 40 \mu m$. We studied the following cases by changing one parameter at a time: $E = 0.1$ to 10 GPa, $\nu = 0$ to 0.4, $\mu = 0$ to 2, $\lambda = 20$ to 80 μm . Since the experimental data for frictional coefficient of fibril-on-fibril is not available, we used an estimated range ($0 < \mu < 2$) based on AFM indentation tests [32]. The maximum value of Poisson's ratio was set to 0.4, which was a practical decision to avoid computational singularity due isotropic material incompressibility limit of $\nu = 0.5$.

To evaluate the spatial distribution of the induced stress and deformation in the fibrils we plotted axial stress and we also plotted the normalized displacement (\bar{u}) relative to the mid-section of each fibril along the axial direction. We defined normalized displacement as

$$\bar{u} = \frac{1}{\lambda} (u(z) - u(L/2)) . \quad (7.4)$$

Here, $u(z)$ is the axial displacement at position z along the fibril length.

Table 7.1. Collagen fibril mechanical properties: Young’s modulus (E), Poisson’s ratio (ν), frictional coefficient (μ) in tendon unless otherwise noted

E (GPa)	ν	μ	Method	Tissue	Reference
0.1-10	0-0.4	0-2	-	Rat tail	Current study’s range
0.326±0.112	-	-	Tensile test MEMS	Rat patellar	[128]
0.6±0.2	-	-	Tensile test AFM	Bovine Achilles	[243]
0.3-1.2	-	-	Atomistic modeling	-	[71]
1.6±0.4	-	-	Shear-lag curve fitting	Rat tail	[216]
1.2-2.2	-	-	Indentation AFM	Bovine Achilles	[142]
3.75-11.5	0-0.5	-	Indentation AFM	Rat tail	[238]
-	2.1±0.7	-	X-ray diffraction	Bovine pericardium	[237]
-	-	~ 0.4	Indentation AFM	Collagen film	[32]

7.3 Results

7.3.1 Microstructure of fibrils and SBF-SEM

To describe the microstructure of tendon, we segmented fibrils from the SBF-SEM images in three-dimensions. The segmentation indicated that although the fibrils are mostly axially-aligned, they create a complex network around the cells (Fig. 7.3A). From the manually segmented fibrils we quantified the fibril diameter throughout the scan depth (Eq. (7.1)) and the percent tortuosity (Eq. (7.2)). As expected, the fibrils’ diameter did not vary along the scanned fibril length of 86.20 μm (Fig. 7.3B), which is consistent with previous findings [209]. Note that the normalized fibril diameter Eq. (7.1) was not significantly different than one across the scan depth (Fig. 7.3B). This observation supports the use of a single median diameter value assigned to each fibril for correlation with the tortuosity. We quantified the % tortuosity (τ) of each segmented fibril Eq. (7.2), and calculated its correlation with the median diameter of the fibrils. This showed that for all of the fibrils, τ was small ($< 1\%$) and for the fibrils in helical groups tortuosity was correlated with diameter ($r = -0.59$, $p < 0.05$), where for the other fibrils it was the same across the diameter sizes ($r = 0.12$, $p = 0.616$) (Fig. 7.3C). As a result, the smaller fibrils in helical groups are more likely to have higher tortuosity, and thus have a more complex structure. For the tortuosity analysis, one fibril that made a right-angle turn and passed through the cell membrane (Fig. 7.4C, discussed below) was not included in the correlation. We made several

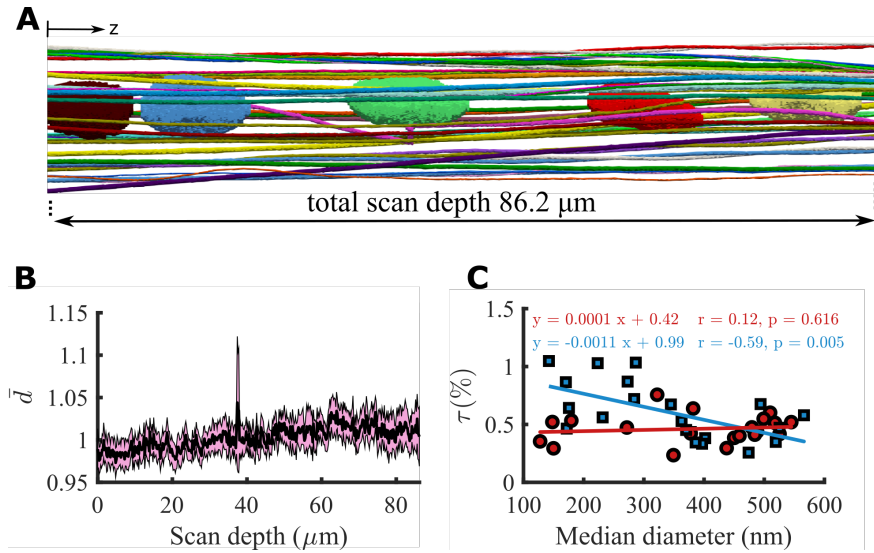


Figure 7.3. Three dimensional segmentation and structural complexity of fibrillar network (A) Lateral view of the three dimensional segmentation along the scan length with cell nuclei. Although the fibrils are primarily axially oriented, they have a complex three-dimensional network. (B) the 95% confidence interval (highlighted in pink) of the normalized diameter (\bar{d} , Eq. (7.1)) contains the unity value throughout the scan depth, which indicates that the diameter of the fibrils does not change along the scan depth. (C) Percent-tortuosity (τ , Eq. (7.2)) was calculated as a measure of the complexity of the fibrillar structure for the fibrils in helical groups (marked with blue squares) and the other fibrils (marked with red circles) separately. The helical fibril tortuosity was correlated with the diameter, with the small diameter fibrils being more tortuous, however, tortuosity was uniform for the other fibrils.

isolated structural observations that have potential mechanical implications: tapered fibril end (Fig. 7.4A and Supplementary Video 1), fibril fusion/branching (Fig. 7.4B and Supplementary Video 2), and one fibril that wrapped around the cells (Fig. 7.4C and Supplementary Video 3). For the tapered fibril end, in the last $\sim 4 \mu m$ of the fibril length (scan depth of 38-42 μm) a reduction in fibril diameter was evident, where the fibril gradually fades away in the image sequence when approaching from the deeper scanned layers (Fig. 7.4A). At the fusion/branching site, a small fibril merges with a larger one, and in the subsequent scanned images the larger resulting fibril branches into two distinct ones. The fusion/branching site approximately spanned 6 μm , where at least two fibrils were not distinguishable (Fig. 7.4B). Another interesting feature was one fibril that made almost a full turn around the cells (Fig. 7.4C). These features

were interesting but were isolated observations in the dataset.

When looking at the axial view of the fibrils, we observed several helical structures (Fig. 7.5 and Supplementary Video 4). In particular, many fibrils locally wrapped around each other, which contained two, three, or more fibrils with both left and right-handed helical configuration (Fig. 7.5 and Supplementary Video 5). Half (21 out of 42 fibril) of the fibrils that we segmented were in helical groups, although the sampling was not purely random. Of these helical fibrils, 13 fibrils had a right-handed twist and 8 were left-handed (Fig. 7.5B). These fibrils made an average of 2.2 ± 0.7 turns around each other along the scan-length (Fig. 7.5 C), that also corresponds to an average $45 \pm 18 \mu m$ helical pitch (λ , the axial length of one full turn as described in Fig. 7.3F).

7.3.2 Finite element simulations of the helical fibrils

We used a finite element model to test our hypothesis that frictional contact between helically wrapped fibrils can transfer stress (load) between fibrils without a need for a mediating matrix. The stress transfer was proportional to the fibril's tensile modulus (Fig. 7.6A). Further parametric studies indicated that there is no change to the transferred stress with a change in Poisson's ratio (ν) (Fig. 7.6B). As expected, the transferred load increased with an increase of frictional coefficient (μ) (Fig. 7.6C). Our results show that the load transfer decreased with an increase in pitch (λ) (Fig. 7.6D).

To evaluate the spatial distribution of stress and deformation along the length of each fibril and its dependence on the friction coefficient, we plotted the axial stress and axial displacement (\bar{u} , Eq. (7.4)) at maximum displacement of the pulled fibril (Fig. 7.7). The fibril stress was zero with no friction ($\mu = 0$, (Fig. 7.7B) and it increased with higher friction coefficient (Fig. 7.7C and D). The axial stress varied linearly along the length of the fibril, increasing with distance from the free boundary and the stress in each fibril was the mirror image of the stress in the other one (Fig. 7.7A-D), which is in accordance with the static equilibrium condition. Similarly, for the fibril deformation, in the zero friction case, there was no axial deformation, hence the fibrils slid freely (Fig. 7.7E). When friction was increased, the induced deformation also

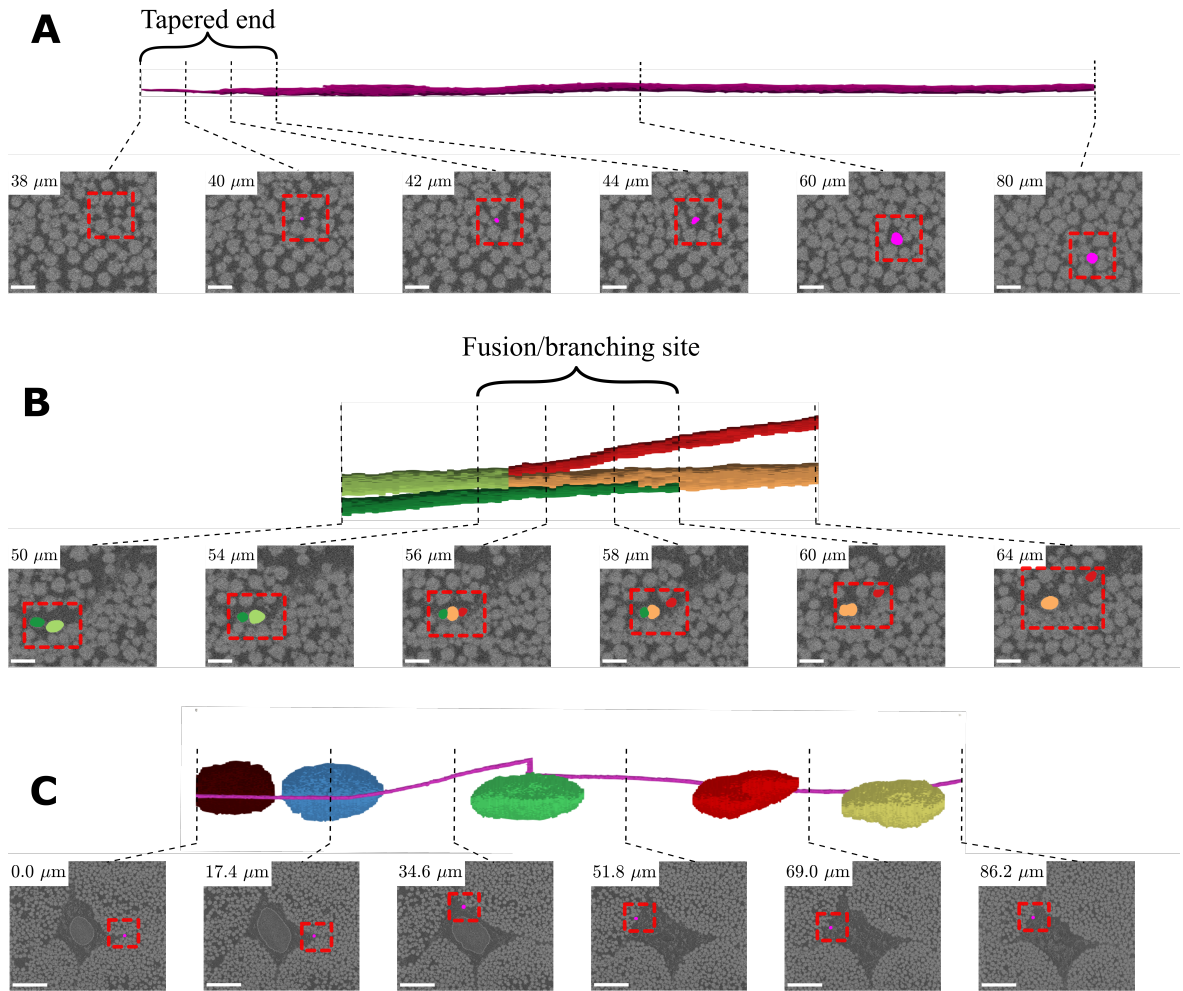


Figure 7.4. Three interesting but isolated structural features were observed: (A) tapered fibril end (B) fibril fusion/branching and (C) a helical fibril that wrapped around cells (only the nuclei are shown). For each feature, the first row includes the 3D segmentation, and the second row shows the segmentation mask overlaid on the SEM section image (dashed red box). In (A) and (B) scale bar = $1 \mu\text{m}$, for (C) scale bar = $5 \mu\text{m}$.

increased, showing a plateau at the free ends indicating no strain, which confirms the stress-free boundary condition imposed on the model (Fig. 7.7F and G).

7.4 Discussion

In this study, we visualized the microscale structure of tendon fibrils in three dimensions using serial block-face scanning electron microscopy (SBF-SEM) and studied the mechanical implications of helical fibrils as a mechanism for interfibrillar load

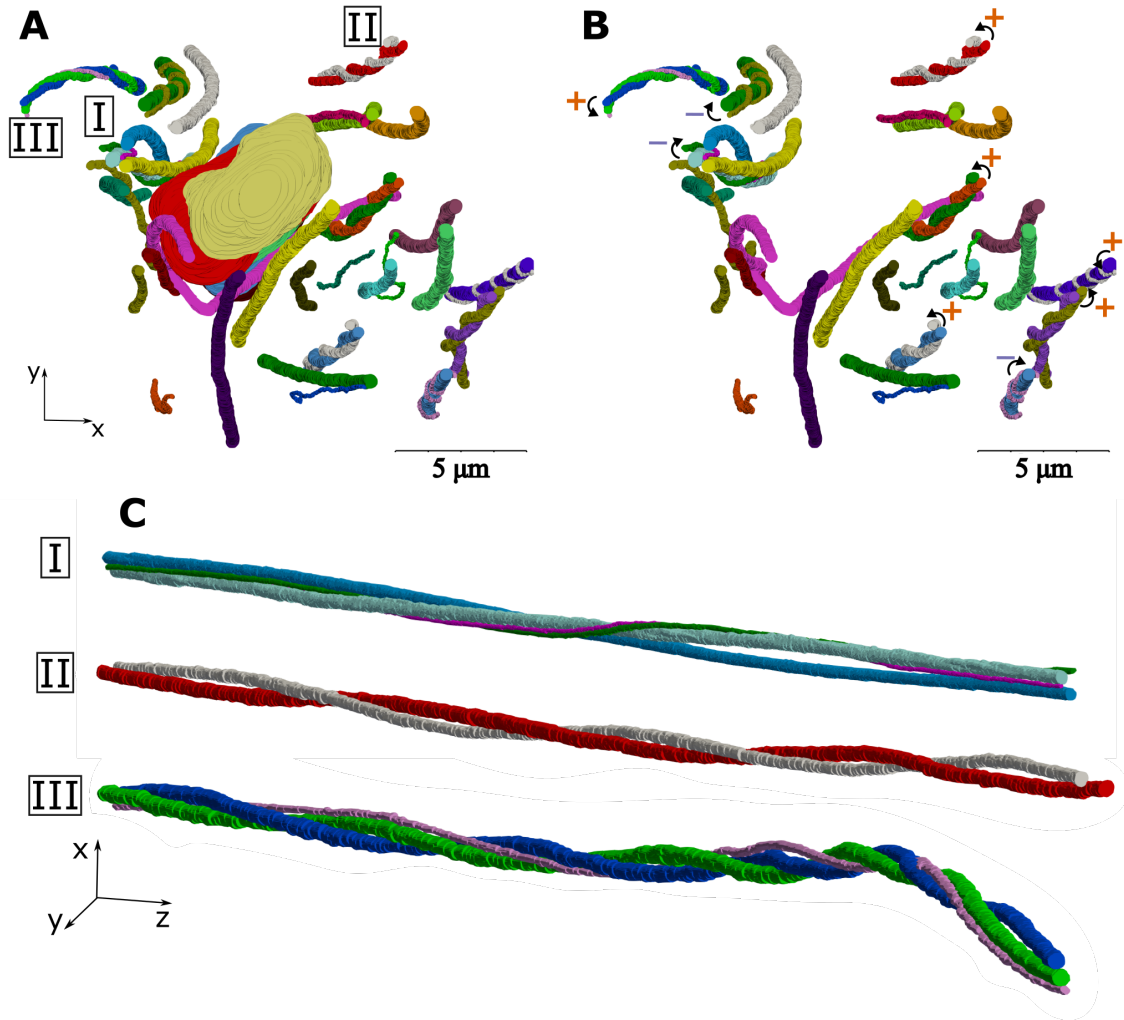


Figure 7.5. Helical fibrils in tendon's fibrillar structure. Many helical structures were observed in the axial view of the fibrils that are evident in the figures (A) with and (B) without the cell nuclei. The helical fibril groups have both right (marked with + ccw arrow) and left-handed (marked with - cw arrow) twist. (C) Shows three examples of the groups of twisting fibrils with pitch ranging from $22 \mu m$ to $86 \mu m$.

transfer using FE analysis. We found that tendon fibrils are not purely parallel structures and there are many helical fibrils that wrap around each other and in groups. Our FE analysis indicated that, in addition to other potential mechanisms of load transfer (interfibrillar matrix and fusion/branching of smaller fibrils), the helical fibrils can also mediate load transfer through frictional mechanical contact.

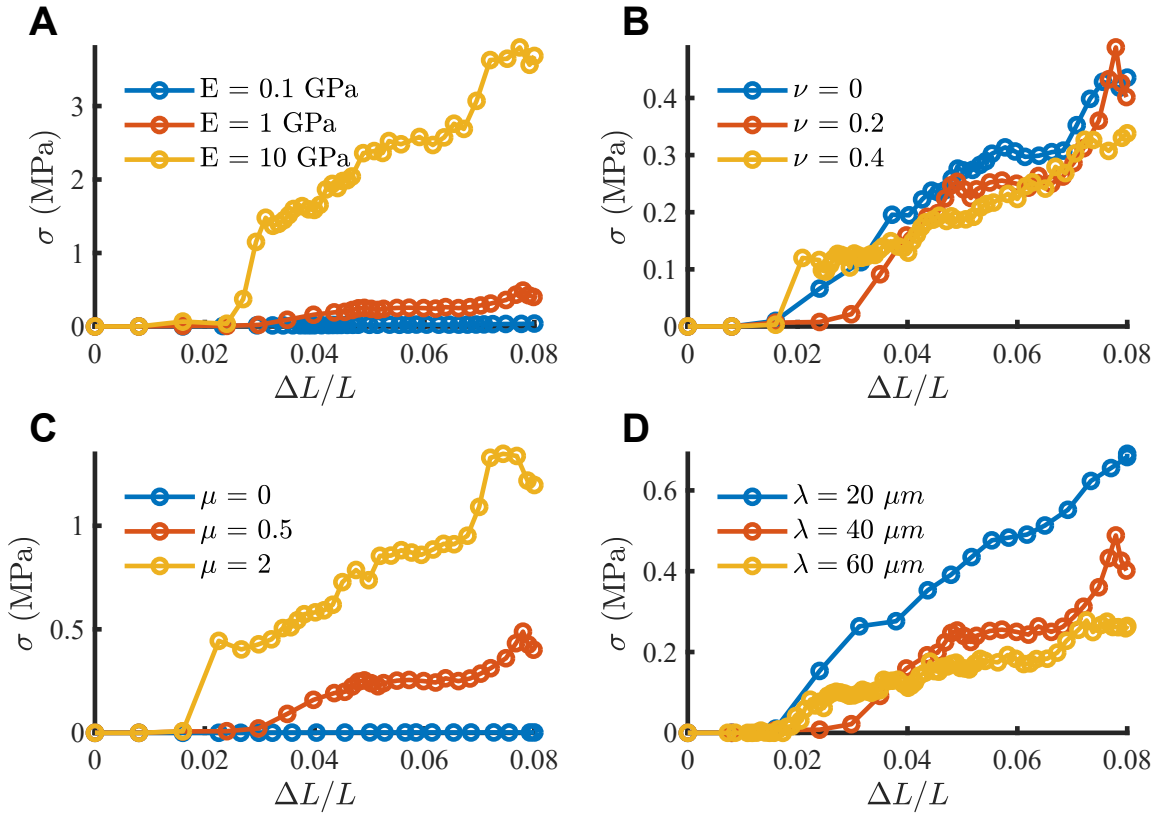


Figure 7.6. Sensitivity analysis of stress transfer due to friction between helically grouped fibrils. Base material properties $E = 1$ GPa, $\nu = 0.2$, $\mu = 0.5$, $\lambda = 40 \mu\text{m}$. The transferred stress (A) increases with fibril modulus E , and (B) is insensitive to Poisson's ratio ν , (C) increases with frictional coefficient μ , and (D) decreases with increasing helix pitch λ .

7.4.1 Microstructure of fibrils and SBF-SEM

We observed helical structures that twisted around each other (Fig. 7.5). The existence of helical fibrils was previously reported [23, 153], and were suggested to be left-handed [67]; however, our findings showed a similar number of the left-handed and right-handed helical fibrils (Fig. 7.5B). The formation of the helical structure has been explained based on a fibrilpositor model of fibril assembly [106, 107] and the helicity of subfibrillar structures [23]. The helical fibril structures explain the rotation of tendon in tension [24]. Additionally, they have been used as an explanation for the macro-scale mechanical behavior of tendon, in particular for the low stiffness at small deformations and the large tensile Poisson's ratio [176, 222]. The grouping of fibrils into helices

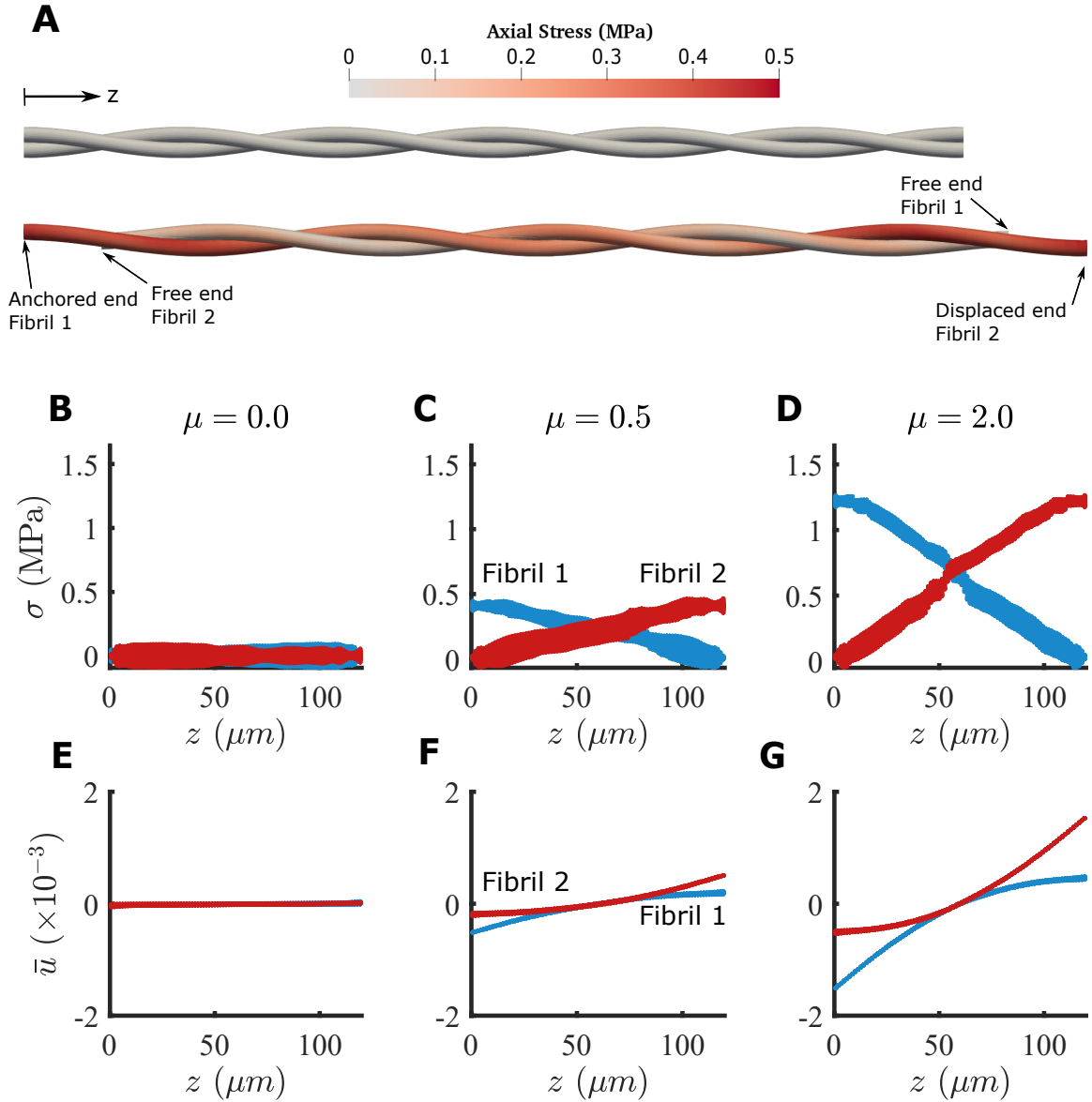


Figure 7.7. Finite element simulation of two helically wrapped fibrils. (A) Axial stress distribution in the fibrils for the undeformed (top) and deformed (bottom) states for $\mu = 0.5$. The geometrical scale is compacted 10 times in the axial direction for clarity. (B-D) Stress along the length of the fibrils, and (E-G) normalized displacement (\bar{u} , Eq. 4) along the length of the fibrils for various choices of friction coefficient μ . With no friction ($\mu = 0$) there was no σ or \bar{u} (B, E). As the frictional coefficient increases, the stress and the deformation increases for $\mu = 0.5$ (C, F) and for $\mu = 2$ (D, G). The model parameters are $E = 1$ GPa, $\nu = 0.2$, $\lambda = 40 \mu\text{m}$.

can mediate load transfer by inducing frictional contact between fibrils during axial loading.

We observed some interesting but isolated features that can have implications for load transfer and loading on cells. For load transfer, we observed a tapered fibril end and fusion/branching, which agree with previous findings [209], with the difference that the tapered end in this study was observed in a “straight” fibril in contrast to the hairpin shape in the previous study. As previously suggested by Szczesny and co-workers [217], an instance of fusion/branching, such as the one described above, could mediate load transfer between fibrils via direct physical connection. A free fibril end like the tapered end can also mediate load transfer by allowing microscale sliding and shear stress, which is a well-documented phenomenon in experimental studies [120,216,222]. Additionally, we observed a fibril that wrapped around the cells, which indicates that during axial loading, lateral compression can be exerted on the cells affecting tendon mechanotransduction [119]. Our fibril diameters and distribution of diameters (Fig. 7.2D and E) were larger than the juvenile tail tendon fibrils [107], and it was consistent with the other tendon studies in mature rat tail tendon [156], however, the incubation in PBS, although facilitating the preparation of sample for fixation and staining by increasing interfibrillar spacing, could have increased the fibril diameter [78,195]. Another potential source of error for fibril diameter would be calculation of diameter based on the circular area assumption used in this study. Due to small dispersion angled of fibrils, this effect should be minimal, however, for future analysis, especially when tortuosity is high, methods such as elliptical fitting could provide a more accurate measurement of fibril diameter [207]. Fibril distribution has recently been related to circadian control [244], however, our study did not control time of day or address this potential mechanism.

The fibril structure assessment was subject to some limitations. The SBF-SEM technique generates large 3D datasets and segmentation is consequently difficult compared to 2D SEM, creating practical limitations in data collection and analysis [209]. Although we consequently chose to do in-depth manual segmentation for only one sample, we performed several scans of additional fascicles and these scans showed similar structural features. Additionally, although the helical fibrils were easily observed and

represented approximately half of the segmented fibrils, based on the current analysis we may not conclude that in general half of the fibrils in tendon are in helical groups; related to this, it is possible that scans that cover larger axial length of fibrils would reveal helices with larger pitch length.

Future work, using 3D automated segmentation will be needed to establish the frequency of helical fibril and quantify helical pitch across a population. Such automatic segmentation methods could then be implemented in studies involving multiple animals at various ages, disease states, or in transgenic mouse models. Such applications would be highly instrumental in determining mechanisms of tendon development and disease, and in developing and testing tendon therapies. A separate limitation of the microstructural analysis is that our observations only included a region near the tenocytes, and other regions further away from the cells might have a different structure. Furthermore, we only scanned the tail tendon, which is a low-stress tendon; further investigation is needed to confirm the existence of helical fibril groups in other tendons.

7.4.2 Finite element simulations of the helical fibrils

Interfibrillar load transfer by friction in a helical contact does not require interfibrillar matrix bonding, but the sum of its contribution over many fibrils and its relative magnitude in comparison to other load transfer mechanisms, such as chemical bonding, remains unknown. Here, the estimated magnitude of the transferred fibril stress ($\sim 0.2\text{--}4$ MPa) was low compared to the ultimate stress of the fibrils' typically in the range of 90 MPa [128], which matches the stress of a single fibril's tensile response based on our model parameters (see supplementary Fig. I.1). The large variation in mechanical parameters of fibrils (Table 7.1) and the unknown accumulation among hundreds of fibrils hinders accurate calculation of the total load transferred in situ by the interfibrillar friction mechanism. Of particular importance, the fibril-on-fibril friction coefficient is unavailable. Thus, more experimental measurements of single fibrils and groups of fibrils are needed for more accurate estimations.

The variations in fibril stress transfer and displacement observed in the parametric FE sensitivity analysis make physical sense (Fig. 7.7). In particular, the dependence of transferred stress with modulus and frictional coefficient are expected based on Hooke’s law and Coulomb’s friction law, respectively, and they were shown using our FE model (Fig. 7.6A and C). Note, however, that while this study used the relatively simplified model of friction contact, additional mechanisms, such as hydrodynamic friction, molecular asperity, and nonlinear dependence of friction coefficient to normal traction and other nano- and micro-scale tribological effects may be at interplay to induce load transfer between and within fibrils in the physiological system [20, 57, 208, 234]. The decrease in reaction force by increasing the pitch of the helix, which is shown in Figure 7.6D, can be explained by a reduction in lateral compression (normal force) on the fibrils as the pitch angle decreases and the fibrils become more parallel. The lack of dependence on Poisson’s ratio was an unexpected observation that might be due to the high aspect ratio of the fibril’s geometry or due to the isotropy of the constitutive relation (Fig. 7.6B). Large Poisson’s ratio in tension ($\nu \sim 2$) have been reported for individual fibrils [237], which is greater than the isotropic limit of $\nu = 0.5$. To include Poisson’s ratio’s effect on the interfibrillar load transfer, anisotropy of the isolated fibril material may need to be incorporated. The curves in Figure 7.6 were not smooth, which is potentially related to the nature of frictional contact that can switch between slip and stick conditions and cause jitter (imagine moving heavy house furniture on ceramic), however the trends are clear, and this does not affect the outcome of the sensitivity analysis.

Interfibrillar friction causes a gradient of axial stress in the fibril. In the simulated cases (Fig. 7.7), the spatial distribution of stress variation and deformation match the distributions of stress and deformation based on established shear-lag theories as applied to tendon fibrils [215]. By using frictional contact, we were able to replicate the linear response in shear lag [215], but did not reach a constant stress plateau, predicted by shear lag model with an intermediating matrix material. Although a region of constant stress is likely to appear with a larger number of helical turns in

the model, it would be extremely difficult to achieve convergence in our FEM contact model with a longer length. Moreover, our actual scan length was only $86.20 \mu\text{m}$ and our current FEM is already extrapolated to a maximum length of $180 \mu\text{m}$. Thus, if we were to model an even longer length, we would have to extrapolate even further, which we do not think is appropriate. To further put this study in the context of prior research on theory of wire ropes, it should be mentioned that, unlike helical ropes such as elevator and bridge cables, which are continuous strands with only a small and local effect of friction [43, 101]; in tissue, experimental observations demonstrate significant nonsymmetrical microscale sliding that mediates load transfer. The interfibrillar sliding, requires implementation of friction and contact, hence we used the finite element method for this problem over the classical wire rope theory [43].

There remains open questions regarding the physical existence and frequency of free fibril ends in mature tendon [166, 209] and our single sample only demonstrated one free end, however, it is important to note that experimental tensile data suggests there are “effective” free fibril ends that allow microscale sliding [213]. It is possible that fibril ends may exist in the form of tapered ends (such as Fig. 7.4A) or as physically weak links along the fibril length that can act as an “effective end” due to its high compliance [227]. Further investigations are required to explore these microstructures and their contribution to interfibrillar sliding and shear load transfer. Regardless of how the effective fibril ends occur, the experimental evidence of microscale sliding and shear load transfer supports our FE model based on friction and its inherent boundary condition assumption for free fibril ends.

In conclusion, we used SBF-SEM to visualize the three-dimensional microscale tendon structure of the fibrillar network, and used FE analysis to demonstrate that helically arranged fibrils can have the mechanical function of frictional interfibrillar load transfer. Our results showed novel microstructural configurations of collagen fibrils and cells in tendon and we showed that interfibrillar friction should be considered as another potential mechanism for interfibrillar load transfer, in addition to the previously postulated mechanisms of interfibrillar matrix shear and direct load transfer through

fibril junctions. This study shows that a combined approach of SBF-SEM imaging and FE modeling is a powerful tool to study structure-mechanics relationships in tendon microstructure.

Chapter 8

CONCLUSIONS AND POTENTIAL FUTURE DIRECTIONS

8.1 Conclusions

To comprehensively study and analyze the inelastic mechanical behaviors of tendon, a structurally-inspired framework was presented based on the kinetics of molecular bonds that break and reform in response to mechanical loading (Aim 1 Chapter 4). This modeling framework addresses viscoelasticity, plastic deformation, and damage of a fibrous structure based on three types of molecular bonds: formative, permanent, and sliding. These bond types each represent a mechanical behavior; formative bonds for viscoelasticity, permanent bonds for hyperelastic behavior, and sliding bonds for plastic deformation. As a general concept, damage was included in the modeling framework by reducing the number fraction of bonds. Damage is applied to each bond type separately, and it results in decreasing the ability of material to absorb energy. All of the aforementioned inelastic behaviors are modeled within the same constitutive setting and by using similar sets of constitutive equations. This Reactive Inelasticity is a structurally-inspired continuum mechanics theoretical framework and it uses observable state variables that are physically observable. Hence, the notion of inelastic mechanical behavior is well adapted to be applied to experimental data and to study and analyze mechanical behaviors in a physiological context.

Further, to evaluate tendon's inelastic mechanical response, the RIE was applied to the experimental micromechanical tests on tendon (Aim 2 Chapter 5). In this aim, the inelastic behaviors in tendon were investigated without a prior assumption about the softening mechanism in tendon to be either damage or plastic deformation. The models demonstrated excellent ability to fit the complex experiments, including stress-relaxation and softening phases of mechanical experiments, and provided numerical

values for inelastic effects on tendon. Despite their overall success in describing the inelastic mechanical behavior, the plastic model had slightly superior performance at the unloading phase, and the damage model had better predictions of the independent validation data set. These results indicate that the deformation-driven experiments are not suitable for distinguishing plastic deformation and damage.

Although the RIE-based inelasticity modeling provided excellent fits to the experimental data, still there is a central unanswered question in the viscoelastic mechanical response of tendon. It is not yet known if fluid flow poroelasticity, or solid matrix viscoelasticity are the mechanisms for tendon's viscoelastic behaviors. The Chapter 6 (Aim 3) was focused on calculating tendon's poroelastic parameters, particularly hydraulic permeability, by using osmotic loading and biphasic finite element modeling. Osmotic loading minimizes the effect of axial fibers on the lateral mechanical response, hence it isolates poroelastic response from solid matrix viscoelasticity. This study also demonstrated that tendon has tension-compression nonlinearity in the lateral direction. Although this study did not directly address the question of duality of poroelasticity and solid matrix as mechanisms of viscoelasticity, it provides a foundation for analysis of the mechanisms of viscoelasticity when the tissue is submitted to physiological axial loading.

In Chapter 7 (Aim 4) tendon's structure-mechanics relations were studied. We used serial block-face scanning electron microscopy (SBF-SEM) to visualize the microscale structures of tendon in 3D that showed many interesting structural features. Particularly, we reported groups of helical fibrils that can mechanically interact with each other. We provided a model for load-transfer between helical fibrils, which showed that the frictional interfibrillar load transfer is possible without a need for intermediating matrix. Thus, frictional contact should be considered as a potential mechanism for interfibrillar load transfer, in addition to the previously postulated mechanisms of interfibrillar matrix shear and direct load transfer through fibrillar junctions. This study demonstrated that three-dimensional microstructural imaging with SBF-SEM and FE modeling is a powerful tool to study structure-mechanics relationships in tendon.

This dissertation addressed several aspects of analysis and modeling of inelasticity in tendon, which included theoretical modeling, state-of-the-art experimental analysis, computational model parameter identification, and three-dimensional electron microscopy. In the light of the analysis provided in this dissertation, I believe that the working cycle of theoretical modeling, mechanical experiments, numerical analysis, and structural imaging is a powerful practice to effectively understand the complex mechanical behaviors of tissue. However, this work is only a prelude to many opportunities for the investigations that shall be pursued in the future.

8.2 Future Work

In the following, I provide the potential directions that could be taken to continue the research on the analysis and modeling of inelasticity in tendon (and in general fibrous tissue) mechanics. In fact, the opportunities are unlimited, and here, I only focused on the ones with potential wide range of interest in the field of tendon and tissue mechanics research. For each direction, when possible, I have provided three judicial steps, with a short-term (up to one year), medium-term (up to five years), and long-term (longer than five years) investment period, based on a conventional graduate-level research program. For some projects which would require more exploratory and preliminary studies, a distinction between medium- and long-term was not clear, so they were presented together.

8.2.1 Force-controlled mechanical experiments for studying inelasticity

Deformation-controlled boundary loading is the most common method for loading tissue in mechanical experiments, which in combination with structural imaging has provided valuable information about mechanisms of mechanical response in tendon [120,216]. However, it appears that the force-controlled mode of loading is less explored. The results of Aim 2 of this dissertation (Chapter 5) showed that the damage and plastic deformation behaviors are equally capable of explaining the deformation-driven mechanical tests. However, a force-controlled test can be utilized to directly

measure plastic deformation. Several other peculiar mechanical behaviors also arise during force-controlled tests, such as structural discrete plasticity during creep loading [86]. The author believes that force-controlled tests are highly fruitful for studying inelastic mechanical behaviors of tendon. Hence, an important short-term future direction would be to optimize the already available confocal imaging and micro-mechanical testing systems for force-controlled testing, and study the effect of such loading modality on the structural mechanisms of tendon mechanics, similar to the previous studies [120, 216]. A particularly curious question is that if the sustained-deformation or sustained-force loading would cause the tissue to undergo permanent inelastic changes (medium- and long-term), which perhaps would be in terms of accumulation of nonrecoverable sliding [120] that may be answered in light of force-controlled micro-mechanical tests.

8.2.2 Using molecular monitoring with inelasticity modeling for understanding mechanical behaviors of tissue

The quasi-static and dynamic mechanical properties of tissue are dependent on the molecular structure and factors affecting it, such as hydration, collagen denaturation, and cross-linking. In the light of advancements in the field, we can study the effect of hydration of collagen molecular configurations [138], and we are capable of measuring spatial distribution of denatured collagen with the use of collagen hybridizing peptides (CHP) [249]. Several studies also confirm that cross-linking can dramatically alter tissue's mechanical response [47, 204]. However, these techniques rely on complex procedures that are not suitable to capture the dynamic changes that can occur during mechanical loading of tissue.

One alternative direction is to utilize online molecular monitoring techniques such as Raman spectroscopy with mechanical loading to track the dynamic changes to the molecular configuration of tissue in response to loading. Some studies have shown the potential of Raman spectroscopy for visualizing such alterations during stress-relaxation that can identify changes to molecular interactions and water content

[56,81,155], however, the implications are not fully explored. For studying the dynamic changes to the molecular configurations in tendon, a hybrid test system with capability of doing Raman Spectroscopy and micro-mechanical testing at the same time can be highly instrumental in achieving this goal. Due to precedence of similar systems, but with other modality of imaging (e.g., confocal microscopy [216]), it is reasonable to assume that in short-term, such a system can be designed and built to collect proof-of-the-concept results with simple mechanical tests, and in mid-term more complex loading modalities can be utilized and cross-checked with the other molecular assays published in the literature. This effort would be an addition to the currently existing technology to track the dynamic of the tissue structure during mechanical loading, and hence in the long-term, to fully explore the multi-scale mechanics of tissue, imaging modalities such as confocal microscopy, and second harmonic generation (SHG) can be combined with Raman spectroscopy to study the molecular state of the tissue in the context of the higher length scale loading during mechanical stimulation.

8.2.3 Using inelasticity modeling and analysis in clinical studies

This dissertation did not directly focus on a clinical approach for understanding the tendon tissue and its disease, however, its findings and approaches open several directions for future clinical studies on tendon. One of the ultimate aims of studying the inelastic behaviors in tissue is to understand damage and failure. Damage and failure are important aspects of developing clinical conditions of tendon rupture and tendinopathy. By understanding the mechanisms of inelasticity in tissue, one can better understand the causes and factors involved in developing the pathological conditions. Specifically, the chronic tendinopathy is developed when a “healthy” regime of loading is not maintained on the tendon, where excessive loading causes disease, but a lack of loading also would be harmful to the tissue [38]. This is likely to be affected by the mechanical characteristics of the cellular environment and matrix mechanics [119]. Hence, based on the approach of inelasticity analysis, the mechanical factors of the

tissue can be evaluated by studying the tendinopathic human tissue. By using structural imaging, such as elastography [42], and reactive inelastic mechanical modeling (Chapter 4) (medium- and long-term) one can study the mechanical properties of the tissue at different stages of disease, injury and healing. The outcomes of this study can provide mechanical parameters beyond the traditional values of elastic moduli, and based on RIE modeling, the onsets of inelasticity and progression of inelasticity can be measured (Chapter 5) providing a more precise view of the mechanical state of the tissue and its susceptibility to further injury and its progress in healing.

8.2.4 Generalized framework for model parameter identification and identifiability of inelastic properties

Due to complex mechanical behaviors of tissue, often mathematical models with many parameters are used. Hence, to calibrate the parameters that best resemble the tissue behavior, *model parameter identification* is used. Model parameter identification, or parameter identification, is done by manual calibration or systematic optimization. Due to the highly nonlinear behavior of tissue, manual calibration, although in some cases practical, is very limited in providing parameters that can be guaranteed to be repeatable, unique, and accurate, which signifies the role of optimization in parameter identification. However, the common use of optimization techniques also come with serious limitations. As an instance, the popular method of *nonlinear least squares*, the most common technique for parameter identification in tissue mechanics, are prone to issues, including *local minima* and *non-uniqueness* of the solutions [111]. Several alternative methods have been used to overcome these difficulties, such as *global optimization* algorithms such as genetic algorithm, particle swarm, simulated annealing, etc [190, 210, 226]. However, even these techniques and promises of a global minima can be misleading when adequate considerations for the type of experimental data and modeling steps are not taking into account [82].

One crucial step to remedy for this issue is to make sure given that the experimental data and the applied model are compatible that the model parameters of

interest are identifiable. One simple, yet important, example is that one cannot find both Young's modulus and Poisson's ratio (or equivalently the combination of bulk modulus and shear modulus) only from the stress-strain curve of a uniaxial tests [82]. Even the best optimization method would not be able to give a unique solution for modulus and Poisson's ratio from only stress-strain response from a uniaxial test, because there is an infinite combination of them that can be THE solution. This is a classic example of the problem of *identifiability*, which needs to be addressed when conducting model parameter identification such as nonlinear least squares or global optimization.

In this dissertation, a primary focus was to isolate the mechanisms with overlapping effects that is in a sense addressing the problem of identifiability. We provided remedies by using distinct structurally-based models Chapters 4 and 5 and multi-start nonlinear least squares optimization Chapters 5 and 6. However, this is only the beginning, and due the complex inelasticity and nonlinearity of tissue response, further studies need to be done. A possible future direction is, in short-term, to conduct identifiability studies to investigate the dependence of the material parameters with standard mechanical tests such as uniaxial and biaxial tension, confined and unconfined compression, and indentation on different tissue systems. This can be achieved by conducting multi-start optimization of theoretically generated data with known model parameters of inelastic mechanical models. Further, in medium-term a theoretical basis is needed to effectively interpret the findings of multi-start optimization experiments and formalizing the procedure for model parameter identification, especially methods for analyzing high-dimensional fit results, and efficient sampling of the n-dimensional search space. In long-term, these efforts should be continued and communicated with the field, and potentially to be a focus in technical sessions and workshops at national and international conferences, with the ultimate aim of coming up with consensus among the field of tissue mechanics for appropriate practices in model parameter identification.

8.2.5 Efficient analysis of 3D micro-structure using SBF-SEM for studying structure-mechanics

In Chapter 7, we used SBF-SEM to visualize the 3D structure of tendon. However, the procedure for analyzing and segmentation of the SBF-SEM data is time consuming and difficult. However, the 3D information from the microstructure needs to be explored in greater detail and yet there are many unanswered questions. Hence, there is a need for more efficient analysis techniques. A possibility would be to use the already established Fourier transformation (FT) techniques that are common for measuring fibrillar alignment in 2D [74, 116] by generalizing it to 3D. In short-term, the generalized three-dimensional FT can be applied to computationally generated idealized structures as proof of concept. In medium- and long-term, analysis of real SBF-SEM data is possible, which would require utilization of filtration of SBF-SEM images, and use of efficient computational algorithms, likely with cluster computers. A computationally valid method then can be applied not only to SBF-SEM data, but it also may be applied to data from higher length-scales, the fiber scale, based on second harmonic generation (SHG) and multi-photon imaging [87, 179], enabling multiscale analysis of structure organization of the hierarchical fibrous structure of tissue.

8.3 Summary

In summary, in this dissertation I provided a basis for analysis and modeling the inelastic behaviors of tendon that include viscoelasticity, damage, and plastic deformation. The theoretical framework for analyzing tissue inelasticity was provided based on kinetics of molecular bonds, and it was used to interpret the mechanisms of inelasticity in experimental micro-mechanical tests on rat tail tendon. I also focused on isolating the poroelastic mechanical behavior of tendon from intrinsic viscoelasticity, and in the pursuit of that aim I provided osmotic loading experimental data, and a finite element model that provided tendon's poroelastic parameter, particularly the hydraulic permeability of tendon. The structural mechanisms of mechanical behaviors of tendon were also investigated by using three-dimensional microstructure of tendon

that found many helical structures, and I also provided a load-transfer model based on the contact between the collagen fibrils as a potential mechanism for load transfer. The most important outcome of this dissertation is that the analysis and modeling of tendon, and soft tissue in general, is far from being done, however, in the light modern tools for theoretical, computation and experimental analysis we are well poised to better advance the fundamental understanding about the mechanical behaviors of biological tissue.

BIBLIOGRAPHY

- [1] M. Abrahams. Mechanical behaviour of tendon In vitro - A preliminary report. *Med. Biol. Eng.*, 5(5):433–443, 1967.
- [2] H. Ahmadzadeh, B. K. Connizzo, B. R. Freedman, L. J. Soslowsky, and V. B. Shenoy. Determining the contribution of glycosaminoglycans to tendon mechanical properties with a modified shear-lag model. *J. Biomech.*, 46(14):2497–503, sep 2013.
- [3] V. Alastrué, E. Peña, M. A. Martínez, and M. Doblaré. Experimental study and constitutive modelling of the passive mechanical properties of the ovine infrarenal vena cava tissue. *J. Biomech.*, 41(14):3038–3045, oct 2008.
- [4] V. Alastrué, J. Rodríguez, B. Calvo, and M. Doblaré. Structural damage models for fibrous biological soft tissues. *Int. J. Solids Struct.*, 44(18-19):5894–5911, sep 2007.
- [5] N. Andarawis-Puri and E. L. Flatow. Tendon fatigue in response to mechanical loading. *J. Musculoskelet. Neuronal Interact.*, 11(2):106–14, jun 2011.
- [6] R. D. Andrews, A. V. Tobolsky, and E. E. Hanson. The Theory of Permanent Set at Elevated Temperatures in Natural and Synthetic Rubber Vulcanizates. *J. Appl. Phys.*, 17(5):352–361, may 1946.
- [7] N. Aravas. Finite-strain anisotropic plasticity and the plastic spin. *Model. Simul. Mater. Sci. Eng.*, 2(3 A):483–504, 1994.
- [8] G. A. Ateshian. On the theory of reactive mixtures for modeling biological growth. *Biomech. Model. Mechanobiol.*, 6(6):423–445, oct 2007.
- [9] G. A. Ateshian. The role of mass balance equations in growth mechanics illustrated in surface and volume dissolutions. *J. Biomech. Eng.*, 133(1):11010, jan 2011.
- [10] G. A. Ateshian. Viscoelasticity using reactive constrained solid mixtures. *J. Biomech.*, 48(6):941–947, apr 2015.
- [11] G. A. Ateshian and J. D. Humphrey. Continuum mixture models of biological growth and remodeling: past successes and future opportunities. *Annu. Rev. Biomed. Eng.*, 14:97–111, 2012.

- [12] G. A. Ateshian and T. Ricken. Multigenerational interstitial growth of biological tissues. *Biomech. Model. Mechanobiol.*, 9(6):689–702, dec 2010.
- [13] G. A. Ateshian, W. H. Warden, J. J. Kim, R. P. Grelsamer, and V. C. Mow. Finite deformation biphasic material properties of bovine articular cartilage from confined compression experiments. *J. Biomech.*, 30(11-12):1157–1164, 1997.
- [14] G. A. Ateshian and J. A. Weiss. Anisotropic Hydraulic Permeability Under Finite Deformation. *J. Biomech. Eng.*, 132(11):111004, nov 2010.
- [15] B. Babaei, A. J. Velasquez-Mao, S. Thomopoulos, E. L. Elson, S. D. Abramowitch, and G. M. Genin. Discrete quasi-linear viscoelastic damping analysis of connective tissues, and the biomechanics of stretching. *J. Mech. Behav. Biomed. Mater.*, 69:193–202, may 2017.
- [16] D. Balzani, S. Brinkhues, and G. Holzapfel. Constitutive framework for the modeling of damage in collagenous soft tissues with application to arterial walls. *Comput. Methods Appl. Mech. Eng.*, 213-216:139–151, mar 2012.
- [17] E. Ban, V. H. Barocas, M. S. Shephard, and C. R. Picu. Softening in Random Networks of Non-Identical Beams. *J. Mech. Phys. Solids*, 87:38–50, feb 2016.
- [18] G. Baril and B. K. Issenman. *Sinews of Survival: The Living Legacy of Inuit Clothing*, volume 40. UBC Press, 2010.
- [19] E. Bass. Tendinopathy: why the difference between tendinitis and tendinosis matters. *Int. J. Ther. Massage Bodywork*, 5(1):14–7, jan 2012.
- [20] B. Bhushan. *Handbook of micro/nanotribology*. CRC Press, 1999.
- [21] M. Böl, A. E. Ehret, K. Leichsenring, and M. Ernst. Tissue-scale anisotropy and compressibility of tendon in semi-confined compression tests. *J. Biomech.*, 48(6):1092–8, apr 2015.
- [22] J. Bonet and R. D. Wood. *Nonlinear Continuum Mechanics for Finite Element Analysis*. Cambridge University Press, 1997.
- [23] L. Bozec, G. van der Heijden, and M. Horton. Collagen fibrils: nanoscale ropes. *Biophys. J.*, 92(1):70–5, jan 2007.
- [24] K. A. Buchanan, R. S. Lakes, and R. Vanderby. Chiral behavior in rat tail tendon fascicles. *J. Biomech.*, 64:206–211, nov 2017.
- [25] B. W. Bussewitz. Repair of Neglected Achilles Rupture, apr 2017.
- [26] T. A. Carniel, B. Klahr, and E. A. Fancello. On multiscale boundary conditions in the computational homogenization of an RVE of tendon fascicles. *J. Mech. Behav. Biomed. Mater.*, 91:131–138, mar 2019.

- [27] A. Caro-Bretelle, P. Gountsop, P. Ienny, R. Leger, S. Corn, I. Bazin, and F. Bretelle. Effect of sample preservation on stress softening and permanent set of porcine skin. *J. Biomech.*, 48(12):3135–3141, 2015.
- [28] J. L. Chaboche. Continuum damage mechanics: Present state and future trends. *Nucl. Eng. Des.*, 105(1):19–33, dec 1987.
- [29] N. O. Chahine, F. H. Chen, C. T. Hung, and G. A. Ateshian. Direct measurement of osmotic pressure of glycosaminoglycan solutions by membrane osmometry at room temperature. *Biophys. J.*, 89(3):1543–50, sep 2005.
- [30] S.-W. Chang and M. J. Buehler. Molecular biomechanics of collagen molecules. *Mater. Today*, 17(2):70–76, mar 2014.
- [31] B. M. Chu and P. J. Blatz. Cumulative microdamage model to describe the hysteresis of living tissue. *Ann. Biomed. Eng.*, 1(2):204–211, dec 1972.
- [32] K. H. Chung, A. K. Chen, C. R. Anderton, K. Bhadriraju, A. L. Plant, B. G. Bush, R. F. Cook, and F. W. Delrio. Frictional properties of native and functionalized type i collagen thin films. *Appl. Phys. Lett.*, 103(14):143703, sep 2013.
- [33] J. M. Cloyd, N. R. Malhotra, L. Weng, W. Chen, R. L. Mauck, and D. M. Elliott. Material properties in unconfined compression of human nucleus pulposus, injectable hyaluronic acid-based hydrogels and tissue engineering scaffolds. *Eur. spine J. Off. Publ. Eur. Spine Soc. Eur. Spinal Deform. Soc. Eur. Sect. Cerv. Spine Res. Soc.*, 16(11):1892–1898, nov 2007.
- [34] B. D. Coleman and M. E. Gurtin. Thermodynamics with Internal State Variables. *J. Chem. Phys.*, 47(2):597–613, jul 1967.
- [35] B. K. Connizzo and A. J. Grodzinsky. Tendon exhibits complex poroelastic behavior at the nanoscale as revealed by high-frequency AFM-based rheology. *J. Biomech.*, 54:11–18, mar 2017.
- [36] B. K. Connizzo and A. J. Grodzinsky. Tendon exhibits complex poroelastic behavior at the nanoscale as revealed by high-frequency AFM-based rheology. *J. Biomech.*, 54:11–18, 2017.
- [37] J. L. Cook and C. R. Purdam. Is tendon pathology a continuum? A pathology model to explain the clinical presentation of load-induced tendinopathy. *Br. J. Sports Med.*, 43:409–416, 2009.
- [38] J. L. Cook, E. Rio, C. R. Purdam, and S. I. Docking. Revisiting the continuum model of tendon pathology: What is its merit in clinical practice and research? *Br. J. Sports Med.*, 50(19):1187–1191, oct 2016.

- [39] J. Cornillie, T. van Cann, A. Wozniak, D. Hompes, and P. Schöffski. Biology and management of clear cell sarcoma: state of the art and future perspectives, aug 2016.
- [40] D. H. Cortes and D. M. Elliott. Accurate prediction of stress in fibers with distributed orientations using generalized high-order structure tensors. *Mech. Mater.*, 75:73–83, aug 2014.
- [41] D. H. Cortes, N. T. Jacobs, J. F. DeLucca, and D. M. Elliott. Elastic, permeability and swelling properties of human intervertebral disc tissues: A benchmark for tissue engineering. *J. Biomech.*, 47(9):2088–2094, jun 2014.
- [42] D. H. Cortes, S. M. Suydam, K. G. Silbernagel, T. S. Buchanan, and D. M. Elliott. Continuous Shear Wave Elastography: A New Method to Measure Viscoelastic Properties of Tendons in Vivo. *Ultrasound Med. Biol.*, 41(6):1518–1529, jun 2015.
- [43] G. A. Costello. *Theory of Wire Rope*. Mechanical Engineering Series. Springer New York, New York, NY, 1997.
- [44] Y. F. Dafalias. The plastic spin in viscoplasticity. *Int. J. Solids Struct.*, 26(2):149–163, dec 1990.
- [45] B. De Campos Vidal. Image analysis of tendon helical superstructure using interference and polarized light microscopy. *Micron*, 34(8):423–432, dec 2003.
- [46] H. Demirkoparan, T. J. Pence, and A. Wineman. On dissolution and reassembly of filamentary reinforcing networks in hyperelastic materials. *Proc. R. Soc. A Math. Phys. Eng. Sci.*, 465(2103):867–894, mar 2009.
- [47] B. Depalle, Z. Qin, S. J. Shefelbine, and M. J. Buehler. Influence of cross-link structure, density and mechanical properties in the mesoscale deformation mechanisms of collagen fibrils. *J. Mech. Behav. Biomed. Mater.*, 52:1–13, 2015.
- [48] J. Diani, B. Fayolle, and P. Gilormini. A review on the Mullins effect, mar 2009.
- [49] Dictionary.com. Tendon, 2019.
- [50] R. Dittmar, M. M. Van Rijsbergen, and K. Ito. Moderately Degenerated Human Intervertebral Disks Exhibit a Less Geometrically Specific Collagen Fiber Orientation Distribution. *Glob. Spine J.*, 6(5):439–446, aug 2016.
- [51] A. Dorfmann and R. Ogden. A constitutive model for the Mullins effect with permanent set in particle-reinforced rubber. *Int. J. Solids Struct.*, 41(7):1855–1878, apr 2004.

- [52] S. E. Duenwald, R. J. Vanderby, and R. S. Lakes. Stress relaxation and recovery in tendon and ligament: Experiment and modeling. *Biorheology*, 47(1):1–14, 2010.
- [53] S. Duenwald-Kuehl, J. Kondratko, R. S. Lakes, and R. J. Vanderby. Damage mechanics of porcine flexor tendon: mechanical evaluation and modeling. *Ann. Biomed. Eng.*, 40(8):1692–1707, aug 2012.
- [54] S. Duenwald-Kuehl, R. Lakes, and R. J. Vanderby. Strain-induced damage reduces echo intensity changes in tendon during loading. *J. Biomech.*, 45(9):1607–1611, jun 2012.
- [55] A. E. Ehret, K. Bircher, A. Stracuzzi, V. Marina, M. Zündel, and E. Mazza. Inverse poroelasticity as a fundamental mechanism in biomechanics and mechanobiology. *Nat. Commun.*, 8(1), 2017.
- [56] K. Esmonde-White. Raman Spectroscopy of Soft Musculoskeletal Tissues. *Appl. Spectrosc.*, 68(11):1203–1218, nov 2014.
- [57] D. R. Eyre, M. A. Weis, and J.-J. Wu. Advances in collagen cross-link analysis. *Methods*, 45(1):65–74, may 2008.
- [58] F. Fang and S. P. Lake. Multiscale mechanical integrity of human supraspinatus tendon in shear after elastin depletion. *J. Mech. Behav. Biomed. Mater.*, 63:443–455, oct 2016.
- [59] S. A. Fenwick, B. L. Hazleman, and G. P. Riley. The vasculature and its role in the damaged and healing tendon. *Arthritis Res.*, 4(4):252–260, 2002.
- [60] B. Fereidoonzehad, R. Naghdabadi, and G. Holzapfel. Stress softening and permanent deformation in human aortas: Continuum and computational modeling with application to arterial clamping. *J. Mech. Behav. Biomed. Mater.*, 61:600–616, aug 2016.
- [61] G. Fessel and J. G. Snedeker. Evidence against proteoglycan mediated collagen fibril load transmission and dynamic viscoelasticity in tendon. *Matrix Biol.*, 28(8):503–10, oct 2009.
- [62] J. L. Finstein, S. B. Cohen, C. C. Dodson, M. G. Ciccotti, P. Marchetto, M. D. Pepe, and P. F. Deluca. Triceps tendon ruptures requiring surgical repair in national football league players. *Orthop. J. Sport. Med.*, 3(8):232596711560102, aug 2015.
- [63] R. Flaherty. Scene from Nanook of the North, 1922.
- [64] B. C. Fleming, M. J. Hulstyn, H. L. Oksendahl, and P. D. Fadale. Ligament injury, reconstruction and osteoarthritis, oct 2005.

- [65] W. Folkhard, D. Christmann, W. Geercken, E. Knörzer, M. H. J. Koch, E. Mosler, H. Nemetschek-Gansler, and T. Nemetschek. Twisted Fibrils are a Structural Principle in the Assembly of Interstitial Collagens, Chordae Tendineae Included. *Zeitschrift für Naturforsch. C*, 42(11-12):1303–1306, dec 1987.
- [66] M. T. Fondrk, E. H. Bahniuk, and D. T. Davy. A damage model for nonlinear tensile behavior of cortical bone. *J. Biomech. Eng.*, 121(5):533–41, oct 1999.
- [67] M. Franchi, V. Ottani, R. Stagni, and A. Ruggeri. Tendon and ligament fibrillar crimps give rise to left-handed helices of collagen fibrils in both planar and helical crimps. *J. Anat.*, 216(3):301–309, mar 2010.
- [68] B. R. Freedman, J. A. Gordon, and L. J. Soslowsky. The Achilles tendon: fundamental properties and mechanisms governing healing. *Muscles. Ligaments Tendons J.*, 4(2):245–55, apr 2014.
- [69] Y.-C. Fung. *Biomechanics*. Springer New York, New York, NY, 1993.
- [70] P. Garnero. The contribution of collagen crosslinks to bone strength. *Bonekey Rep.*, 1:182, sep 2012.
- [71] A. Gautieri, S. Vesentini, A. Redaelli, and M. J. Buehler. Hierarchical structure and nanomechanics of collagen microfibrils from the atomistic scale up. *Nano Lett.*, 11(2):757–766, feb 2011.
- [72] R. H. Gelberman. Flexor tendon physiology: tendon nutrition and cellular activity in injury and repair. *Instr. Course Lect.*, 34:351–360, 1985.
- [73] M. S. Green and A. V. Tobolsky. A New Approach to the Theory of Relaxing Polymeric Media. *J. Chem. Phys.*, 14(2):80–92, feb 1946.
- [74] H. A. L. Guerin and D. M. Elliott. Degeneration affects the fiber reorientation of human annulus fibrosus under tensile load. *J. Biomech.*, 39(8):1410–1418, jan 2006.
- [75] Z. Guo and R. De Vita. Probabilistic constitutive law for damage in ligaments. *Med. Eng. Phys.*, 31(9):1104–1109, nov 2009.
- [76] M. F. Hadi and V. H. Barocas. Microscale Fiber Network Alignment Affects Macroscale Failure Behavior in Simulated Collagen Tissue Analogs. *J. Biomech. Eng.*, 135(2):021026, feb 2013.
- [77] M. F. Hadi, E. A. Sander, and V. H. Barocas. Multiscale Model Predicts Tissue-Level Failure From Collagen Fiber-Level Damage. *J. Biomech. Eng.*, 134(9):091005, sep 2012.

- [78] W. M. Han, N. L. Nerurkar, L. J. Smith, N. T. Jacobs, R. L. Mauck, and D. M. Elliott. Multi-scale structural and tensile mechanical response of annulus fibrosus to osmotic loading. *Ann. Biomed. Eng.*, 40(7):1610–21, jul 2012.
- [79] J. A. Hannafin and S. P. Arnoczky. Effect of cyclic and static tensile loading on water content and solute diffusion in canine flexor tendons: an in vitro study. *J. Orthop. Res.*, 12(3):350–6, may 1994.
- [80] K. A. Hansen, J. A. Weiss, and J. K. Barton. Recruitment of Tendon Crimp With Applied Tensile Strain. *J. Biomech. Eng.*, 124(1):72, 2002.
- [81] J. Hanuza, M. Maczka, M. Gasior-Glogowska, M. Komorowska, M. Kobielarz, R. Bedzinski, S. Szotek, K. Maksymowicz, and K. Hermanowicz. FT-Raman spectroscopic study of thoracic aortic wall subjected to uniaxial stress. *J. Raman Spectrosc.*, 41(10):1163–1169, oct 2010.
- [82] S. Hartmann and R. R. Gilbert. Identifiability of material parameters in solid mechanics. *Arch. Appl. Mech.*, 88(1-2):3–26, feb 2018.
- [83] T. Hashimoto, G. E. Thompson, X. Zhou, and P. J. Withers. 3D imaging by serial block face scanning electron microscopy for materials science using ultramicrotomy. *Ultramicroscopy*, 163:6–18, apr 2016.
- [84] H. B. Henninger, C. J. Underwood, G. A. Ateshian, and J. A. Weiss. Effect of sulfated glycosaminoglycan digestion on the transverse permeability of medial collateral ligament. *J. Biomech.*, 43(13):2567–2573, sep 2010.
- [85] H. B. Henninger, W. R. Valdez, S. A. Scott, and J. A. Weiss. Elastin governs the mechanical response of medial collateral ligament under shear and transverse tensile loading. *Acta Biomater.*, 25:304–312, oct 2015.
- [86] T. W. Herod, N. C. Chambers, and S. P. Veres. Collagen fibrils in functionally distinct tendons have differing structural responses to tendon rupture and fatigue loading. *Acta Biomater.*, 42:296–307, sep 2016.
- [87] M. R. Hill, X. Duan, G. A. Gibson, S. Watkins, and A. M. Robertson. A theoretical and non-destructive experimental approach for direct inclusion of measured collagen orientation and recruitment into mechanical models of the artery wall. *J. Biomech.*, 45(5):762–771, 2012.
- [88] M. H. Holmes and V. C. Mow. The nonlinear characteristics of soft gels and hydrated connective tissues in ultrafiltration. *J. Biomech.*, 23(11):1145–1156, 1990.
- [89] G. Holzapfel. *Nonlinear Solid Mechanics: A Continuum Approach for Engineering*. 2000.

- [90] G. A. Holzapfel and J. C. Simo. A new viscoelastic constitutive model for continuous media at finite thermomechanical changes. *Int. J. Solids Struct.*, 33(20-22):3019–3034, aug 1996.
- [91] M. F. Horstemeyer and D. J. Bammann. Historical review of internal state variable theory for inelasticity. *Int. J. Plast.*, 26(9):1310–1334, sep 2010.
- [92] S. Hosseini, W. Wilson, K. Ito, and C. van Donkelaar. A numerical model to study mechanically induced initiation and progression of damage in articular cartilage. *Osteoarthr. Cartil.*, 22(1):95–103, jan 2014.
- [93] C. Y. Huang, V. C. Mow, and G. A. Ateshian. The role of flow-independent viscoelasticity in the biphasic tensile and compressive responses of articular cartilage. *J. Biomech. Eng.*, 123(5):410–417, oct 2001.
- [94] C.-Y. Huang, A. Stankiewicz, G. A. Ateshian, and V. C. Mow. Anisotropy, inhomogeneity, and tension-compression nonlinearity of human glenohumeral cartilage in finite deformation. *J. Biomech.*, 38(4):799–809, apr 2005.
- [95] D. J. Hulmes. Building Collagen Molecules, Fibrils, and Suprafibrillar Structures. *J. Struct. Biol.*, 137(1-2):2–10, jan 2002.
- [96] H. Huntley, A. Wineman, and K. Rajagopal. Stress softening, strain localization and permanent set in the circumferential shear of an incompressible elastomeric cylinder. *IMA J. Appl. Math. (Institute Math. Its Appl.)*, 59(3):309–338, dec 1997.
- [97] J. Huyghe and J. Janssen. Quadriphasic mechanics of swelling incompressible porous media. *Int. J. Eng. Sci.*, 35(8):793–802, jun 1997.
- [98] J. C. Iatridis, L. A. Setton, R. J. Foster, B. A. Rawlins, M. Weidenbaum, and V. C. Mow. Degeneration affects the anisotropic and nonlinear behaviors of human annulus fibrosus in compression. *J. Biomech.*, 31(6):535–544, jun 1998.
- [99] J. C. Iatridis, J. Wu, J. a. Yandow, and H. M. Langevin. Subcutaneous tissue mechanical a is linear and viscoelastic under uniaxial tension. *Connect. Tissue Res.*, 44(5):208–217, 2003.
- [100] N. T. Jacobs, D. H. Cortes, J. M. Peloquin, E. J. Vresilovic, and D. M. Elliott. Validation and application of an intervertebral disc finite element model utilizing independently constructed tissue-level constitutive formulations that are nonlinear, anisotropic, and time-dependent. *J. Biomech.*, 47(11):2540–2546, aug 2014.
- [101] W. Jiang, M. Yao, and J. Walton. A concise finite element model for simple straight wire rope strand. *Int. J. Mech. Sci.*, 41(2):143–161, feb 1999.
- [102] J. Johansson and C. Forsell. Evaluation of Parallel Coordinates: Overview, Categorization and Guidelines for Future Research. *IEEE Trans. Vis. Comput. Graph.*, 22(1):579–588, jan 2016.

- [103] Józsa, László G. and P. Kannus. *Human tendons: anatomy, physiology, and pathology*. Human Kinetics Publishers, 1997.
- [104] J. W. Ju. Isotropic and Anisotropic Damage Variables in Continuum Damage Mechanics. *J. Eng. Mech.*, 116(12):2764–2770, dec 1990.
- [105] L. M. Kachanov. *Introduction to continuum damage mechanics*, volume 79. Springer Science & Business Media, 1986.
- [106] K. E. Kadler, D. F. Holmes, J. A. Trotter, and J. A. Chapman. H.5002_2111_0463805.Pdf. *Biochem. J.*, 11:1–11, 1996.
- [107] N. S. Kalson, Y. Lu, S. H. Taylor, T. Starborg, D. F. Holmes, and K. E. Kadler. A structure-based extracellular matrix expansion mechanism of fibrous tissue growth. *Elife*, 4, may 2015.
- [108] N. S. Kalson, P. S. Malone, R. S. Bradley, P. J. Withers, and V. C. Lees. Fibre bundles in the human extensor carpi ulnaris tendon are arranged in a spiral. *J. Hand Surg. Eur. Vol.*, 37(6):550–554, jul 2012.
- [109] P. Kannus. Structure of the tendon connective tissue. *Scand. J. Med. Sci. Sport.*, 10(6):312–320, dec 2000.
- [110] J. Kastelic, A. Galeski, and E. Baer. The multicomposite structure of tendon. *Connect. Tissue Res.*, 6(1):11–23, jan 1978.
- [111] C. T. Kelley. *Iterative Methods for Optimization*. Society for Industrial and Applied Mathematics, jan 1999.
- [112] A. S. Khan and S. Huang. *Continuum theory of plasticity*. John Wiley & Sons, 1995.
- [113] D. Krajcinovic. Damage mechanics: accomplishments, trends and needs. *Int. J. Solids Struct.*, 37(1-2):267–277, jan 2000.
- [114] A. S. LaCroix, S. E. Duenwald-Kuehl, R. S. Lakes, and R. Vanderby. Relationship between tendon stiffness and failure: a metaanalysis. *J. Appl. Physiol.*, 115(1):43–51, jul 2013.
- [115] W. M. Lai, J. S. Hou, and V. C. Mow. A triphasic theory for the swelling and deformation behaviors of articular cartilage. *J. Biomech. Eng.*, 113(3):245–258, aug 1991.
- [116] S. P. Lake, K. S. Miller, D. M. Elliott, and L. J. Soslowsky. Tensile properties and fiber alignment of human supraspinatus tendon in the transverse direction demonstrate inhomogeneity, nonlinearity, and regional isotropy. *J. Biomech.*, 43(4):727–732, mar 2010.

- [117] R. S. Lakes and R. Vanderby. Interrelation of Creep and Relaxation: A Modeling Approach for Ligaments. *J. Biomech. Eng.*, 121(6):612, 1999.
- [118] N. S. Landinez-Parra, D. A. Garzón-Alvarado, and J. C. Vanegas-Acosta. A phenomenological mathematical model of the articular cartilage damage. *Comput. Methods Programs Biomed.*, 104(3):e58—74, dec 2011.
- [119] M. Lavagnino, M. E. Wall, D. Little, A. J. Banes, F. Guilak, and S. P. Arnoczky. Tendon mechanobiology: Current knowledge and future research opportunities. *J. Orthop. Res.*, 33(6):813–822, 2015.
- [120] A. H. Lee, S. E. Szczesny, M. H. Santare, and D. M. Elliott. Investigating mechanisms of tendon damage by measuring multi-scale recovery following tensile loading. *Acta Biomater.*, 57:363–372, jul 2017.
- [121] E. H. Lee. Elastic-Plastic Deformation at Finite Strains. *J. Appl. Mech.*, 36(1):1, 1969.
- [122] K. Legerlotz, G. P. Riley, and H. R. Screen. Specimen dimensions influence the measurement of material properties in tendon fascicles. *J. Biomech.*, 43(12):2274–2280, 2010.
- [123] J. Lemaitre. How to use damage mechanics. *Nucl. Eng. Des.*, 80(2):233–245, jul 1984.
- [124] M. A. LeRoux and L. A. Setton. Experimental and Biphasic FEM Determinations of the Material Properties and Hydraulic Permeability of the Meniscus in Tension. *J. Biomech. Eng.*, 124(3):315, 2002.
- [125] W. Li. Damage Models for Soft Tissues: A Survey. *J. Med. Biol. Eng.*, 36(3):285–307, jun 2016.
- [126] Y. Li and S. M. Yu. Targeting and mimicking collagens via triple helical peptide assembly. *Curr. Opin. Chem. Biol.*, 17(6):968–975, dec 2013.
- [127] J. H. Lillie, D. K. MacCallum, L. J. Scaletta, and J. C. Occhino. Collagen structure: Evidence for a helical organization of the collagen fibril. *J. Ultrastructure Res.*, 58(2):134–143, 1977.
- [128] Y. Liu, R. Ballarini, and S. J. Eppell. Tension tests on mammalian collagen fibrils. *Interface Focus*, 6(1):20150080, feb 2016.
- [129] V. A. Lubarda. Constitutive theories based on the multiplicative decomposition of deformation gradient: Thermoelasticity, elastoplasticity, and biomechanics. *Appl. Mech. Rev.*, 57(2):95, 2004.

- [130] T. J. Lujan, C. J. Underwood, N. T. Jacobs, and J. A. Weiss. Contribution of glycosaminoglycans to viscoelastic tensile behavior of human ligament. *J. Appl. Physiol.*, 106(2):423–31, feb 2009.
- [131] H. A. Lynch, W. Johannessen, J. P. Wu, A. Jawa, and D. M. Elliott. Effect of fiber orientation and strain rate on the nonlinear uniaxial tensile material properties of tendon. *J. Biomech. Eng.*, 125(5):726–731, oct 2003.
- [132] S. A. Maas, B. J. Ellis, G. A. Ateshian, and J. A. Weiss. FEBio: Finite Elements for Biomechanics. *J. Biomech. Eng.*, 134(1):011005, jan 2012.
- [133] C. N. Maganaris, P. Chatzistergos, N. D. Reeves, and M. V. Narici. Quantification of internal stress-strain fields in human tendon: Unraveling the mechanisms that underlie regional tendon adaptations and mal-adaptations to mechanical loading and the effectiveness of therapeutic eccentric exercise, 2017.
- [134] E. Maher, A. Creane, C. Lally, and D. J. Kelly. An anisotropic inelastic constitutive model to describe stress softening and permanent deformation in arterial tissue. *J. Mech. Behav. Biomed. Mater.*, 12:9–19, 2012.
- [135] A. Maiti, W. Small, R. H. Gee, T. H. Weisgraber, S. C. Chinn, T. S. Wilson, and R. S. Maxwell. Mullins effect in a filled elastomer under uniaxial tension. *Phys. Rev. E*, 89(1):012602, jan 2014.
- [136] Y. Mao, S. Lin, X. Zhao, and L. Anand. A large deformation viscoelastic model for double-network hydrogels. *J. Mech. Phys. Solids*, 100:103–130, mar 2017.
- [137] G. Marlena, M. Komorowska, J. Hanuza, M. Mirosław, B. Romuald, and M. Kobielarz. Mechanobiology of soft tissues : FT-Raman spectroscopic studies Biomedical Engineering. *Challenges Mod. Technol.*, Vol. 2, no:8–11, 2011.
- [138] A. Masic, L. Bertinetti, R. Schuetz, S.-W. Chang, T. H. Metzger, M. J. Buehler, and P. Fratzl. Osmotic pressure induced tensile forces in tendon collagen. *Nat. Commun.*, 6:5942, jan 2015.
- [139] F. Meng, R. H. Pritchard, and E. M. Terentjev. Stress Relaxation, Dynamics, and Plasticity of Transient Polymer Networks. *Macromolecules*, 49(7):2843–2852, apr 2016.
- [140] F. Meng and E. Terentjev. Transient Network at Large Deformations: ElasticPlastic Transition and Necking Instability. *Polymers (Basel)*., 8(4):108, mar 2016.
- [141] Merriam-Webster.com. Tendon, 2019.
- [142] M. Minary-Jolandan and M. F. Yu. Nanomechanical heterogeneity in the gap and overlap regions of type I collagen fibrils with implications for bone heterogeneity. *Biomacromolecules*, 10(9):2565–2570, 2009.

- [143] V. C. Mow, S. C. Kuei, W. M. Lai, and C. G. Armstrong. Biphasic creep and stress relaxation of articular cartilage in compression? Theory and experiments. *J. Biomech. Eng.*, 102(1):73–84, feb 1980.
- [144] A. Muliana, K. R. Rajagopal, D. Tscharnuter, and G. Pinter. A nonlinear viscoelastic constitutive model for polymeric solids based on multiple natural configuration theory. *Int. J. Solids Struct.*, 100-101:95–110, dec 2016.
- [145] L. Mullins. Softening of Rubber by Deformation. *Rubber Chem. Technol.*, 42(1):339–362, mar 1969.
- [146] S. Murakami. *Continuum Damage Mechanics*, volume 185 of *Solid Mechanics and Its Applications*. Springer Netherlands, Dordrecht, 2012.
- [147] P. Naghdi and J. Trapp. The significance of formulating plasticity theory with reference to loading surfaces in strain space. *Int. J. Eng. Sci.*, 13(9-10):785–797, sep 1975.
- [148] C. Napaumpaiporn and W. Katchamart. Clinical manifestations and outcomes of musculoskeletal nontuberculous mycobacterial infections. *Rheumatol. Int.*, pages 1–5, jul 2019.
- [149] A. Natali, P. Pavan, E. Carniel, M. Lucisano, and G. Tagliavero. Anisotropic elasto-damage constitutive model for the biomechanical analysis of tendons. *Med. Eng. Phys.*, 27(3):209–214, apr 2005.
- [150] R. J. Nims and G. A. Ateshian. Reactive Constrained Mixtures for Modeling the Solid Matrix of Biological Tissues. *J. Elast.*, mar 2017.
- [151] R. J. Nims, K. M. Durney, A. D. Cigan, A. Dusséaux, C. T. Hung, and G. A. Ateshian. Continuum theory of fibrous tissue damage mechanics using bond kinetics: application to cartilage tissue engineering. *Interface Focus*, 6(1):20150063, feb 2016.
- [152] R. Oftadeh, B. K. Connizzo, H. T. Nia, C. Ortiz, and A. J. Grodzinsky. Biological connective tissues exhibit viscoelastic and poroelastic behavior at different frequency regimes: Application to tendon and skin biophysics. *Acta Biomater.*, 70:249–259, apr 2018.
- [153] J. P. R. O. Orgel, T. C. Irving, A. Miller, and T. J. Wess. Microfibrillar structure of type I collagen in situ. *Proc. Natl. Acad. Sci. U. S. A.*, 103(24):9001–5, jun 2006.
- [154] R. W. Park and D. R. Stenton. *Ancient Harpoon Heads of Nunavut: an Illustrated Guide*. Parks Canada, 1998.

- [155] M. Parkes, P. Cann, and J. Jeffers. Real-time observation of fluid flows in tissue during stress relaxation using Raman spectroscopy. *J. Biomech.*, 60:261–265, jun 2017.
- [156] D. A. Parry, G. R. Barnes, and A. S. Craig. A comparison of the size distribution of collagen fibrils in connective tissues as a function of age and a possible relation between fibril size distribution and mechanical properties. *Proc. R. Soc. London. Ser. B. Biol. Sci.*, 203(1152):305–321, dec 1978.
- [157] C. Paul Buckley, S. T. Samuel Salisbury, and A. B. Zavatsky. Viscoelasticity of Tendons Under Transverse Compression. *J. Biomech. Eng.*, 138(10):101004, oct 2016.
- [158] J. M. Peloquin, M. H. Santare, and D. M. Elliott. Advances in Quantification of Meniscus Tensile Mechanics Including Nonlinearity, Yield, and Failure. *J. Biomech. Eng.*, 138(2):021002, jan 2016.
- [159] E. Peña. Prediction of the softening and damage effects with permanent set in fibrous biological materials. *J. Mech. Phys. Solids*, 59(9):1808–1822, sep 2011.
- [160] E. Peña. Computational aspects of the numerical modelling of softening, damage and permanent set in soft biological tissues. *Comput. Struct.*, 130:57–72, jan 2014.
- [161] E. Peña, B. Calvo, M. A. Martínez, and M. Doblaré. An anisotropic visco-hyperelastic model for ligaments at finite strains. Formulation and computational aspects. *Int. J. Solids Struct.*, 44(3-4):760–778, feb 2007.
- [162] M. Pensalfini, S. Duenwald-Kuehl, J. Kondratko-Mittnacht, R. Lakes, and R. Vanderby. Evaluation of global load sharing and shear-lag models to describe mechanical behavior in partially lacerated tendons. *J. Biomech. Eng.*, 136(9):091006, sep 2014.
- [163] J. Pingel, Y. Lu, T. Starborg, U. Fredberg, H. Langberg, A. Nedergaard, M. Weis, D. Eyre, M. Kjaer, and K. E. Kadler. 3-D ultrastructure and collagen composition of healthy and overloaded human tendon: Evidence of tenocyte and matrix buckling. *J. Anat.*, 224(5):548–555, may 2014.
- [164] P. P. Provenzano, K. Hayashi, D. N. Kunz, M. D. Markel, and R. J. Vanderby. Healing of subfailure ligament injury: comparison between immature and mature ligaments in a rat model. *J. Orthop. Res.*, 20(5):975–983, sep 2002.
- [165] P. P. Provenzano, D. Heisey, K. Hayashi, R. Lakes, and R. Vanderby. Subfailure damage in ligament: a structural and cellular evaluation. *J. Appl. Physiol.*, 92(1):362–371, 2002.

- [166] P. P. Provenzano and R. Vanderby. Collagen fibril morphology and organization: implications for force transmission in ligament and tendon. *Matrix Biol.*, 25(2):71–84, mar 2006.
- [167] M. A. Puso and J. A. Weiss. Finite element implementation of anisotropic quasi-linear viscoelasticity using a discrete spectrum approximation. *J. Biomech. Eng.*, 120(1):62–70, feb 1998.
- [168] K. Rajagopal and A. Wineman. A constitutive equation for nonlinear solids which undergo deformation induced microstructural changes. *Int. J. Plast.*, 8(4):385–395, jan 1992.
- [169] K. R. Rajagopal and A. R. Srinivasa. On the thermomechanics of materials that have multiple natural configurations Part I: Viscoelasticity and classical plasticity, 2004.
- [170] M. K. Rausch, S. Reese, S. Maas, and J. A. Weiss. Can Poroelasticity Predict the Cyclic Tensile Viscoelastic Behavior of Ligament? In *Society*, volume 119, pages 2007–2007, Las Vegas, NV, 2007.
- [171] E. Raz and Y. Lanir. Recruitment Viscoelasticity of the Tendon. *J. Biomech. Eng.*, 131(11):111008, oct 2009.
- [172] A. Redaelli, S. Vesentini, M. Soncini, S. P. Veres, S. Mantero, and F. Montevecchi. Possible role of decorin glycosaminoglycans in fibril to fibril force transfer in relative mature tendons: a computational study from molecular to microstructural level. *J. Biomech.*, 36(10):1555–1569, oct 2003.
- [173] R. Reed, M. J. Wood, and M. K. Keech. Helical Nature of the Collagen Fibril. *Nature*, 177(4511):697–699, apr 1956.
- [174] S. Reese and S. Govindjee. A theory of finite viscoelasticity and numerical aspects. *Int. J. Solids Struct.*, 35(26-27):3455–3482, sep 1998.
- [175] S. P. Reese, S. A. Maas, and J. A. Weiss. Micromechanical models of helical superstructures in ligament and tendon fibers predict large Poisson’s ratios. *J. Biomech.*, 43(7):1394–400, may 2010.
- [176] S. P. Reese and J. a. Weiss. Tendon fascicles exhibit a linear correlation between poisson’s ratio and force during uniaxial stress relaxation. *J. Biomech. Eng.*, 135(3):34501, mar 2013.
- [177] K. Reiser, R. J. McCormick, and R. B. Rucker. Enzymatic and nonenzymatic cross-linking of collagen and elastin. *FASEB J.*, 6(7):2439–49, apr 1992.
- [178] B. J. Rigby. Effect of cyclic extension on the physical properties of tendon collagen and its possible relation to biological ageing of collagen. *Nature*, 202(4937):1072–1074, 1964.

- [179] S. J. Ros, N. Andarawis-Puri, and E. L. Flatow. Tendon extracellular matrix damage detection and quantification using automated edge detection analysis. *J. Biomech.*, 46(16):2844–7, nov 2013.
- [180] M. S. Sacks. Incorporation of Experimentally-Derived Fiber Orientation into a Structural Constitutive Model for Planar Collagenous Tissues. *J. Biomech. Eng.*, 125(2):280, apr 2003.
- [181] B. N. Safa. ReactiveBond. <https://github.com/BabakNSafa/ReactiveBond/>, 2018.
- [182] B. N. Safa, A. H. Lee, M. H. Santare, and D. M. Elliott. Evaluating Plastic Deformation and Damage as Potential Mechanisms for Tendon Inelasticity Using a Reactive Modeling Framework. *J. Biomech. Eng.*, 141(10):101008, jul 2019.
- [183] B. N. Safa, K. D. Meadows, S. E. Szczesny, and D. M. Elliott. Exposure to buffer solution alters tendon hydration and mechanics. *J. Biomech.*, 61:18–25, aug 2017.
- [184] B. N. Safa, J. M. Peloquin, J. R. Natriello, J. L. Caplan, and D. M. Elliott. Helical Fibrillar Microstructure of Tendon using Serial Block-Face SEM and a Mechanical Model for Interfibrillar Load Transfer. *bioRxiv*, page 547281, aug 2019.
- [185] B. N. Safa, M. H. Santare, and D. M. Elliott. A Reactive Inelasticity Theoretical Framework for Modeling Viscoelasticity, Plastic Deformation, and Damage in Fibrous Soft Tissue. *J. Biomech. Eng.*, 141(2):021005, dec 2018.
- [186] Sally Pointer and Gareth Reiborough. Tendon and Sinew Rope (sally-pointer.com), 2014.
- [187] S. T. Samuel Salisbury, C. Paul Buckley, and A. B. Zavatsky. Transverse Compression of Tendons. *J. Biomech. Eng.*, 138(4):041002, feb 2016.
- [188] J. J. Sarver, P. S. Robinson, and D. M. Elliott. Methods for Quasi-Linear Viscoelastic Modeling of Soft Tissue: Application to Incremental Stress-Relaxation Experiments. *J. Biomech. Eng.*, 125(5):754, oct 2003.
- [189] T. Schmidt, D. Balzani, and G. Holzapfel. Statistical approach for a continuum description of damage evolution in soft collagenous tissues. *Comput. Methods Appl. Mech. Eng.*, 278:41–61, aug 2014.
- [190] J. F. Schutte, B.-I. Koh, J. A. Reinbolt, R. T. Haftka, A. D. George, and B. J. Fregly. Evaluation of a Particle Swarm Algorithm For Biomechanical Optimization. *J. Biomech. Eng.*, 127(3):465, jun 2005.

- [191] T. D. Schwab, C. R. Johnston, T. R. Oxland, and G. M. Thornton. Continuum damage mechanics (CDM) modelling demonstrates that ligament fatigue damage accumulates by different mechanisms than creep damage. *J. Biomech.*, 40(14):3279–84, jan 2007.
- [192] K. W. Scott and R. S. Stein. A Molecular Theory of Stress Relaxation in Polymeric Media. *J. Chem. Phys.*, 21(7):1281–1286, jul 1953.
- [193] H. R. Screen. Investigating load relaxation mechanics in tendon. *J. Mech. Behav. Biomed. Mater.*, 1(1):51–58, jan 2008.
- [194] H. R. Screen, V. H. Chhaya, S. E. Greenwald, D. L. Bader, D. A. Lee, and J. C. Shelton. The influence of swelling and matrix degradation on the microstructural integrity of tendon. *Acta Biomater.*, 2(5):505–513, sep 2006.
- [195] H. R. Screen, J. C. Shelton, V. H. Chhaya, M. V. Kayser, D. L. Bader, and D. A. Lee. The Influence of Noncollagenous Matrix Components on the Micromechanical Environment of Tendon Fascicles. *Ann. Biomed. Eng.*, 33(8):1090–1099, aug 2005.
- [196] S. B. Shah, C. Witzenburg, M. F. Hadi, H. P. Wagner, J. M. Goodrich, P. W. Alford, and V. H. Barocas. Prefailure and failure mechanics of the porcine ascending thoracic aorta: experiments and a multiscale model. *J. Biomech. Eng.*, 136(2):021028, feb 2014.
- [197] D. Shahmirzadi and A. H. Hsieh. An efficient technique for adjusting and maintaining specific hydration levels in soft biological tissues in vitro. *Med. Eng. Phys.*, 32(7):795–801, sep 2010.
- [198] Z. L. Shen, M. R. Dodge, H. Kahn, R. Ballarini, and S. J. Eppell. Stress-Strain Experiments on Individual Collagen Fibrils. *Biophys. J.*, 95(8):3956–3963, oct 2008.
- [199] J. Simo. On a fully three-dimensional finite-strain viscoelastic damage model: Formulation and computational aspects. *Comput. Methods Appl. Mech. Eng.*, 60(2):153–173, feb 1987.
- [200] J. Simo. A framework for finite strain elastoplasticity based on maximum plastic dissipation and the multiplicative decomposition: Part I. Continuum formulation. *Comput. Methods Appl. Mech. Eng.*, 66(2):199–219, 1988.
- [201] J. C. Simo and T. J. R. Hughes. *Computational Inelasticity*. Interdisciplinary Applied Mathematics. Springer-Verlag, New York, 1998.
- [202] J. C. Simo and J. W. Ju. Strain- and stress-based continuum damage model - I. Formulation. *Int. J. Solids Struct.*, 23:821–840, 1987.

- [203] J. G. Snedeker and J. Foolen. Tendon injury and repair A perspective on the basic mechanisms of tendon disease and future clinical therapy, nov 2017.
- [204] J. G. Snedeker and A. Gautieri. The role of collagen crosslinks in ageing and diabetes - the good, the bad, and the ugly. *Muscles. Ligaments Tendons J.*, 4(3):303–8, jul 2014.
- [205] A. J. Spencer. *Continuum Theory of the Mechanics of Fibre-Reinforced Composites*. Springer Vienna, Vienna, 1984.
- [206] T. Starborg and K. E. Kadler. Serial block face-scanning electron microscopy: A tool for studying embryonic development at the cell-matrix interface. *Birth Defects Res. Part C - Embryo Today Rev.*, 105(1):9–18, mar 2015.
- [207] T. Starborg, N. S. Kalson, Y. Lu, A. Mironov, T. F. Cootes, D. F. Holmes, and K. E. Kadler. Using transmission electron microscopy and 3View to determine collagen fibril size and three-dimensional organization. *Nat. Protoc.*, 8(7):1433–48, jan 2013.
- [208] M. J. Sutcliffe, S. R. Taylor, and A. Cameron. Molecular asperity theory of boundary friction. *Wear*, 51(1):181–192, nov 1978.
- [209] R. B. Svensson, A. Herchenhan, T. Starborg, M. Larsen, K. E. Kadler, K. Qvortrup, S. P. Magnusson, S. Peter Magnusson, and S. P. Magnusson. Evidence of structurally continuous collagen fibrils in tendons. *Acta Biomater.*, 50:293–301, mar 2017.
- [210] A. Sverdlik and Y. Lanir. Time-dependent mechanical behavior of sheep digital tendons, including the effects of preconditioning. *J Biomech Eng*, 124(1):78–84, 2002.
- [211] A. M. Swedberg, S. P. Reese, S. A. Maas, B. J. Ellis, and J. A. Weiss. Continuum description of the Poisson’s ratio of ligament and tendon under finite deformation. *J. Biomech.*, 47(12):3201–9, sep 2014.
- [212] S. E. Szczesny, C. Aeppli, A. David, and R. L. Mauck. Fatigue loading of tendon results in collagen kinking and denaturation but does not change local tissue mechanics. *J. Biomech.*, 71:251–256, apr 2018.
- [213] S. E. Szczesny, J. L. Caplan, P. Pedersen, and D. M. Elliott. Quantification of Interfibrillar Shear Stress in Aligned Soft Collagenous Tissues via Notch Tension Testing. *Sci. Rep.*, 5:14649, jan 2015.
- [214] S. E. Szczesny, R. S. Edelman, and D. M. Elliott. DTAF dye concentrations commonly used to measure microscale deformations in biological tissues alter tissue mechanics. *PLoS One*, 9(6):e99588, jan 2014.

- [215] S. E. Szczesny and D. M. Elliott. Incorporating plasticity of the interfibrillar matrix in shear lag models is necessary to replicate the multiscale mechanics of tendon fascicles. *J. Mech. Behav. Biomed. Mater.*, 40:325–338, dec 2014.
- [216] S. E. Szczesny and D. M. Elliott. Interfibrillar shear stress is the loading mechanism of collagen fibrils in tendon. *Acta Biomater.*, 10(6):2582–2590, jun 2014.
- [217] S. E. Szczesny, K. L. Fetchko, G. R. Dodge, and D. M. Elliott. Evidence that interfibrillar load transfer in tendon is supported by small diameter fibrils and not extrafibrillar tissue components. *J. Orthop. Res.*, 35(10):2127–2134, oct 2017.
- [218] F. Tanaka and S. Edwards. Viscoelastic properties of physically crosslinked networks. *J. Nonnewton. Fluid Mech.*, 43(2-3):273–288, jul 1992.
- [219] G. M. Thornton, A. Oliynyk, C. B. Frank, and N. G. Shrive. Ligament creep cannot be predicted from stress relaxation at low stress: A biomechanical study of the rabbit medial collateral ligament. *J. Orthop. Res.*, 15(5):652–656, sep 1997.
- [220] G. M. Thornton, T. D. Schwab, and T. R. Oxland. Fatigue is more damaging than creep in ligament revealed by modulus reduction and residual strength. *Ann. Biomed. Eng.*, 35(10):1713–21, oct 2007.
- [221] G. M. Thornton, N. G. Shrive, and C. B. Frank. Altering ligament water content affects ligament pre-stress and creep behavior. *J. Orthop. Res.*, 19(5):845–851, sep 2001.
- [222] C. T. Thorpe, C. Klemt, G. P. Riley, H. L. Birch, P. D. Clegg, and H. R. Screen. Helical sub-structures in energy-storing tendons provide a possible mechanism for efficient energy storage and return. *Acta Biomater.*, 9(8):7948–7956, 2013.
- [223] A. V. Tobolsky and R. D. Andrews. Systems Manifesting Superposed Elastic and Viscous Behavior. *J. Chem. Phys.*, 13(1):3–27, jan 1945.
- [224] T. K. Tonge, J. W. Ruberti, and T. D. Nguyen. Micromechanical Modeling Study of Mechanical Inhibition of Enzymatic Degradation of Collagen Tissues. *Biophys. J.*, 109(12):2689–2700, dec 2015.
- [225] Unknown. Death of Achilles Painting on Ancient Greek Vase 540 BCE.
- [226] M. Vaz, E. L. Cardoso, and J. Stahlschmidt. Particle swarm optimization and identification of inelastic material parameters. *Eng. Comput. (Swansea, Wales)*, 30(7):936–960, oct 2013.
- [227] S. P. Veres, J. M. Harrison, and J. M. Lee. Mechanically overloading collagen fibrils uncoils collagen molecules, placing them in a stable, denatured state. *Matrix Biol.*, 2014.

- [228] S. P. Veres and J. M. Lee. Designed to fail: a novel mode of collagen fibril disruption and its relevance to tissue toughness. *Biophys. J.*, 102(12):2876–84, jun 2012.
- [229] A. Viinikainen, H. Göransson, and J. Ryhänen. Primary flexor tendon repair techniques, dec 2008.
- [230] G. A. Von Forell and A. E. Bowden. A damage model for the percutaneous triple hemisection technique for tendo-achilles lengthening. *J. Biomech.*, 47(13):3354–3360, oct 2014.
- [231] G. Z. Voyiadjis and P. I. Kattan. A Comparative Study of Damage Variables in Continuum Damage Mechanics. *Int. J. Damage Mech.*, 18(May):315–340, 2008.
- [232] L. Wang, C. Zheng, H. Luo, S. Wei, and Z. Wei. Continuum damage modeling and progressive failure analysis of carbon fiber/epoxy composite pressure vessel. *Compos. Struct.*, 134:475–482, dec 2015.
- [233] X. T. Wang and R. F. Ker. Creep rupture of wallaby tail tendons. *J. Exp. Biol.*, 198(Pt 3):831–45, mar 1995.
- [234] A. Ward, F. Hilitski, W. Schwenger, D. Welch, A. W. Lau, V. Vitelli, L. Mahadevan, and Z. Dogic. Solid friction between soft filaments. *Nat. Mater.*, 14(6):583–588, jun 2015.
- [235] H. Weisbecker, D. M. Pierce, P. Regitnig, and G. A. Holzapfel. Layer-specific damage experiments and modeling of human thoracic and abdominal aortas with non-atherosclerotic intimal thickening. *J. Mech. Behav. Biomed. Mater.*, 12(2):93–106, 2012.
- [236] J. A. Weiss and B. J. Maakestad. Permeability of human medial collateral ligament in compression transverse to the collagen fiber direction. *J. Biomech.*, 39(2):276–283, jan 2006.
- [237] H. C. Wells, K. H. Sizeland, H. R. Kaye, N. Kirby, A. Hawley, S. T. Mudie, and R. G. Haverkamp. Poisson’s ratio of collagen fibrils measured by small angle X-ray scattering of strained bovine pericardium. *J. Appl. Phys.*, 117(4):184905, 2015.
- [238] M. P. E. Wenger, L. Bozec, M. A. Horton, and P. Mesquida. Mechanical properties of collagen fibrils. *Biophys. J.*, 93(4):1255–63, aug 2007.
- [239] A. Wineman. On the mechanics of elastomers undergoing scission and cross-linking. *Int. J. Adv. Eng. Sci. Appl. Math.*, 1(2-3):123–131, sep 2009.
- [240] S. L. Woo, G. A. Johnson, and B. A. Smith. Mathematical modeling of ligaments and tendons. *J. Biomech. Eng.*, 115(4B):468–73, nov 1993.

- [241] S. L. Woo, B. R. Simon, S. C. Kuei, and W. H. Akeson. Quasi-Linear Viscoelastic Properties of Normal Articular Cartilage. *J. Biomech. Eng.*, 102(2):85, may 1980.
- [242] T. A. Wren, S. A. Yerby, G. S. Beaupré, and D. R. Carter. Mechanical properties of the human achilles tendon. *Clin. Biomech.*, 16(3):245–251, mar 2001.
- [243] Y. Yang, A. Rupani, P. Bagnaninchi, I. Wimpenny, and A. Weightman. Study of optical properties and proteoglycan content of tendons by polarization sensitive optical coherence tomography. *J. Biomed. Opt.*, 17(8):081417, 2012.
- [244] C.-Y. C. Yeung, R. Garva, A. Pickard, J. Chang, D. F. Holmes, Y. Lu, V. Mallikarjun, J. Swift, A. Adamson, B. Calverley, Q. J. Meng, and K. E. Kadler. Circadian Clock Regulation of the Secretory Pathway, apr 2018.
- [245] L. Yin and D. M. Elliott. A biphasic and transversely isotropic mechanical model for tendon: application to mouse tail fascicles in uniaxial tension. *J. Biomech.*, 37(6):907–16, jun 2004.
- [246] V. Zarei, C. J. Liu, A. A. Claeson, T. Akkin, and V. H. Barocas. Image-based multiscale mechanical modeling shows the importance of structural heterogeneity in the human lumbar facet capsular ligament. *Biomech. Model. Mechanobiol.*, 16(4):1425–1438, aug 2017.
- [247] W. Zhang and M. S. Sacks. Modeling the response of exogenously crosslinked tissue to cyclic loading: The effects of permanent set. *J. Mech. Behav. Biomed. Mater.*, 75:336–350, nov 2017.
- [248] B. K. Zimmerman and G. A. Ateshian. A Surface-to-Surface Finite Element Algorithm for Large Deformation Frictional Contact in febio. *J. Biomech. Eng.*, 140(8):081013, aug 2018.
- [249] J. L. Zitnay, Y. Li, Z. Qin, B. H. San, B. Depalle, S. P. Reese, M. J. Buehler, S. M. Yu, and J. A. Weiss. Molecular level detection and localization of mechanical damage in collagen enabled by collagen hybridizing peptides. *Nat. Commun.*, 8:14913, mar 2017.

Appendices

Appendix A

STRESS AND RELATIVE DEFORMATION

By using the definition of free energy of the system from Eq. (4.11) the second Piola-Kirchhoff stress tensor for a bond type in terms of number fraction of bonds (w^α) and relative deformation (represented by relative right Cauchy-Green deformation \mathbf{C}^α) is

$$\mathbf{S} = 2 \frac{\partial \Psi(\mathbf{C}^\alpha)}{\partial \mathbf{C}} = \sum_{\alpha} 2w^\alpha \frac{\partial \psi(\mathbf{C}^\alpha)}{\partial \mathbf{C}}. \quad (\text{A.1})$$

Using the chain rule of differentiation and Einstein's index notation:

$$\frac{\partial \psi}{\partial C_{ij}} = \frac{\partial \psi}{\partial C_{mn}^\alpha} \frac{\partial C_{mn}^\alpha}{\partial C_{ij}}. \quad (\text{A.2})$$

Using Eq. (4.2) and noting that the reference deformation gradient tensor ($\mathbf{\Pi}^\alpha$) is fixed for a specific generation;

$$\begin{aligned} \frac{\partial C_{mn}^\alpha}{\partial C_{ij}} &= \frac{\partial ((\Pi_{pm}^\alpha)^{-1} C_{pq} (\Pi_{qn}^\alpha)^{-1})}{\partial C_{ij}} \\ &= (\Pi_{pm}^\alpha)^{-1} \delta_{pi} \delta_{qj} (\Pi_{qn}^\alpha)^{-1} \\ &= (\Pi_{im}^\alpha)^{-1} (\Pi_{jn}^\alpha)^{-1}. \end{aligned} \quad (\text{A.3})$$

By substituting this result back

$$\frac{\partial \psi}{\partial C_{ij}} = \frac{\partial \psi}{\partial C_{mn}^\alpha} (\Pi_{im}^\alpha)^{-1} (\Pi_{jn}^\alpha)^{-1}. \quad (\text{A.4})$$

Or, in tensor notation

$$\frac{\partial \psi(\mathbf{C}^\alpha)}{\partial \mathbf{C}} = (\mathbf{\Pi}^\alpha)^{-1} \frac{\partial \psi(\mathbf{C}^\alpha)}{\partial \mathbf{C}^\alpha} (\mathbf{\Pi}^\alpha)^{-T}. \quad (\text{A.5})$$

And, finally we can write

$$\mathbf{S} = \sum_{\alpha} 2w^{\alpha}(\mathbf{\Pi}^{\alpha})^{-1} \frac{\psi(\mathbf{C}^{\alpha})}{\partial \mathbf{C}^{\alpha}} (\mathbf{\Pi}^{\alpha})^{-T}, \quad (\text{A.6})$$

which provides the full form of the second Piola-Kirchhoff stress for a bond type in a reactive material, Eq. (4.13).

Appendix B

PROOF OF THE STRUCTURE TENSOR (\tilde{M}^α) EXPRESSION FOR SLIDING BONDS

By assuming that the stretch in the fiber direction for the reference configuration of the α generation is λ_s^α , which has a value that is infinitesimally different from that of generation $(\alpha - 1)$, and by using Taylor's approximation one can show

$$(\lambda_s^\alpha)^2 \approx (\lambda_s^{\alpha-1})^2 + 2(\lambda_s^{\alpha-1})\Delta\lambda_s^\alpha. \quad (\text{B.1})$$

Additionally, based on Eq. (4.31) from the corresponding sliding configuration deformation gradients we have:

$$\begin{aligned} (\lambda_s^\alpha)^2 &= \mathbf{e}_s^0 (\mathbf{\Pi}_s^\alpha)^T \mathbf{\Pi}_s^\alpha \mathbf{e}_s^0 \\ &= \mathbf{e}_s^0 [((\mathbf{\Pi}_s^{\alpha-1})^T + (\Delta\mathbf{\Pi}_s^\alpha)^T) (\mathbf{\Pi}_s^{\alpha-1} + \Delta\mathbf{\Pi}_s^\alpha)] \mathbf{e}_s^0 \\ &\approx \mathbf{e}_s^0 [(\mathbf{\Pi}_s^{\alpha-1})^T \mathbf{\Pi}_s^{\alpha-1} + (\Delta\mathbf{\Pi}_s^\alpha)^T \mathbf{\Pi}_s^{\alpha-1} + (\mathbf{\Pi}_s^{\alpha-1})^T \Delta\mathbf{\Pi}_s^\alpha] \mathbf{e}_s^0 \end{aligned} \quad (\text{B.2})$$

By substituting $(\lambda_s^{\alpha-1})^2 = \mathbf{e}_s^0 (\mathbf{\Pi}_s^{\alpha-1})^T \mathbf{\Pi}_s^{\alpha-1} \mathbf{e}_s^0$ we get

$$\mathbf{e}_s^0 [(\Delta\mathbf{\Pi}_s^\alpha)^T \mathbf{\Pi}_s^{\alpha-1} + (\mathbf{\Pi}_s^{\alpha-1})^T \Delta\mathbf{\Pi}_s^\alpha] \mathbf{e}_s^0 = 2(\lambda_s^{\alpha-1})\Delta\lambda_s^\alpha. \quad (\text{B.3})$$

Therefore, by assuming $\mathbf{e}_s^{\alpha-1} = \mathbf{e}_s^0$, one can easily show that

$$\Delta\mathbf{\Pi}_s^\alpha = \Delta\lambda_s^\alpha \mathbf{e}_s^0 \otimes \mathbf{e}_s^0 \quad (\text{B.4})$$

holds. Finally, by taking that $\Delta\lambda_s^\alpha = \partial_{\Xi_s} f_s(\Xi_s) \Delta\Xi_s$ the expression $\tilde{M}^\alpha = \mathbf{e}_s^0 \otimes \mathbf{e}_s^0$ is resulted in terms of Eq. (4.38). This relation indicates that during sliding, the

dominant fiber direction is preserved and only the reference length changes. This relation can be enhanced by including the effect of permanent changes to the dominant fiber direction as seen in some fibrous tissues, such as the intervertebral disc [50], by using phenomenological relations to correlate e_s^0 and $e_s^{\alpha-1}$.

Appendix C

IMPLICATIONS OF THE SECOND LAW OF THERMODYNAMICS

C.1 Second law of thermodynamics

Any physical process must comply with the second law of thermodynamics, thus we check for compatibility of reactive inelasticity with the second law of thermodynamics in terms of the Clausius-Duhem inequality. By neglecting the thermal effects, the local form of Clausius-Duhem inequality reads as [34]

$$\mathcal{D} = \frac{1}{2} \mathbf{S} : \dot{\mathbf{C}} - \dot{\Psi}(\mathbf{C}, w^\alpha, \mathbf{\Pi}^\alpha, D) \geq 0, \quad (\text{C.1})$$

where \mathcal{D} is the instantaneous local dissipation of energy, and for convenience will be referred to as dissipation. Here, (\cdot) is the double contraction ($(\mathbf{A} : \mathbf{B})_{ij} = A_{ij}B_{ij}$) and dot stands for material time derivative. Using the chain rule of differentiation and Eq. (4.11) we get

$$\begin{aligned} \left(\frac{1}{2} \mathbf{S} - (1 - D) \sum_{\alpha} w^{\alpha} \frac{\partial \psi(\mathbf{C}^{\alpha})}{\partial \mathbf{C}} \right) : \dot{\mathbf{C}} - (1 - D) \sum_{\alpha} \dot{w}^{\alpha} \psi(\mathbf{C}^{\alpha}) \\ - (1 - D) \sum_{\alpha} w^{\alpha} \left(\frac{\partial \psi(\mathbf{C}^{\alpha})}{\partial \mathbf{\Pi}^{\alpha}} : \dot{\mathbf{\Pi}}^{\alpha} \right) \\ + \dot{D} \sum_{\alpha} w^{\alpha} \psi(\mathbf{C}^{\alpha}) \geq 0. \end{aligned} \quad (\text{C.2})$$

Thus, to have a physically admissible process in the most general case each of the following conditions should be separately satisfied [34, 146]

$$\mathbf{S} = (1 - D) \sum_{\alpha} w^{\alpha} 2 \frac{\partial \psi(\mathbf{C}^{\alpha})}{\partial \mathbf{C}} \quad (\text{C.3a})$$

$$\mathcal{D} = \mathcal{D}_R + \mathcal{D}_D \geq 0, \quad (\text{C.3b})$$

where

$$\mathcal{D}_R = -(1 - D) \sum_{\alpha} \left(\dot{w}^{\alpha} \psi(\mathbf{C}^{\alpha}) + w^{\alpha} \frac{\partial \psi(\mathbf{C}^{\alpha})}{\partial \mathbf{\Pi}^{\alpha}} : \dot{\mathbf{\Pi}}^{\alpha} \right), \text{ and} \quad (\text{C.4a})$$

$$\mathcal{D}_D = \dot{D} \sum_{\alpha} w^{\alpha} \psi(\mathbf{C}^{\alpha}). \quad (\text{C.4b})$$

The first condition results in a new form of Eq. (4.12) where stress is scaled with damage. The second condition describes the dissipation of energy in a reactive inelastic process, where \mathcal{D}_R is dissipation due to reactive bond breaking/reformations and change in reference configuration, and \mathcal{D}_D is the dissipation due to damage.

C.2 Reactive bond compliance with the conditions of the second law

In the following, we investigate the compatibility of different bond types with the second law of thermodynamics. At a given time, consider a set of bonds from the same type that are grouped into breaking generations ($\alpha \in \{0, \dots, (N - 1)\}$) and a reforming generation ($\alpha = N$), hence

$$\mathcal{D}_R = -(1 - D) \left[\underbrace{\left(\sum_{\alpha=0}^{N-1} \dot{w}^{\alpha} \psi(\mathbf{C}^{\alpha}) + w^{\alpha} \frac{\partial \psi(\mathbf{C}^{\alpha})}{\partial \mathbf{\Pi}^{\alpha}} : \dot{\mathbf{\Pi}}^{\alpha} \right)}_{\text{breaking generations}} + \underbrace{\left(\dot{w}^N \psi(\mathbf{C}^N) + w^N \frac{\partial \psi(\mathbf{C}^N)}{\partial \mathbf{\Pi}^N} : \dot{\mathbf{\Pi}}^N \right)}_{\text{reforming generation}} \right]. \quad (\text{C.5})$$

C.2.1 Formative bonds

According to Eq. (4.26) for all of the breaking bonds we have

$$\dot{w}_f^\alpha < 0, \quad (\text{C.6})$$

and we know in general that the free energy in a deformed state is considered positive

$$\psi_f(\mathbf{C}^\alpha) > 0. \quad (\text{C.7})$$

Additionally, the reforming bonds reform in an energy free state (Section 4.2.4.1)

$$\psi_f(\mathbf{C}^N = \mathbf{I}) = 0. \quad (\text{C.8})$$

For the breaking formative bonds the reference deformation gradient is fixed ($\dot{\mathbf{\Pi}}_f^\alpha = \mathbf{0}, \alpha < N$) and for their reforming generation ($\alpha = N$) (Eq. (4.29))

$$\mathbf{\Pi}_f^N = \mathbf{\Pi}_f^{N-1} + u(t - t^N)\Delta\mathbf{\Pi}_f^N, \text{ and } \dot{\mathbf{\Pi}}_f^N = \delta(t - t^N)\Delta\mathbf{\Pi}_f^N, \quad (\text{C.9})$$

where $u(t)$ denotes the unit step function, and $\delta(t)$ is the Dirac delta function. Further, using Eq. (4.27) one can show

$$w_f^N \dot{\mathbf{\Pi}}_f^N = \delta(t - t^N) w_f^N \Delta\mathbf{\Pi}_f^N = \mathbf{0}. \quad (\text{C.10})$$

Therefore, for formative bonds

$$(\mathcal{D}_R)_f = -(1 - D_f) \sum_{\alpha=0}^{N-1} \dot{w}_f^\alpha \psi(\mathbf{C}^\alpha) \geq 0, \quad (\text{C.11})$$

which indicates that during breaking and reformation of formative bonds, dissipation is positive and is due solely to breakage of bonds.

C.2.2 Permanent bonds

Since for these bonds there is just one generation and there is no breakage and reformation, we have ($\dot{w}_p^0 = 0$ and $\mathbf{\Pi}_p^0 = \mathbf{I}$) as a result

$$(\mathcal{D}_R)_p = 0. \quad (\text{C.12})$$

This result denotes that there is no dissipation of energy for permanent bonds due to a lack of reactive breaking and reformation.

C.2.3 Sliding bonds

For these bonds, the only generations with non-zero dissipation terms are the last breaking ($\alpha = N - 1$) and the reforming generations ($\alpha = N$). Their number fractions and kinetics rates are (Section 4.2.4.3)

$$w_s^{N-1}(t) = 1 - u(t - t^N), \quad w_s^N(t) = u(t - t^N), \quad (\text{C.13a})$$

$$\dot{w}_s^{N-1}(t) = -\delta(t - t^N), \quad \dot{w}_s^N(t) = \delta(t - t^N). \quad (\text{C.13b})$$

In addition, according to Eqs. (4.31) and (4.40) the corresponding $\dot{\mathbf{\Pi}}_s$ for those bonds during sliding reads as

$$\dot{\mathbf{\Pi}}_s^{N-1}(t) = \mathbf{0}, \text{ and } \dot{\mathbf{\Pi}}_s^N(t) = \delta(t - t^N) \Delta \mathbf{\Pi}_s^N. \quad (\text{C.14})$$

As a result

$$\begin{aligned} (\mathcal{D}_R)_s &= \delta(t - t^N)(1 - D_s) \left[(\psi(\mathbf{C}_s^{N-1}) - \psi(\mathbf{C}_s^N)) - \frac{\partial \psi(\mathbf{C}_s^N)}{\partial \mathbf{\Pi}_s^N} : \Delta \mathbf{\Pi}_s^N \right] \\ &= -2\delta(t - t^N)(1 - D_s) \frac{\partial \psi(\mathbf{C}_s^N)}{\partial \mathbf{\Pi}_s^N} : \Delta \mathbf{\Pi}_s^N, \end{aligned} \quad (\text{C.15})$$

where we used the Taylor series to write $\psi(\mathbf{C}_s^N) - \psi(\mathbf{C}_s^{N-1}) \approx (\partial\psi(\mathbf{C}_s^N)/\partial\mathbf{\Pi}_s^N) : \Delta\mathbf{\Pi}_s^N$. Therefore, half of this dissipation is driven by the process of breakage and reformation, and the other half is explicitly due to a shift in the reference configuration. The above relation corresponds to a positive value for dissipation when

$$-\frac{\partial\psi(\mathbf{C}_s^N)}{\partial\mathbf{\Pi}^N} : \Delta\mathbf{\Pi}^N \geq 0. \quad (\text{C.16})$$

For the constitutive relations and deformation used in this paper, we can analytically verify the above inequality as follows.

C.2.3.1 Exponential fibers

Since the only non-zero component of the deformation and stress is in the fiber direction, a one dimensional formulation can be used for convenience, where $\mathbf{\Pi}_s^N$ is represented by λ_s^N . As a result, the dissipation inequality reads as

$$\begin{aligned} -\frac{\partial\psi_{EF}(I_4^N)}{\partial\mathbf{\Pi}^N} : \Delta\mathbf{\Pi}^N &= -\frac{\partial\psi_{EF}(\lambda/\lambda_s^N)}{\partial\lambda_s^N} \Delta\lambda_s^N \\ &= 4C_2C_3 \left(\frac{\lambda}{\lambda_s^N}\right)^3 \exp \left[C_3 \left(\left(\frac{\lambda}{\lambda_s^N}\right)^2 - 1 \right)^2 \right] \left(\left(\frac{\lambda}{\lambda_s^N}\right)^2 - 1 \right) \frac{\Delta\lambda_s^N}{\lambda} \end{aligned} \quad (\text{C.17})$$

where $\Delta\lambda_s^N = \lambda_s^N - \lambda_s^{N-1}$. As a result, since $\lambda^{N-1} < \lambda^N < \lambda$ the above expression has a positive value.

C.2.3.2 Neo-Hookean

Because of the assumption that $\mathbf{F} = \hat{\mathbf{F}}(\lambda)$, $\Delta\mathbf{\Pi}^N$ can be written as $\hat{\mathbf{F}}(\lambda_s^N) - \hat{\mathbf{F}}(\lambda_s^{N-1})$ and by using the Taylor's expansion

$$\Delta\mathbf{\Pi}^N = \begin{bmatrix} -\frac{1}{2}(\lambda_s^{N-1})^{-\frac{3}{2}} & 0 & 0 \\ 0 & -\frac{1}{2}(\lambda_s^{N-1})^{-\frac{3}{2}} & 0 \\ 0 & 0 & 1 \end{bmatrix} \Delta\lambda_s^N, \quad (\text{C.18})$$

also, one can write

$$\frac{\partial \psi_{NH}(I_1^N)}{\partial \mathbf{\Pi}^N} = -2C_1 \begin{bmatrix} \frac{(\lambda_s^N)^{\frac{3}{2}}}{\lambda} & 0 & 0 \\ 0 & \frac{(\lambda_s^N)^{\frac{3}{2}}}{\lambda} & 0 \\ 0 & 0 & \frac{\lambda^2}{(\lambda_s^N)^3} \end{bmatrix}. \quad (\text{C.19})$$

Therefore, the inequality up to the first order relative to $\Delta \lambda_s^N$, reads as

$$-\frac{\partial \psi_{NH}(I_1^\alpha)}{\partial \mathbf{\Pi}^N} : \Delta \mathbf{\Pi}^N \approx 2C_1 \left(\left(\frac{\lambda}{\lambda_s^N} \right)^3 - 1 \right) \frac{\Delta \lambda_s^N}{\lambda} \geq 0, \quad (\text{C.20})$$

which is clearly valid when $\lambda^{N-1} < \lambda^N < \lambda$.

C.2.3.3 Holmes-Mow

The $\Delta \mathbf{\Pi}^N$ is the same as in the Neo-Hookean case, and similarly the inequality is calculated as

$$-\frac{\partial \psi_{HM}(I_1^\alpha, I_2^\alpha, I_3^\alpha)}{\partial \mathbf{\Pi}^N} : \Delta \mathbf{\Pi}^N \approx 2\alpha_0 \exp(\mathcal{A}) \left(\alpha_1 + \alpha_2 \frac{\lambda_s^N}{\lambda} \right) \left(\left(\frac{\lambda}{\lambda_s^N} \right)^3 - 1 \right) \frac{\Delta \lambda_s^N}{\lambda} \geq 0, \quad (\text{C.21})$$

where

$$\mathcal{A} = \alpha_1(I_1^\alpha - 3) + \alpha_2(I_2^\alpha - 3). \quad (\text{C.22})$$

That also indicates since $\lambda^{N-1} < \lambda^N < \lambda$ the conditions of the second law are met for sliding.

For determining the reference configuration, if there is no sliding, the current configuration is saved for each generation ($\text{Pi_alpha}(\text{gen})=\text{lam}(i)$), and for the cases that have sliding, a function (`ReactiveSliding.m`) checks for sliding at each step, and if sliding occurs the reference configuration is calculated according to Eqs. (4.31) and (4.38). The sliding can be implemented as formative bonds with a fast kinetics rate; however, one may choose to use a ‘step’ kinetics, which assigns a value of zero to breaking generations and one to the reforming generation for speed considerations.

D.2 Calculating damage, energy, and stress

Finally, before calculating energy and stress, damage is calculated. When damage is included, similar to sliding, a function is called (`ReactiveDamage.m`) that checks for damage, which then is used to update the non-damage number-fraction array and finally stress is calculated

$$\begin{array}{l} 1 \quad w_alpha(1:\text{gen}) = (1-D(i+1))*w_alpha_nd(1:\text{gen}); \\ 2 \quad T_rb(i+1) = \mathbf{sum}(\text{psi.T}(\text{lam}(i+1)./Pi_alpha(1:\text{gen})).*w_alpha(1:\text{gen})); \end{array}$$

where, `psi.T` is a structure that passes the analytical expression for stress based on Eq. (4.21). The energy also can be deposited in a similar way if the output is requested from `ReactiveBond.m`; however, they increase the amount of calculations and generally is not recommended unless there is a need for it.

Appendix E

**FIT PARAMETER RESULTS FOR THE PLASTIC AND DAMAGE
MODELS**

Table E.1. Fit parameter results for the plastic and damage models

Bond Type	Kinetics	Intrinsic Hyperelasticity	Sliding	Damage
Plastic Model				
Formative	$[K(s^{-1}), N]_{fP}$	$[C_1(\text{MPa}), C_2]_{fP}$	-	$[k, l, r_0]_{fP}$
Mean	[0.43*, 1.44*]	[2.98, 74.34*]	N/A	[1.74*, 1.04*, 1.05]
Median	[0.32 ^a , 1.49]	[2.62 ^b , 47.47 ^c]	N/A	[1.50 ^d , 1.03, 1.04 ^e]
Q1	[0.23, 1.42]	[0.67, 41.76]	N/A	[1.34, 1.03, 1.02]
Q3	[0.55, 1.56]	[4.76, 113.87]	N/A	[1.70, 1.06, 1.06]
Sliding	-	$[C_1(MPa), C_2]_{sP}$	$[b, c, r_0]_{sP}$	-
Mean	N/A	-	[1.18*, 1.07*, 1.03]	N/A
Median	N/A	-	[1.04, 1.06, 1.03]	N/A
Q1	N/A	-	[1.00, 1.06, 1.02]	N/A
Q3	N/A	-	[1.22, 1.08, 1.03]	N/A
Damage Model				
Formative	$[K(s^{-1}), N]_{fD}$	$[C_1(\text{MPa}), C_2]_{fD}$	-	$[k, l, r_0]_{fD}$
Mean	[0.52*, 1.49*]	[2.09, 81.48]	N/A	[2.27, 1.05, 1.02]
Median	[0.34 ^a , 1.51]	[1.97 ^b , 61.53 ^c]	N/A	[2.10 ^d , 1.05, 1.03 ^e]
Q1	[0.25, 1.38]	[0.61, 50.01]	N/A	[1.26, 1.03, 1.02]
Q3	[0.67, 1.58]	[3.37, 123.12]	N/A	[2.72, 1.06, 1.03]
Permanent	-	$[C_1(MPa), C_2]_{pD}$	-	$[k, l, r_0]_{pD}$
Mean	N/A	-	N/A	[1.40*, 1.02, 1.03]
Median	N/A	-	N/A	[1.16, 1.02, 1.03]
Q1	N/A	-	N/A	[1.06, 1.02, 1.02]
Q3	N/A	-	N/A	[1.43, 1.03, 1.03]
same as fD				

* The distribution is non-normal ($p < 0.05$)

a-e The medians of the parameter distributions are different ($p < 0.05$)

Appendix F

LATERAL STRAIN OF TENDON IN RESPONSE TO OSMOTIC LOADING

In the following we are showing the raw data for the strain of all the groups 8% (control), 1%, and 15% SPEG. After exchanging the buffer solution at $t = 16$ min, the optical strain results in highly noisy readings that due to distortions because of bath solutions. In order to account for that we truncated the beginning 75 seconds of the Osmotic loading phase, and took the $t = 16$ min + 60 sec as the reference time for the osmotic loading phase.

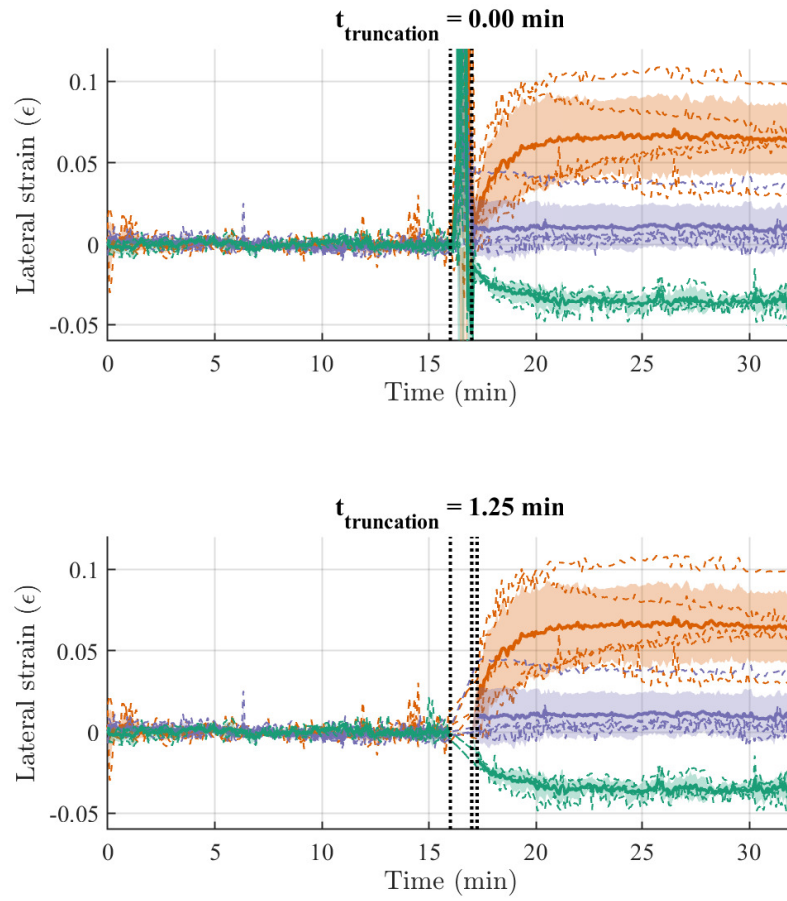


Figure F.1. Raw data for the lateral strain analysis during osmotic loading

Appendix G

NORMALIZED FLUID FLUX DURING OSMOTIC LOADING

We plotted the spatial distribution of the normalized fluid flux, where the normalization was defined as

$$\bar{f}^w = q \left(\frac{f^w}{\max f^w} \right). \quad (\text{G.1})$$

Here, f^w is the magnitude of fluid flux over the boundary of tendon and normal to surface. The parameter q indicates the direction of flow, where $q = 1$ indicates an outward flow, and $q = -1$ indicates an inward flow.

The fluid flow was not uniform along the boundary (Fig. G.1), and its maximum was along the minor axis ($\bar{f}^w = 1$ at $x = 0$), at all time steps. With progression of time, the nonuniformity increases, however, at 15 min the flow very small. This was true for both of the osmotic loading cases. Note that for osmotic loading of a circular section the flow would be uniform, and thus \bar{f}^w would always be equal to one.

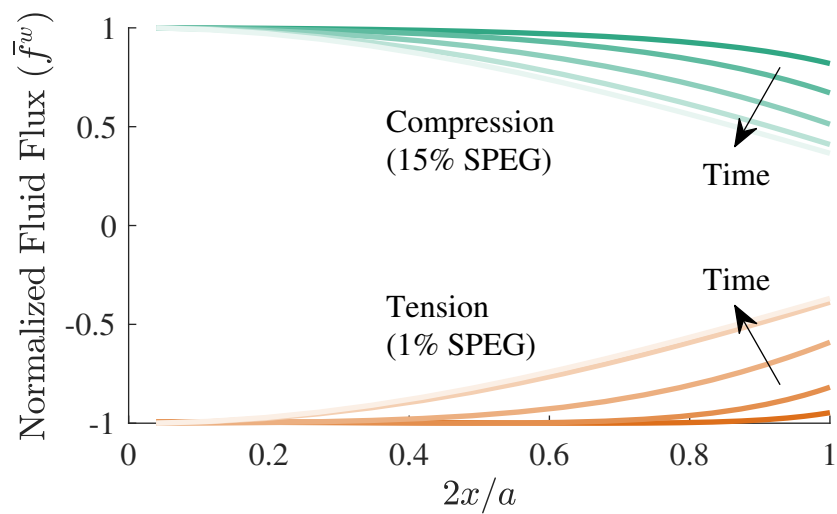


Figure G.1. The distribution of the normalized fluid flux \bar{f}^w (Eq. (G.1)) indicates that fluid flow is both spatially and temporally non-uniform. In both of the cases flow is higher along the minor axis of tendon ($x = 0$).

Appendix H

THE AUXILIARY SHEATH MESH USED FOR THE HELICAL FIBRIL'S FEM ANALYSIS

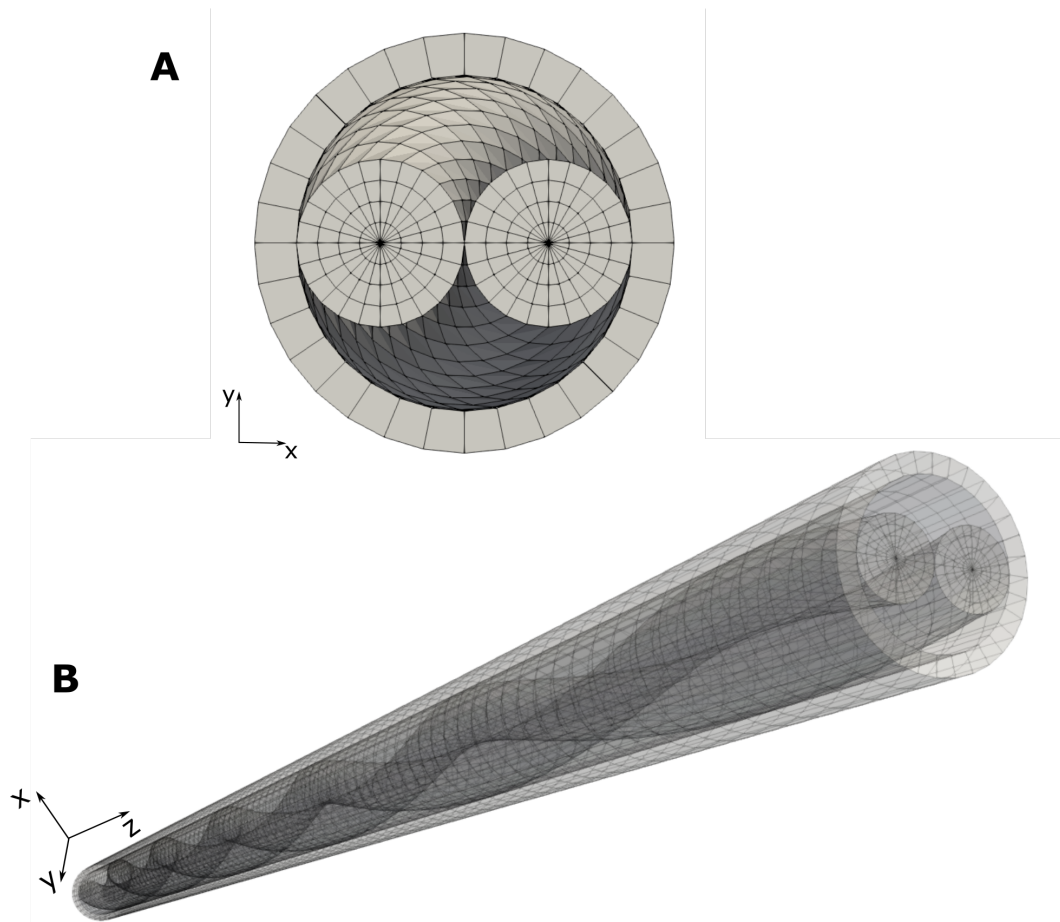


Figure H.1. The auxiliary sheath mesh used for helical fibrils FEM analysis (A) The axial view of the mesh with surrounding auxiliary sheath mesh (B) 3D view of the surrounding auxiliary sheath mesh with 25% transparency. The geometrical scale is compacted 10 times in the axial direction (z-axis) for clarity.

Appendix I

STRESS-STRAIN RESPONSE OF A SINGLE HELICAL FIBRIL

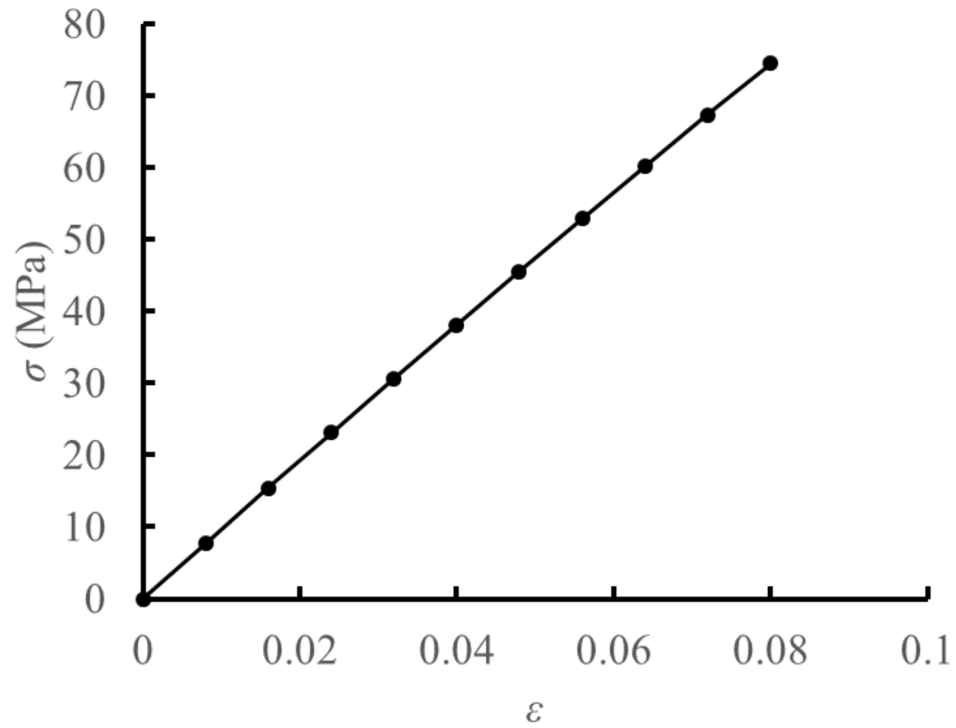


Figure I.1. Stress-strain (σ - ϵ) response of a single helical fibril with the neo-Hookean parameters of $E = 1$ GPa, $\nu = 0.2$, where the helical pitch is $\lambda = 40 \mu m$. Showing an approximately linear response with a maximum stress of ~ 74 MPa at $\epsilon = 0.08$ maximum engineering strain.

Appendix J

HISTOGRAM OF THE PERCENT TORTUOSITY OF THE FIBRILS

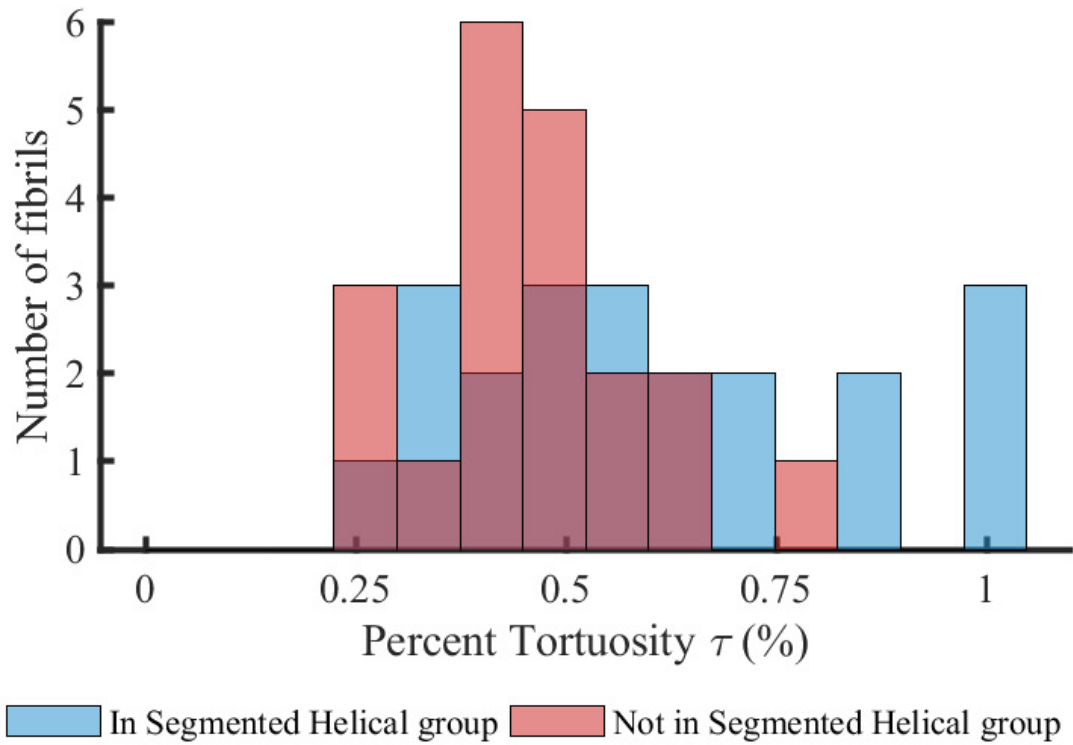


Figure J.1. Histogram of the percent tortuosity (τ) of the fibrils in segmented helical groups and the ones not in the segmented helical groups.

Appendix K

PERMISSIONS TO INCLUDE PUBLISHED MANUSCRIPTS

K.1 Permission for manuscripts of Chapters 4 and 5



Babak Naghizadehsafa <safa@udel.edu>

[time sensitive] rights and permission to include papers in my dissertation

Beth Darchi <DarchiB@asme.org>

Wed, Nov 6, 2019 at 1:48 PM

To: Babak Naghizadehsafa <safa@udel.edu>

Dear Mr. Safa,

It is our pleasure to grant you permission to use **all or any part of** the following ASME papers:

- A Reactive Inelasticity Theoretical Framework for Modeling Viscoelasticity, Plastic Deformation, and Damage in Fibrous Soft Tissue, by Babak N. Safa, Michael H. Santare, Dawn M. Elliott, J Biomech Eng. February 2019, 141(2)
- Evaluating Plastic Deformation and Damage as Potential Mechanisms for Tendon Inelasticity Using a Reactive Modeling Framework, by Babak N. Safa, Andrea H. Lee, Michael H. Santare, Dawn M. Elliott, J Biomech Eng. October 2019, 141(10)

cited in your letter for inclusion in a dissertation entitled Analysis and Modeling of Inelasticity in Tendon: Viscoelasticity, Damage, and Plastic Deformation to be published by University of Delaware.

Permission is granted for the specific use as stated herein and does not permit further use of the materials without proper authorization. Proper attribution must be made to the author(s) of the materials. **Please note:** if any or all of the figures and/or Tables are of another source, permission should be granted from that outside source or include the reference of the original source. ASME does not grant permission for outside source material that may be referenced in the ASME works.

As is customary, we request that you ensure full acknowledgment of this material, the author(s), source and ASME as original publisher. Acknowledgment must be retained on all pages where figure is printed and distributed.

Many thanks for your interest in ASME publications.

Sincerely,

[Quoted text hidden]

K.2 Permission for manuscript of Chapter 7

Licence to Publish

Notice: you are the person first named under the heading ‘Authors and Institutions’ at stage 4 of the online process to ‘Submit a Manuscript’ (referred to as “**you/your**”). we are the Royal Society, a body incorporated by royal charter, with its place of business at 6-9 Carlton House Terrace, London SW1Y 5AG (referred to as “**we/us/our**”).

You have indicated your intention to upload the article more fully detailed at stage 1 of the online submission process (the “**article**”) to be considered for publication by us. In order to publish your article we need you to grant us a licence to publish*. This licence also sets out your rights regarding use of Preprints, Accepted Author Manuscripts and the Definitive Published Version of the article (as defined below). Please read the terms of this licence carefully before uploading the article.

Ticking the box next to the question “Confirm you accept the terms and conditions of the relevant Licence to Publish.” at stage 6 of the online submission process will be taken as assurance that you have read, agree to grant and have the right to grant this licence.

Definitions

“**Preprints**” - the un-refereed version of the article;

“**Accepted Author Manuscript**” - your personal copy of the revised version of the article as accepted by us;

“**Definitive Published Version**” - the citable version of the article produced by us after peer review, copy editing and print and electronic production.

1. You grant to us for the full term of copyright in the article and any extensions thereto the exclusive right throughout the world to edit, adapt, translate, publish reproduce, distribute and display the article in printed, electronic or any other medium and format whether now known or yet to be developed; you agree to publish associated supplementary material under a [CC-BY licence*](#); and
2. You represent to us that:
 - a) the article is your original work, has not previously been published and is not currently under consideration for publication by any other entity;
 - b) in the case of a multi-authored article, you have obtained written authorisation from all the co-authors of the article (if any) to grant this licence to us on their behalf as their agent, and you will supply a copy of the same to us if we so request;
 - c) where any copyright material has been included in the article which has been sourced from third parties (e.g. illustrations, photographs, charts or maps), you have obtained all necessary written authorisations for the reproduction and distribution of these materials as

part of the article throughout the world, in all languages and in all media and formats whether now known or yet to be developed and you will supply a copy of the same to us if we so request;

d) if copyright in the article is owned by any third party, whether your employer or someone to whom you have assigned your rights, you have obtained written authorisation from such copyright owner to grant this licence to us on their behalf as their agent and will supply a copy of the same to us if we so request; and

e) the article does not contain anything which is obscene, defamatory, libellous, infringes any right of privacy or any intellectual property right (including without limitation rights in patents, copyright or trademarks) or any other rights of any person or entity, or is otherwise unlawful.

3. You assert your moral right to be identified as the Author or co-author of the article (as applicable). If your article is published, we will provide you with a PDF copy of the published article.

4. If you decide to make the Definitive Published Version of the article open access, this will be under [this licence](#).

You shall pay to us any relevant fee and we shall make the article so available from the later of the date of receipt of the relevant fee or the date of first publication of the article.

5. You retain copyright in the article. However, you authorise us to act on your behalf to defend your copyright in the article should anyone infringe it, and to retain half of any damages awarded after deducting our costs.

6. You retain the right to use the article in the following ways, provided that you acknowledge the Definitive Published Version of the article by placing the full bibliographic reference and URL of the relevant journal homepage close to the title of the article:

a) In relation to the **Preprint, Accepted Author Manuscript** and **Definitive Published Version of the article**, you are free to: make copies for your own personal use; use the article for the internal teaching purposes of your own institution or company; and make and distribute copies (including through e-mail) of the article to research colleagues, for personal use by such colleagues on a non-commercial, non-systematic basis.

b) In relation to the **Preprint** version only, you are free to post it on web sites, including electronic preprint servers.

When the **Definitive Published Version** of the article is published the Author must acknowledge it by placing the full bibliographic reference and URL of the relevant journal homepage close to the title of the article.

c) In relation to the **Accepted Author Manuscript** only, you are free to: post it on your personal or institutional web site and load it onto your institutional or subject repository once accepted for publication; use it in compilations of your work subsequent to publication of the Definitive Published Version of the article, expand the article into

book-length form, and/or otherwise re-use portions of the Accepted Author Manuscript of the article in other works. you are also free to present the article at a meeting or conference and to disseminate copies of such article to the delegates attending such meeting or conference and/or to use the Accepted Author Manuscript in a thesis or dissertation. A licence of CC-BY may be applied to the Accepted Author Manuscript, as required by some funders.

7. We are entitled to assign our rights under this licence to any third party without giving notice to you.
8. No change or modification of this licence will be valid unless confirmed in writing by us.
9. Failure or delay by us to exercise any right or remedy under this Agreement shall not be deemed to be a waiver of that right or remedy, or prevent us from exercising that or any other right or remedy on any occasion.
10. This licence is terminated in case the article is rejected for publication or the author withdraws the article for consideration for publication before publication has occurred.

US Government contracts

*For US government employees, works created within the scope of their employment are considered to be public domain (the article is not copyrightable in the US) and our publishing agreements do not require a transfer or license of rights for such works. For such works “you/your” is replaced with “United States government”

Where the author has notified us that this is the situation, the copyright line will indicate that the article constitutes a “work of the United States government” and a statement will be included in the article “US government may reproduce, without charge, all or portions of the contribution and may authorize others to do so, for official US government purposes only.”